

Small-Signal Modelling of Maximum Power Point Tracking for Photovoltaic Systems

Michael Sokolov

A Thesis submitted in fulfilment of requirements for the degree of Doctor of Philosophy and
Diploma of Imperial College London

Imperial College London
Department of Electrical and Electronic Engineering

2013

Abstract

In grid connected photovoltaic (PV) generation systems, inverters are used to convert the generated DC voltage to an AC voltage. An additional dc-dc converter is usually connected between the PV source and the inverter for Maximum Power Point Tracking (MPPT). An iterative MPPT algorithm searches for the optimum operating point of PV cells to maximise the output power under various atmospheric conditions. It is desirable to be able to represent the dynamics of the changing PV power yield within stability studies of the AC network. Unfortunately MPPT algorithms tend to be nonlinear and/or time-varying and cannot be easily combined with linear models of other system elements.

In this work a new MPPT technique is developed in order to enable linear analysis of the PV system over reasonable time scales. The new MPPT method is based on interpolation and an emulated-load control technique. Numerical analysis and simulations are employed to develop and refine the MPPT. The small-signal modelling of the MPPT technique exploits the fact that the emulated-load control technique can be linearised and that short periods of interpolation can be neglected. A small-signal PV system model for variable irradiation conditions was developed. The PV system includes a PV module, a dc-dc boost converter, the proposed controller and a variety of possible loads. The new model was verified by component-level time-domain simulations.

Because measured signals in PV systems contain noise, it is important to assess the impact of that noise on the MPPT and design an algorithm that operates effectively in presence of noise. For performance assessment of the new MPPT techniques, the efficiencies of various MPPT techniques in presence of noise were compared. This comparison showed superiority of the interpolation MPPT and led to conclusions about effective use of existing MPPT methods. The new MPPT method was also experimentally tested.

Acknowledgments

Firstly, I would like to thank to my parents Musia and Boris and other members of my family for their unlimited support throughout this work and beyond. Without them carrying out this work would be impossible.

I would like to thank to my supervisors, Prof. Tim C. Green, Dr. Paul D. Mitcheson and Prof. Doron Shmilovitz for their support, patience, inspiration and invaluable advice during this work. I have learned a lot from my supervisors and it was a great honour to be their student.

Also, I thank to members of the Control and Power research group for friendly working environment, to Jeff Bloemink for his help in the laboratory, to Nathaniel Bottrell for his advice regarding ac power systems and to Michael Merlin for his help in editing this thesis. In addition, I would like to thank to numerous friends across the campus and London for their support, help and advice.

Finally, I would like to acknowledge the financial support of this work by Alan Howard Scholarship from Energy Futures Laboratory and by Leo Baeck (London) Lodge B'nai B'rith Scholarship.

Declaration of Originality

This thesis presents results of my work. To the best of my knowledge, any previous works published by another person that were used in this thesis are appropriately referenced.

Copyright Declaration

The copyright of this thesis rests with the author and is made available under a Creative Commons Attribution Non-Commercial No Derivatives licence. Researchers are free to copy, distribute or transmit the thesis on the condition that they attribute it, that they do not use it for commercial purposes and that they do not alter, transform or build upon it. For any reuse or redistribution, researchers must make clear to others the licence terms of this work.

Contents

Abstract.....	3
Acknowledgments.....	5
Declaration of Originality	7
Copyright Declaration.....	7
List of Figures	11
List of Tables	15
List of Principle Symbols.....	16
List of Abbreviations	17
Chapter 1 Introduction.....	19
1.1 Statement of the general topic area	19
1.2 Research topics.....	20
1.2.1 Modelling of PV systems.....	20
1.2.2 Development of new MPPT algorithm	21
1.2.3 Impact of measurement noise on MPPT algorithms.....	22
Chapter 2 Literature review	23
2.1 Electrical grid analysis and distributed generation	23
2.2 Review of maximal power point tracking methods	24
2.2.1 Perturb and Observe algorithms.....	24
2.2.2 Behaviour of Perturb and Observe MPPT Algorithm.....	27
2.2.3 Incremental Conductance algorithm	27
2.2.4 dP-P&O Algorithm	28
2.2.5 Emulated Load Method.....	30
2.2.6 Other Algorithms	32
2.3 Review of small-signal modelling of PV systems	33
Chapter 3 Small-signal modelling of PV systems	35
3.1 Modelling and linearisation of the PV source	35
3.2 Derivation of a small-signal model of a PV system.....	37
3.3 Verification of the small-signal model of the PV system	39
3.4 Use of Small-signal Model for Selection of Iteration Time Step for MPPT Algorithm.....	48
3.5 Conclusions on small-signal modelling of PV systems	51
Chapter 4 Noise influence on Maximum Power Point Tracking.....	53
4.1 Introduction	53

4.2	Observation and representation of measurement noise.....	55
4.3	Simulation method	60
4.4	Results	61
4.5	Results Verification.....	65
4.6	Discussion	67
4.7	Conclusions	69
Chapter 5	Interpolation MPPT algorithm.....	71
5.1	Introduction	71
5.2	Theoretical background of polynomial interpolation.....	74
5.3	Assessment of interpolation of PV power curves	75
5.4	Interpolation of PV power curves in presence of noise	82
5.5	Algorithm development.....	85
5.6	Simulation and experimental tests.....	88
5.6.1	Simulation results.....	88
5.6.2	Experimental results.....	96
5.6.3	Simulation comparison with other algorithms according to EN 50530 standard 103	
Chapter 6	Conclusions.....	107
6.1	Concluding Remarks	107
6.2	Future work	108
Author's publications.....		111
Bibliography		113
Appendix A	Calculation of a maximum point using interpolation.....	119
Appendix B	Calculation of a maximum point in rotated axis	123
Appendix C	Simulations of interpolation error in presence of noise	127

List of Figures

Figure 1.1	Schematic diagram of an electrical network with distributed generation.	21
Figure 2.1	Flowchart of P&O algorithm with decision based on ΔV (P&O- ΔV) or on previous decision (P&O- ΔV_{ref}).	26
Figure 2.2	Flowchart of the P&O- ΔV_{ref} algorithm.	26
Figure 2.3	P&O MPPT operating point path during change in irradiation. The * represents MPP for different levels of the irradiance [34] (© 2005 IEEE).	27
Figure 2.4	Flowchart of the Incremental Conductance algorithm.	28
Figure 2.5	Flowchart of the dP-P&O algorithm.	29
Figure 2.6	PV panel characteristics and the linear approximation of MPP loci [41] (© 2008 IEEE).	30
Figure 2.7	Emulated load based MPPT control scheme.	31
Figure 2.8	PV panel characteristics and the linear approximation of MPP loci at different temperatures: solid line – at 50°C, dashed line – at 25°C.	32
Figure 2.9	Schematic diagram of the boost dc–dc converter [49] (© 2007 IEEE).	33
Figure 2.10	PV characteristic and its linear small-signal representation.	34
Figure 3.1	Model of the PV generator.	35
Figure 3.2	Small-signal model of PV generator.	36
Figure 3.3	The modelled PV system.	37
Figure 3.4	The controller of the PV system.	39
Figure 3.5	Simulink simulation of the PV system.	40
Figure 3.6	Simulation results for constant output current i_o : top to bottom: v_{in} , v_o , i_L , d , e_f . (a) state-space model (b) time domain simulation.	43
Figure 3.7	Simulation results for constant output voltage v_o : top to bottom: v_{in} , i_L , d , e_f , i_o . (a) state-space model (b) time domain simulation.	45
Figure 3.8	Simulation results for resistive load v_o : top to bottom: v_{in} , v_o , i_L , d , e_f . (a) state-space model. (b) time domain simulation.	47
Figure 3.9	System response to a step of 0.5 V in v_{ref} . (a) Time-domain Simulink simulation, top to bottom: PV array voltage v_{pv} , output voltage v_o , inductor current i_L , average inductor current $\langle i_L \rangle$, duty cycle d , filtered error e_f . (b) small-signal model, top to	

bottom: PV array voltage v_{pv} , output voltage v_o , inductor current i_L , duty cycle d , filtered error e_f	49
Figure 3.10 Response of the system to a step in v_{ref} that occurs before output voltage v_o reaches steady state.	50
Figure 4.1 Schematic of dc-dc converter used for observation of measurement noise.	56
Figure 4.2 Current measurement circuit.	56
Figure 4.3 Experimentally measured PV voltage and current shapes.	57
Figure 4.4 Histograms of experimentally measured PV voltage and current and calculated power.....	58
Figure 4.5 Histograms of simulated realistic PV voltage and current and calculated power.	59
Figure 4.6 Histograms of simulated Gaussian PV voltage and current and calculated power.	59
Figure 4.7 Flowchart of simulation procedure. (V and I are observations without noise. V_n , and I_n are observations with noise.)	60
Figure 4.8 Efficiency of the algorithms with various step-sizes at different irradiation levels.	63
Figure 4.9 PV Voltage using as a result of operation of P&O- ΔV_{ref} algorithm (realistic noise) at irradiation of 1 Sun.....	64
Figure 4.10 Convergence process of P&O- ΔV_{ref} algorithm with step size 0.1 V at irradiation of 1 Sun.	65
Figure 4.11 Experimental results of P&O- ΔV algorithm operation with step-size of 0.05 V.	66
Figure 4.12 Experimental results of P&O- ΔV_{ref} algorithm operation with step-size of 0.05 V.	67
Figure 5.1 PV characteristic sampled at three points, calculated parabola and maximum points.....	72
Figure 5.2 The function $(x-x_0)(x-x_1)(x-x_2)$, $x_1=0$	75
Figure 5.3 Power – voltage characteristic of PV panel and its third derivative.....	76
Figure 5.4 Power – V_{ref} characteristic of PV panel and its third derivative at irradiation of 1 Sun.	77
Figure 5.5 Power – voltage characteristic of PV panel and its third derivative at irradiation of 1 Sun in axis system rotated by 3°	78

Figure 5.6 Simulation results of maximum calculation at different sampling points. Top to bottom: power loss, error of maximal power estimation, error of maximum location.80

Figure 5.7 Different positions of the sampling points.80

Figure 5.8 Simulation results of mean power loss in maximum calculation in V-P plane at different sampling points in presence of noise. Distance between sampling points, top to bottom: 0.7 V, 1 V, 1.5 V.83

Figure 5.9 Simulation results of mean power loss in maximum calculation in V_{ref} -P plane at different sampling points in presence of noise. Distance between sampling points, top to bottom: 0.7 V, 1 V, 1.5 V, 2 V.84

Figure 5.10 Flowchart of the interpolation MPPT algorithm.87

Figure 5.11 Steady state operation at the irradiation of 1 Sun. (a) Interpolation algorithm. (b) P&O- ΔV_{ref} algorithm.89

Figure 5.12 Steady-state operation at the irradiation of 0.3 Sun. (a) Interpolation algorithm. (b) P&O- ΔV_{ref} algorithm.90

Figure 5.13 Operation during irradiation increase from 0.3 Sun to 1 Sun. (a) Interpolation algorithm. (b) P&O- ΔV_{ref} algorithm.92

Figure 5.14 Operation during irradiation decrease from 1 Sun to 0.3 Sun. (a) Interpolation algorithm. (b) P&O- ΔV_{ref} algorithm.93

Figure 5.15 Operation during irradiation increase from 0.1 Sun to 0.5 Sun. (a) Interpolation algorithm. (b) P&O- ΔV_{ref} algorithm.94

Figure 5.16 Operation during irradiation decrease from 0.5 Sun to 0.1 Sun. (a) Interpolation algorithm. (b) P&O- ΔV_{ref} algorithm.95

Figure 5.17 Characteristic of the PV emulator at short circuit current $I_{sc}=3.5$ A (x: 2V/div, y: 0.5A/div).96

Figure 5.18 P&O- ΔV_{ref} algorithm at steady irradiation.97

Figure 5.19 Interpolation algorithm at steady irradiation.98

Figure 5.20 P&O- ΔV_{ref} algorithm at changing irradiation.99

Figure 5.21 Interpolation algorithm at changing irradiation (version with measurement at constant long time intervals).100

Figure 5.22 Interpolation algorithm at changing irradiation (version with measurement after change in irradiation is detected).101

Figure 5.23	Characteristic of the PV emulator.	102
Figure 5.24	Convergence process of the interpolation algorithm.	102
Figure 5.25	Convergence process of the P&O- ΔV_{ref} algorithm.	103
Figure 5.26	Irradiation profile for dynamic efficiency tests according to EN 50530 standard.	104
Figure A.1	Schematic illustration of the sampled points and parabola that intersects them.	119
Figure B.1	Sampled points on rotated axis.	123
Figure C.1	Simulation results of power loss in maximum calculation in V-P plane at different sampling points in presence of noise. Distance between sampling points 0.7 V.	128
Figure C.2	Simulation results of power loss in maximum calculation in V-P plane at different sampling points in presence of noise. Distance between sampling points 1 V...129	129
Figure C.3	Simulation results of power loss in maximum calculation in V-P plane at different sampling points in presence of noise. Distance between sampling points 1.5 V.	130
Figure C.4	Simulation results of power loss in maximum calculation in V_{ref} -P plane at different sampling points in presence of noise. Distance between sampling points 0.7 V.	131
Figure C.5	Simulation results of power loss in maximum calculation in V_{ref} -P plane at different sampling points in presence of noise. Distance between sampling points 1 V.	132
Figure C.6	Simulation results of power loss in maximum calculation in V_{ref} -P plane at different sampling points in presence of noise. Distance between sampling points 1.5 V.	133
Figure C.7	Simulation results of power loss in maximum calculation in V_{ref} -P plane at different sampling points in presence of noise. Distance between sampling points 2 V.	134

List of Tables

Table 4.1 Algorithms power losses [%] at 1 Sun, $P_{MPP} = 60.47$ W, $V_{MPP} = 17.01$ V.....	62
Table 4.2 Algorithms power losses [%] at 0.5 Sun, $P_{MPP} = 29.76$ W, $V_{MPP} = 16.74$ V.....	62
Table 4.3 Algorithms power losses [%] at 0.5 Sun, $P_{MPP} = 5.46$ W, $V_{MPP} = 15.41$ V.....	62
Table 5.1 Static MPPT efficiency	104
Table 5.2 Dynamic MPPT efficiency	105
Table 5.3 MPPT efficiency according to EN 50530 standard.	105

List of Principle Symbols

I_{pv} –	current of PV array
V_{pv} –	voltage of PV array
P_{pv} –	power of PV array
ΔT –	time interval between iterations of MPPT algorithms
V_{ref} –	reference voltage of dc-dc converter controller
ΔV_{ref} –	incremental value of MPPT algorithms
r –	gain of current amplifier in emulated load controller
i_{sat} –	diode saturation current
v_t –	thermal voltage
v_{MPP} –	voltage of a PV panel (or cell) at the MPP
P_{MPP} –	power of a PV panel (or cell) at the MPP
V_{refMPP} –	value of V_{ref} that achieves operation at the MPP
$V_{ref_est_MPP}$ –	estimate of the value of V_{ref} that provides operation at the MPP
$P_{op_est_MPP}$ –	power obtained when the PV panel operates at the estimated MPP (i.e., P when $V_{ref} = V_{ref_est_MPP}$)
$V_{op_est_MPP}$ –	voltage of a PV panel when the panel operates at estimated MPP
P_{est_MPP} –	estimate of power of a PV panel (or cell) at the MPP
d –	duty cycle of a PWM signal
e –	error signal of linear controller
\hat{x} –	small-signal value
X –	large-signal value
ω –	angular frequency
η –	efficiency

List of Abbreviations

AC	Alternating Current
ADC	Analogue to Digital Converter
CEC	California Energy Commission
DC	Direct Current
EU	European Union
Inc	Incremental Conductance
MPP	Maximum Power Point
MPPT	Maximum Power Point Tracking
P&O	Perturb and Observe
PV	Photovoltaic
PWM	Pulse-width modulation

Chapter 1

Introduction

1.1 Statement of the general topic area

Solar energy is one of the main available sources of non-polluting energy and photovoltaic (PV) arrays are commonly used to convert the energy from the solar irradiation to electrical energy directly. The major limit for wide usage of this energy source is the high cost of production of PV cells [1].

Recently, the use of renewable energy, particularly solar energy, has been rising [2]. Photovoltaic (PV) technology has been taken up where grid supplies are difficult to obtain or where subsidies exist to defray the initial purchase cost. Clearly, the technology still has some cost barriers to widespread use and so anything that can be done to ease the integration costs is helpful to promoting this form of renewable energy. A key advantage of PV is that the energy production is correlated to peak demand in office buildings and to air-conditioning use [3]. Also, the integration of PV into architectural building panels suits office building use [4]. In London, for instance, load growth beyond substation capacity now restricts building refurbishment and using on-site renewable generation to reduce peaks in demand is economically attractive because it avoids network reinforcement [5]. Small amounts of PV generated power injected into a distribution network can be handled as disturbance or as negative load [6], but when the PV sources contribute a significant fraction of the total power production, the network will be influenced by the characteristics of many small and independently controlled units. The increase of use of renewable energy sources and distributed power generation raises concerns about the stability of the electrical network and

the power quality [7]. Some European countries already take steps to limit renewable energy micro-generation due to the potential risk of grid instability [8].

1.2 Research topics

The aim for this work is to improve the efficiency and ease of integration of PV power generation systems by addressing questions in three areas described in the following sections.

1.2.1 Modelling of PV systems

Since grid stability is a great concern when more renewable power sources needed to be added to a network, it is important to develop system models that combine the new power sources and the existing network infrastructure that facilitate stability analysis. Commonly, such analysis is done using linear or linearised state-space models of the system. Grid stability analysis is discussed in [9] and although work on micro-grid stability analysis exists [10],[11], to date these models do not include a sufficiently detailed representation of PV systems. A PV system typically consists of dc-dc and dc-ac switched-mode mode power converters, linear controllers and an overall MPPT algorithm. Modelling of switched-mode mode power converters and linear controllers is well established. The MPPT, however, has the nature of a search algorithm rather than a control system and does not fit into existing linearised modelling methods and stability analysis. This work aims to develop a model of a PV system with MPPT algorithm that can be included in a wider system model. It is expected that this will require creation of a new MPPT algorithm that is amenable to linearisation.

Recently, work on analysis of a micro-grid with multiple power sources and loads have been conducted [10],[11]. A schematic diagram of electrical network with distributed generation is shown in Figure 1.1, where the system analysed in [10] is shown in the central part of this figure. In this previous work a constant DC voltage at the DC inputs to the inverters was assumed. A further simplification was that only simple load such as resistors

and uncontrolled rectifiers were analysed. In order to conduct a more realistic analysis of an electrical grid with distributed generation, more detailed representations of renewable energy sources and of complex loads are needed. Modelling of a controlled (or active) load, which is shown in the right part of Figure 1.1, is currently being conducted by another PhD student, Nathaniel Bottrell. This work aims to create a suitable model of the PV generation system shown in the left part of Figure 1.1 in order to incorporate it with models of other parts of the electrical network. The PV generation system consists of a PV module and a dc-dc converter which is connected to the inverter and controlled by a Maximum Power Point Tracking (MPPT) controller.

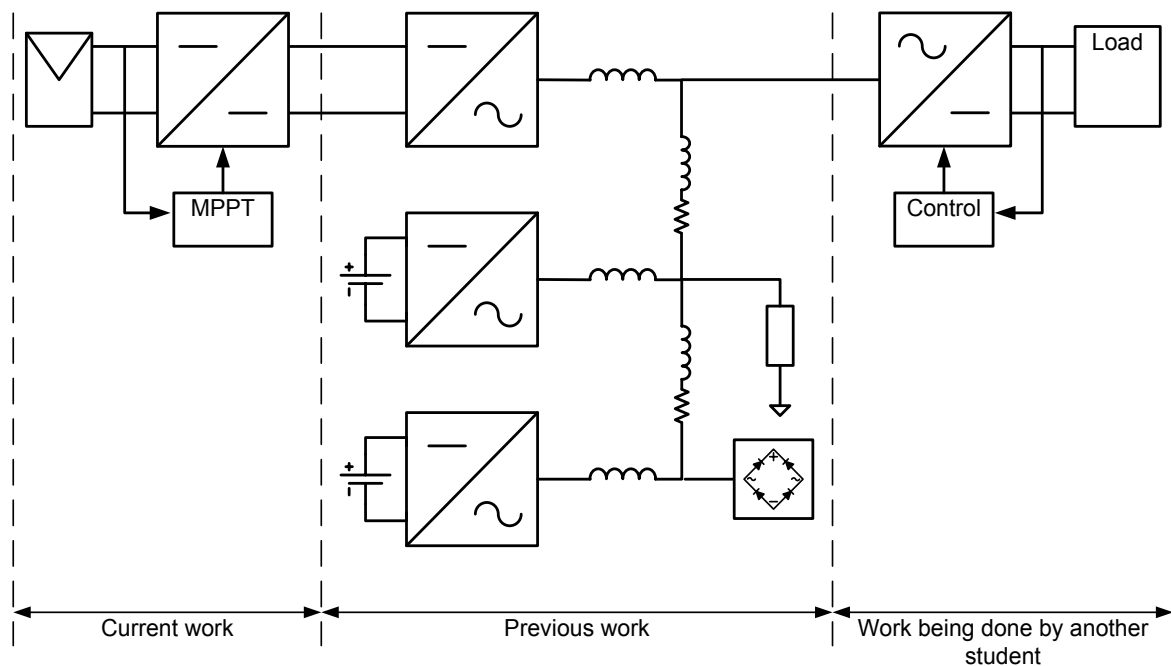


Figure 1.1 Schematic diagram of an electrical network with distributed generation.

1.2.2 Development of new MPPT algorithm

Efficiency of a PV system is a very important factor in the cost-benefit analysis of a proposed system. The efficiency of the PV system is composed of a product of efficiencies of the subsystems, namely, the efficiency of the solar cells, the efficiency of the power converters and effectiveness of MPPT operation. The MPPT algorithm is responsible for

maximum utilization of the generation potential of PV cells under various environmental conditions. Ensuring fast and accurate attainment of the maximum power point (MPP) of a PV panel is recognized as being important in making effective use of the relatively expensive panel materials [12]. The nonlinear voltage-current characteristic and its dependence on both irradiation and temperature requires a real-time search for the MPP based on feedback of operating conditions [13]. Improving MPPT performance and reliability is important and has received much attention in the literature [14],[15] because it has the same effect on the system in increasing the output power as improving the efficiency of the PV cells themselves. Many different MPPT algorithms have been proposed and discussed in the literature [14]-[24]. Many of these methods perform with very high efficiency. Even so, achieving excellent MPPT performance for certain conditions such as changing irradiation and partial shading is still challenging. The algorithm being developed in this work aims to match or exceed the performance of existing commonly used methods.

1.2.3 Impact of measurement noise on MPPT algorithms

The voltage and current of a PV panel need to be measured for MPPT operation. As in other physical systems, measurements on PV panels contain measurement noise. Usually the noise is small in comparison to the signal. However, it is important to note that in MPPT, differences are calculated between two (or more) measurements that are normally close to each other and these differences, which are particularly susceptible to measurement noise, are used for decisions on changes to the PV operating point. Thus it is important to analyse the impact of measurement noise on both the efficiency and the dynamics of MPPT algorithms. In this work, performance of several commonly used MPPT methods will be analysed and compared. Any newly developed MPPT method will be included in this comparison.

Chapter 2

Literature review

2.1 Electrical grid analysis and distributed generation

Power grid stability is widely discussed in “Power System Stability and Control” by Prabha Kundur [9]. According to this book, the stability problem can be divided to several categories. The type of stability is classified by the physical parameter being analysed (e.g. voltage or angle), the extent of the disturbance (small-signal stability or transient stability) and the time duration of the analysed phenomena. The small-signal stability is analysed using a state-space representation of the linearised system in which the time varying ac signals are represented using the d-q transform [9]. Kundur [9] concentrates on a traditional large electrical network in which the power is generated by synchronous machines. Small-signal modelling of a micro-grid, in which all of the sources were inverters, was presented in [11]. This model assumed that there was a constant DC link voltage and therefore no dynamics in the DC link voltage caused by the source of DC power. In the work to be described here, the focus is on providing models of PV power sources to include in such small-signal stability analysis of electrical systems.

A model for stability analysis of a PV generator with the P&O MPPT algorithm was developed in [17], but this model is nonlinear so it cannot be represented using state-space equations. In [25] a small-signal modelling of a renewable-energy-based distribution system is presented, but there was an assumption of constant generated power. In [26],[27], the MPPT algorithm was kept as a nonlinear block combined with linear models of other components. In [28], the MPPT algorithm was represented as a linear block using an unrealistic assumption that the MPP is known and a simple linear controller was used to

reach the MPP. Only recently a linearised model of an analogue implementation of the Incremental Conductance (Inc) MPPT algorithm has been developed [29]. Analogue implementation of the Inc algorithm is not commonly used, however. The work reported in [29] does not include any experimental verification, and their simulation does not take measurement noise into account or compare the MPPT efficiency with other algorithms.

2.2 Review of maximal power point tracking methods

Many MPPT control methods have been developed. The simplest method is to set the PV cell voltage to a constant voltage as an approximation of the MPP location since the MPP voltage varies across a relatively narrow range [16]. This method is not very accurate and is suitable only for small systems where minimising the “balance of system” costs (i.e. the costs beyond the basic PV panel) is the dominant concern. A better approximation can be achieved by setting the PV cell voltage to a proportion of its open circuit voltage [30]. In similar way, the PV cell current can be set as a proportion of the short circuit current [30]. The periodical measurement of the open circuit voltage or short circuit current requires additional hardware. Also, the time periods between the measurements are usually long, since frequent sampling will lead to significant loss of output power (i.e. lower efficiency) and long sampling intervals lead to poor tracking performance. Even though these two open-loop methods are more accurate than the constant voltage method, they are still based on a rough approximation of the MPP.

2.2.1 Perturb and Observe algorithms

A very popular MPPT method is called Perturb and Observe (P&O) [14],[31]-[33] and many modifications to it have been developed. In this method, a microcontroller measures the PV cell voltage and current then calculates the power by multiplying them. The result is compared to a previous measurement and the operating point is moved in the direction that is

expected to increase power. The voltage and current are then measured again and a further adjustment made. After several perturb and observe operations, the operation point will be close to the MPP but subject to small perturbation around it. This method is accurate but relatively slow as tracking is performed step-by-step, each step requires waiting until the PV voltage and current are stable and steps need to be small to ensure the perturbations around the MPP are small [34]. The P&O algorithm has two parameters that need to be adjusted for correct operation: the step size and the time between algorithm iterations. There is a trade-off in choosing the step size as large step size allows fast tracking, but small step size is needed for better accuracy [34]. The time intervals between algorithm iterations should be short to allow faster tracking, but they must be longer than the settling time of the PV current and voltage for reliable signal measurement and filtering. Fast tracking is especially important when irradiation is changing quickly during cloudy weather or in solar powered vehicles. Since the P&O algorithm has been developed for steady-state operation it may work incorrectly during changing irradiation [35].

In this work, two versions of this algorithm are discussed, both are shown in Figure 2.1. In one version, the check of the previous step is based on the measured voltage of the PV panel $\Delta V = V - V(\text{prev})$. This variant was used in [16]-[18] and a noise model for this variant was developed in [36]. The other version uses information about the previous choice of reference voltage rather than the measured voltage, $\Delta V = V_{ref} - V_{ref}(\text{prev})$. This version was used in [19]-[21] and a model for this algorithm based on Markov chain was developed in [37]. These two P&O algorithm options will be referred as P&O- ΔV and P&O- ΔV_{ref} respectively. When it is assumed that no measurement noise is present, both algorithms have the same behaviour and will be referred as P&O. The flowchart of an alternative implementation of the P&O- ΔV_{ref} algorithm is shown in Figure 2.2 [38].

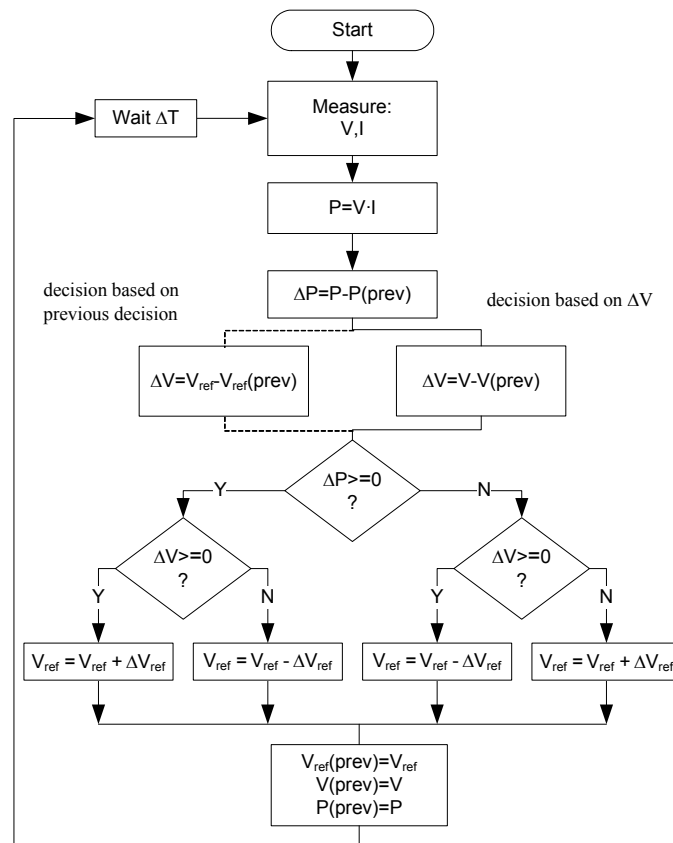


Figure 2.1 Flowchart of P&O algorithm with decision based on ΔV (P&O- ΔV) or on previous decision (P&O- ΔV_{ref}).

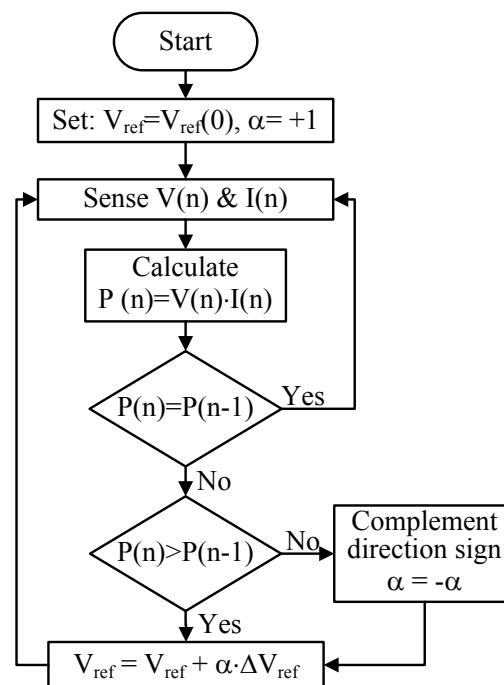


Figure 2.2 Flowchart of the P&O- ΔV_{ref} algorithm.

2.2.2 Behaviour of Perturb and Observe MPPT Algorithm

The Perturb and Observe method has good accuracy under steady state operation, but it is less accurate and relatively slow during the reaction to changing irradiation conditions. As described in [35], the P&O algorithm can cause the operating voltage to oscillate during changing irradiation. This process is clearly shown in Figure 2.3 from [34], where the MPP tracking process during the increase in irradiation from 0.2 Sun to 0.8 Sun is shown (where 1 Sun is taken to be a solar irradiance of $1,000 \text{ W/m}^2$). This oscillation of the operating voltage prevents the maximum power point being found during continuously increasing and decreasing irradiation.

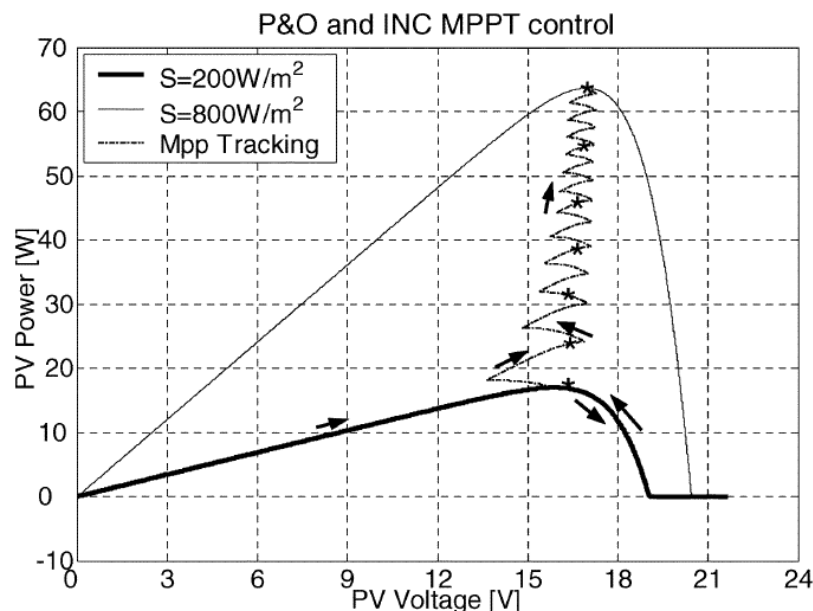


Figure 2.3 P&O MPPT operating point path during change in irradiation. The * represents MPP for different levels of the irradiance [34] (© 2005 IEEE).

2.2.3 Incremental Conductance algorithm

The Incremental Conductance (Inc) algorithm [39] was originally developed to improve the performance of the P&O algorithm and even though the improvements are limited [40], it is one of the most widely used MPPT algorithm variants. It similar to the Perturb and Observe method in its operation, but instead of calculating the PV cell power, it is based on a

mathematical development of $dP/dV|_{MPP}=0$ expressed in terms of voltage and current. The flowchart of the Inc algorithm is shown in Figure 2.4. The Inc method requires more calculations to be performed by the microprocessor than the Perturb and Observe method. It is unclear whether Inc can achieve better efficiency than P&O [34].

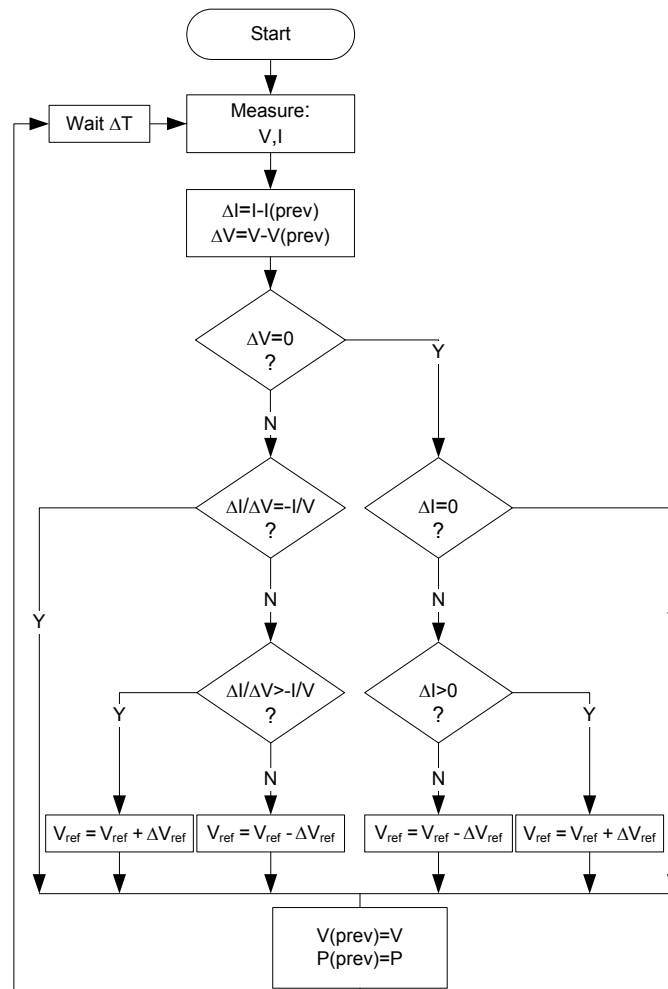


Figure 2.4 Flowchart of the Incremental Conductance algorithm.

2.2.4 dP-P&O Algorithm

The P&O algorithm may operate incorrectly during changing irradiation conditions [35] (because the algorithm cannot distinguish whether the measured change in power is caused by the algorithm's perturbation or by a change in irradiation). The dP-P&O algorithm [24] was developed to overcome this deficiency. It is known as being very

effective for changing irradiation conditions. The flowchart of dP-P&O algorithm is shown in Figure 2.5. This algorithm is based on two sets of power change measurements: with and without perturbing the V_{ref} . The difference between the two values is used to decide the next step in similar manner to the P&O algorithm.

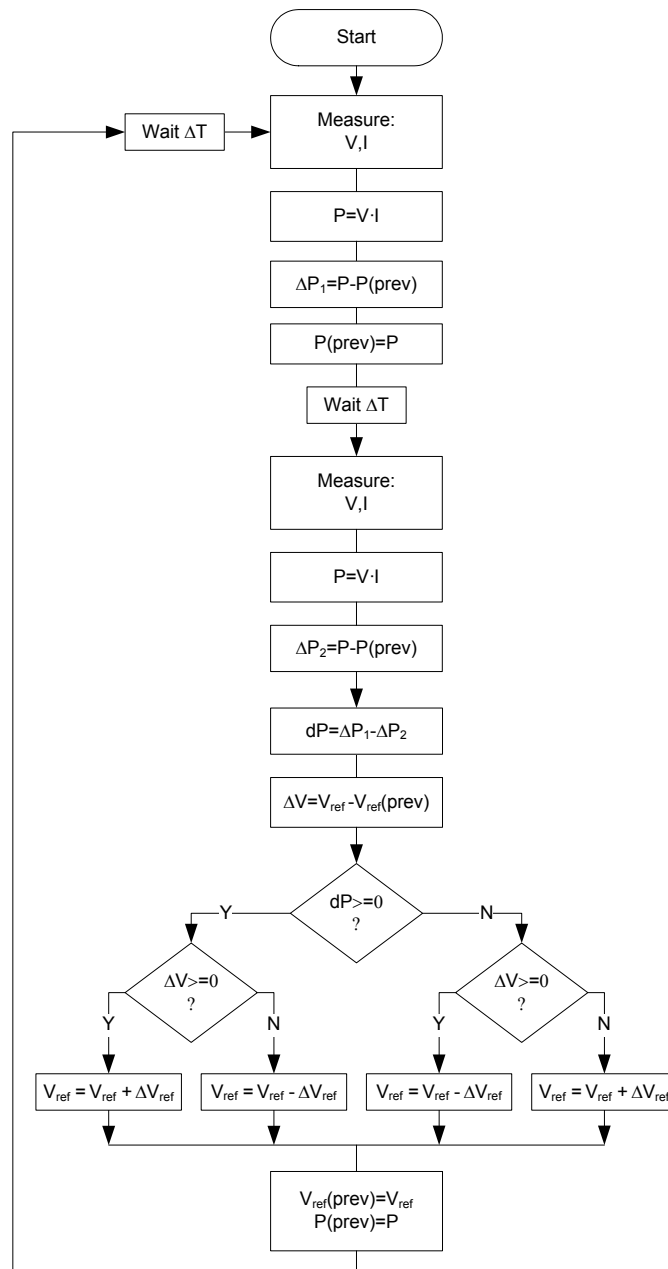


Figure 2.5 Flowchart of the dP-P&O algorithm.

2.2.5 Emulated Load Method

The emulated load method is based on the linear approximation of the loci of maximum power points in the voltage-current plane [41]. This approximation is shown in Figure 2.6 and described by equation (2.1), where r and V_{ref} are fixed and adjustable parameters respectively. The analytically derived function (neglecting the photovoltaic source's series and parallel resistances) of MPP loci is available from [42] and described by equation (2.2), where i_{sat} is the saturation current of the internal PV source's diode and v_t is the thermal voltage.

$$v_{pv} - i_{pv}r - v_{ref} = 0 \quad (2.1)$$

$$i_{MPP}(v_{MPP}) = i_{sat} \frac{v_{MPP}}{v_t} e^{\frac{v_{MPP}}{v_t}} \quad (2.2)$$

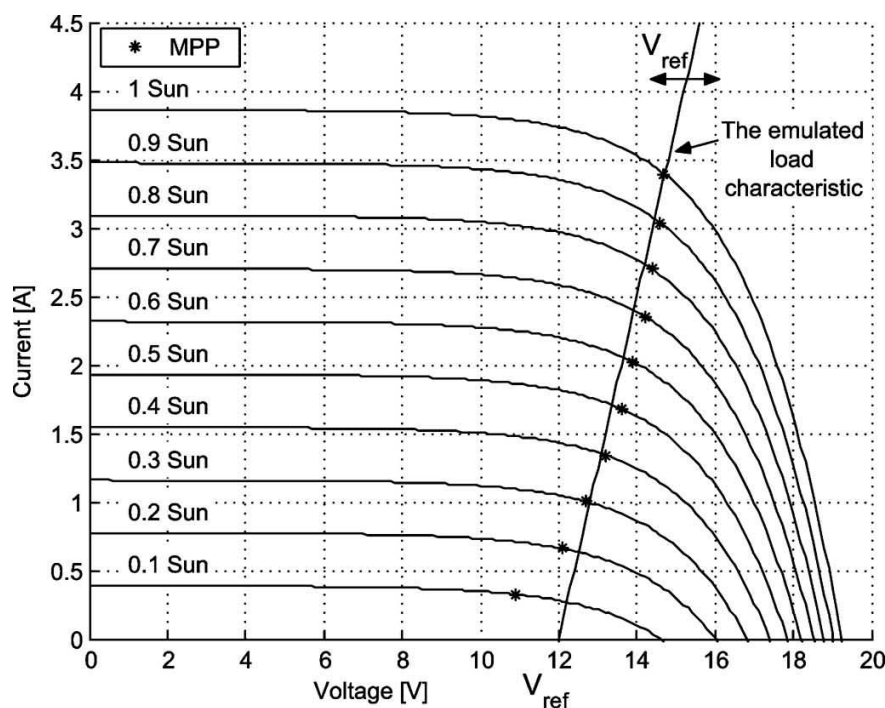


Figure 2.6 PV panel characteristics and the linear approximation of MPP loci [41] (© 2008 IEEE).

Operation along this linear approximation of maximum power points loci is achieved by the control scheme shown in Figure 2.7, which is designed to implement equation (2.1). The adjustment of v_{ref} is performed by the P&O algorithm.

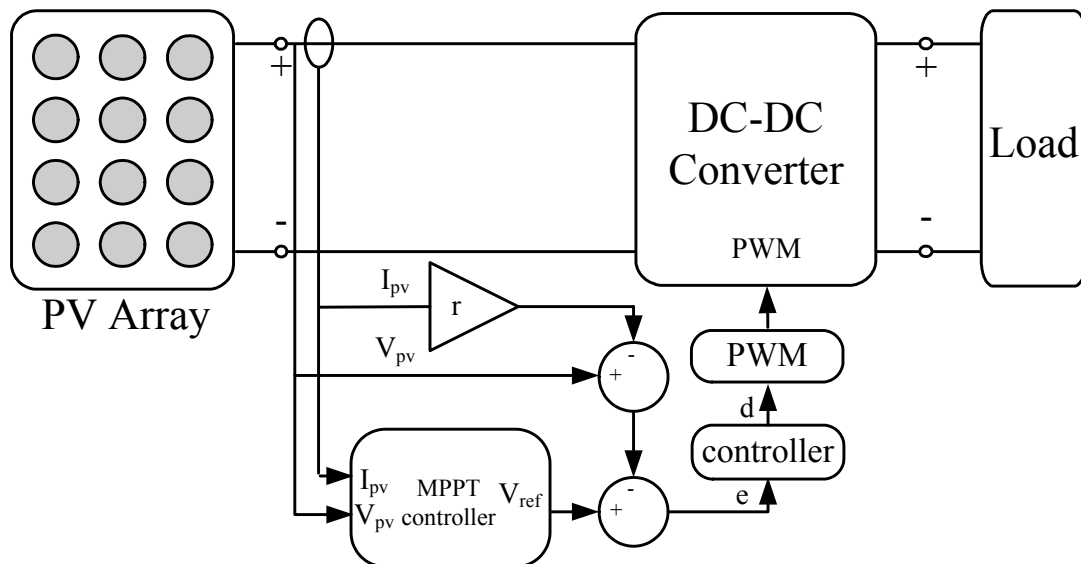


Figure 2.7 Emulated load based MPPT control scheme.

Since the operation along the emulated load characteristic is achieved by a linear controller it is possible to derive an analytical model of such a system assuming V_{ref} is constant. However, fixed V_{ref} provides only an approximation for the MPP loci at a limited range of irradiation levels and at a constant temperature. The reference voltage V_{ref} needs to be changed to account for the dependence of I-V PV characteristics on panel temperature. Figure 2.8 shows the characteristics of a PV panel and the emulated load at different temperatures. An MPPT algorithm such as P&O can be added to adjust V_{ref} [41], but this re-introduces the problem of linearisation of the algorithm.

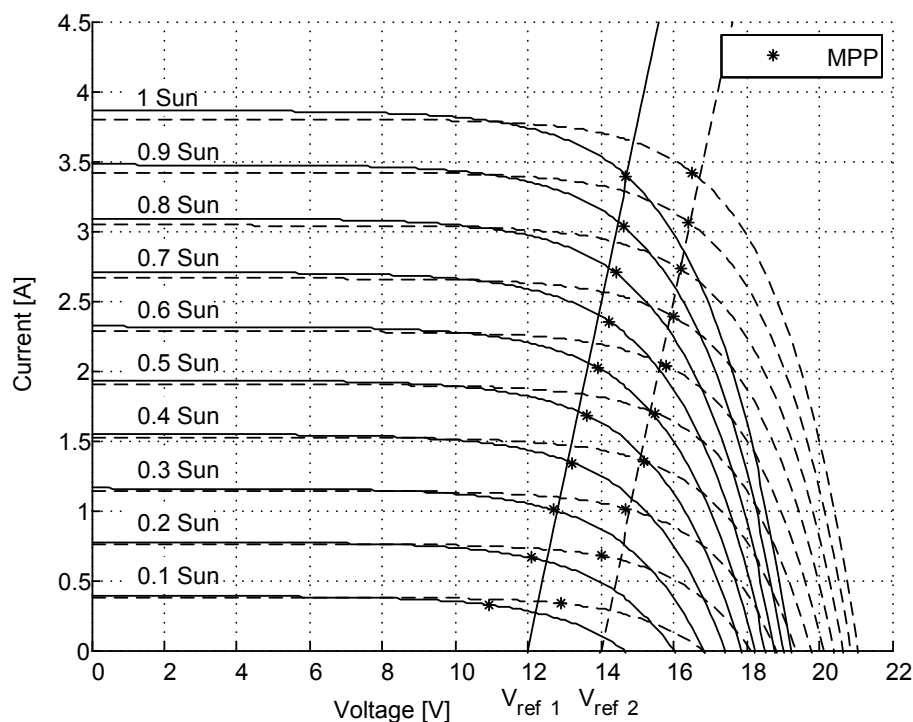


Figure 2.8 PV panel characteristics and the linear approximation of MPP loci at different temperatures: solid line – at 50°C, dashed line – at 25°C.

2.2.6 Other Algorithms

Many other methods have been developed to improve different aspects of Maximal Power Point Tracking [14]. Some of them aim to be simpler and require less hardware, others aim to achieve fast and accurate response. Variable step-size P&O algorithms, such as [43], were developed in order to overcome the trade-off in choosing the step size of the P&O algorithm. Variable step-size algorithms can track changes in irradiation faster but are more complex, have more parameters that need to be adjusted and still can suffer from problems of the P&O algorithm that were discussed in section 2.2.2. Fuzzy logic based algorithms such as [44] can achieve good system performance but like variable-step algorithms they are more complex and more difficult to calibrate. Artificial neural networks based algorithms, such as [45], also can perform well but are complex and require period of training before effective operation. When PV array is partially shaded its P-V characteristic may have multiple local MPPs. Conventional MPPT algorithms search only for a local MPP. There are MPPT

algorithms that search for global MPP in partial shading conditions [46]-[48]. Those algorithms perform wider sweep of the P-V characteristic which is time consuming.

2.3 Review of small-signal modelling of PV systems

An example of small-signal modelling for a boost converter connected to a PV source is shown in [49], where a state-space model is derived for the system depicted in Figure 2.9. The linearisation technique is based on averaging the switching operation and neglecting the high frequency PWM switching and nonlinear terms in the circuit equations [50]. In [49], a constant output voltage across C_2 was assumed, but this is not realistic if an inverter is connected to the output. Also, the irradiance is assumed to be constant. Hence the model presented in [49] needs to be augmented.

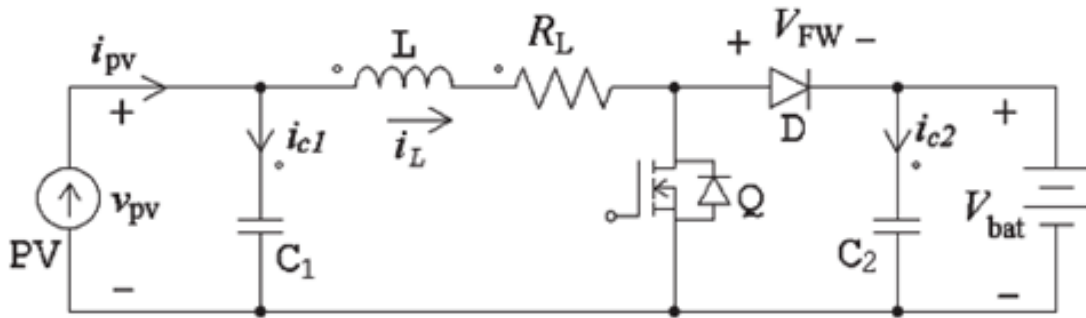


Figure 2.9 Schematic diagram of the boost dc–dc converter [49] (© 2007 IEEE).

The state-space model of the linearised system is:

$$\frac{d}{dt} \begin{bmatrix} \hat{i}_L \\ \hat{v}_{PV} \end{bmatrix} = \begin{bmatrix} -\frac{R_L}{L} & \frac{1}{L} \\ -\frac{1}{C_1} & \frac{1}{r_{PV}C_1} \end{bmatrix} \begin{bmatrix} \hat{i}_L \\ \hat{v}_{PV} \end{bmatrix} + \begin{bmatrix} \frac{V_{bat}+V_{FW}}{L} \\ 0 \end{bmatrix} \hat{d} \quad (2.3)$$

$$\hat{v}_{PV} = [0 \quad 1] \begin{bmatrix} \hat{i}_L \\ \hat{v}_{PV} \end{bmatrix}$$

Where r_{pv} is PV source's dynamic resistance: $r_{PV} = -R_S - \frac{v_t}{i_{sat}} e^{-\frac{v_{PV}+i_{PV}R_S}{v_t}}$ (2.4)

While i_{sat} is the saturation current of the internal PV source's diode, v_t is the thermal voltage and R_S is the internal series resistance of the PV model.

Then, the transfer function of this system is:

$$G(s) = \frac{\hat{v}_{PV}(s)}{\hat{d}(s)} = \frac{K}{\frac{s^2}{\omega_n^2} + \frac{2\xi_n s}{\omega_n} + 1} \quad (2.5)$$

In this transfer function, the duty cycle d is the input and the PV generator voltage v_{pv} is the output. The parameters in this transfer function are:

$$K = -(V_{bat} + V_{FW}) \frac{r_{PV}}{r_{PV} - R_L} \quad (2.6)$$

$$\omega_n = \sqrt{\frac{1}{LC_1} \left(1 - \frac{R_L}{r_{PV}}\right)} \quad (2.7)$$

$$\xi_n = \left(\frac{R_L}{L} - \frac{1}{r_{PV}C_1}\right) \frac{1}{2\omega_n} \quad (2.8)$$

It should be noted that r_{pv} has a negative value as can be seen from the $i - v$ characteristics illustrated in Figure 2.10.

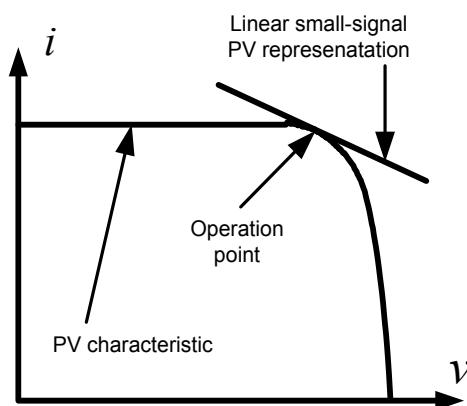


Figure 2.10 PV characteristic and its linear small-signal representation.

This model was created to provide transfer function for regulation of the PV voltage and does not attempt to include MPPT algorithm as part of the model.

Chapter 3

Small-signal modelling of PV systems

3.1 Modelling and linearisation of the PV source

In order to incorporate irradiation as an input to the small-signal model, a detailed representation of the PV module is required. A model of a PV module [34] is shown in Figure 3.1. All components of this model except the diode D_j are linear, so only D_j needs to be linearised. The linearised diode is a slope resistance for a particular operating point and can be combined with R_{sh} to form a single element that will be called r_{pvd} .

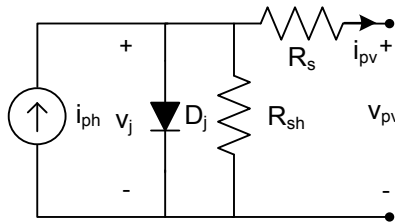


Figure 3.1 Model of the PV generator.

The current of the PV source can be described by a non-explicit function:

$$i_{PV} = i_{ph} - f(v_j) = i_{ph} - f(v_{PV} + i_{PV}R_S) \quad (3.1)$$

Where:

$$f(v_j) = \frac{v_j}{R_{sh}} + i_{sat} \left(e^{\frac{v_j}{nv_t}} - 1 \right) \approx \frac{v_j}{R_{sh}} + i_{sat} e^{\frac{v_j}{nv_t}} \quad (3.2)$$

The parameters are: n – ideality factor [51], i_{sat} – saturation current, v_t – thermal voltage,

$v_t = \frac{kT}{q}$ (k – the Boltzmann constant, T – temperature in °K, q – the electron charge)

Let us define the small signals $\hat{v}_j, \hat{i}_{ph}, \hat{v}_{PV}, \hat{i}_{PV}$ which are perturbations of the large steady signals $V_j, I_{ph}, V_{pv}, I_{pv}$ respectively:

$$v_j = V_j + \hat{v}_j, \quad i_{ph} = I_{ph} + \hat{i}_{ph}, \quad v_{PV} = V_{PV} + \hat{v}_{PV}, \quad i_{PV} = I_{PV} + \hat{i}_{PV} \quad (3.3)$$

Then it can be derived that:

$$v_j = v_{pv} + i_{pv}R_S \Rightarrow V_j + \hat{v}_j = \underbrace{V_{PV} + I_{PV}R_S}_{V_j} + \underbrace{\hat{v}_{PV} + \hat{i}_{PV}R_S}_{\hat{v}_j} \quad (3.4)$$

The function $f(v_j)$ can be expanded using a Taylor series in the region of V_j :

$$f(V_j + \hat{v}_j) = \frac{M(V_j + \hat{v}_j)}{R_{sh}} + i_{sat} \left(e^{\frac{V_j + \hat{v}_j}{nv_t}} - 1 \right) = \underbrace{\frac{V_j}{R_{sh}} + i_{sat} \left(e^{\frac{V_j}{nv_t}} - 1 \right)}_{f(V_j)} + \left(\frac{1}{R_{sh}} + \frac{i_{sat}}{nv_t} e^{\frac{V_j}{nv_t}} \right) \hat{v}_j + \dots \quad (3.5)$$

The second term of this Taylor series is linear and it defines r_{pvd} :

$$\frac{1}{r_{pvd}} \stackrel{\text{def}}{=} \frac{1}{R_{sh}} + \frac{i_{sat}}{nv_t} e^{\frac{V_j}{nv_t}} = \frac{1}{R_{sh}} + \frac{i_{sat}}{nv_t} e^{\frac{V_{pv} + I_{pv}R_S}{nv_t}} \quad (3.6)$$

If R_{sh} is neglected then:

$$r_{pvd} = \frac{nv_t}{i_{sat}} e^{-\frac{V_{pv} + I_{pv}R_S}{nv_t}} \quad (3.7)$$

The small-signal model of PV generator is illustrated in Figure 3.2.

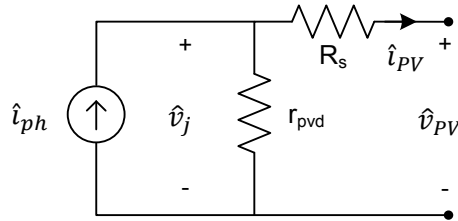


Figure 3.2 Small-signal model of PV generator.

This model is described by:

$$\hat{i}_{PV} = \hat{i}_{ph} - \frac{\hat{v}_j}{r_{pvd}} = \hat{i}_{ph} - \frac{\hat{v}_{PV} + \hat{i}_{PV}R_S}{r_{pvd}} \quad (3.8)$$

The PV generator current \hat{i}_{PV} can be described as an explicit linear function of the applied voltage:

$$\hat{i}_{PV} = \frac{\hat{i}_{ph}r_{pvd} - \hat{v}_{PV}}{r_{pvd} + R_S} \quad (3.9)$$

There is a relation between the used in [49] r_{pv} and r_{pvd} , which can be seen from their definitions (even though in definition of r_{pv} the R_{sh} and n were neglected):

$$r_{pvd} = -R_s - r_{pv} \tag{3.10}$$

Since it is possible to determine both R_s and r_{pv} , this relation allows finding the value of the internal PV generator’s parameter r_{pvd} .

3.2 Derivation of a small-signal model of a PV system

This section describes the derivation of a small-signal state-space model of a PV system that includes a PV source, a dc-dc boost converter and an emulated load controller. The emulated load controller was chosen so that approximate tracking of the MPP could be achieved with a linear controller. The system is shown in Figure 3.3. It can be seen that the detailed model of the PV source is included; also there is no assumption of constant voltage at the final output of the system (instead it is treated as a system output) and the physical output current i_o is treated as an input to the dynamic model. The MPPT block was not modelled. It is assumed that a slow-acting MPPT controller will provide a constant reference V_{ref} for comparatively long periods of time, but nevertheless V_{ref} is considered as an input of the system.

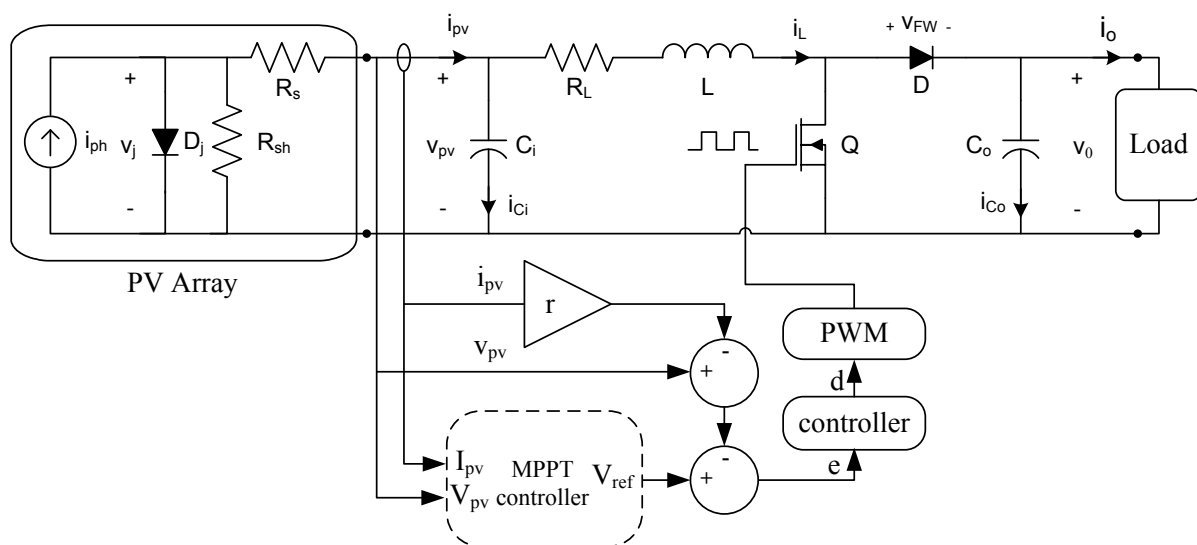


Figure 3.3 The modelled PV system.

Under the assumption that the switching action can be ignored and switching function averages based on the duty-cycle can be used, the basic circuit equations that describe the boost dc-dc converter are:

$$\begin{cases} i_{C_i} = C_i \frac{d}{dt} v_{PV} = i_{PV} - i_L \\ i_{C_o} = C_o \frac{d}{dt} v_o = i_L(1 - d) - i_o \\ v_L = L \frac{d}{dt} i_L = v_{PV} - (1 - d)(v_o + V_{FW}) - R_L i_L \end{cases} \quad (3.11)$$

Similarly to (3.3), let us define the small signals $\hat{v}_L, \hat{i}_L, \hat{v}_o, \hat{i}_o, \hat{v}_{ref}, \hat{d}$ which are perturbations of the large steady signals $V_j, I_L, V_o, I_o, V_{ref}, D$ respectively:

$$v_L = V_L + \hat{v}_L, \quad i_L = I_L + \hat{i}_L, \quad v_o = V_o + \hat{v}_o, \quad i_o = I_o + \hat{i}_o, \quad v_{ref} = V_{ref} + \hat{v}_{ref}, \quad d = D + \hat{d} \quad (3.12)$$

It should be noticed that, since the steady-state average current through C_i will be zero:

$$I_L = I_{PV} \quad (3.13)$$

Substituting (3.12) and (3.13) in (3.11) yields a small-signal description of the boost dc-dc converter:

$$\begin{cases} C_i \frac{d}{dt} \hat{v}_{PV} = \hat{i}_{PV} - \hat{i}_L \\ C_o \frac{d}{dt} \hat{v}_o = -I_{PV} \hat{d} + (1 - D) \hat{i}_L - \underbrace{\hat{i}_L \hat{d}}_{\text{non-linear term}} - \hat{i}_o \\ L \frac{d}{dt} \hat{i}_L = \hat{v}_{PV} - (1 - D) \hat{v}_o + (V_o + V_{FW}) \hat{d} + \underbrace{\hat{v}_o \hat{d}}_{\text{non-linear term}} - R_L \hat{i}_L \end{cases} \quad (3.14)$$

Neglecting the products of two perturbation terms (since they are small), the nonlinear terms are removed and a linearised small-signal model results:

$$\begin{cases} C_i \frac{d}{dt} \hat{v}_{PV} = \hat{i}_{PV} - \hat{i}_L \\ C_o \frac{d}{dt} \hat{v}_o = -I_{PV} \hat{d} + (1 - D) \hat{i}_L - \hat{i}_o \\ L \frac{d}{dt} \hat{i}_L = \hat{v}_{PV} - (1 - D) \hat{v}_o + (V_o + V_{FW}) \hat{d} - R_L \hat{i}_L \end{cases} \quad (3.15)$$

The chosen controller, as shown in Figure 3.4, consists of a gain A_c , an integrator and a first-order low pass filter with a cut-off frequency ω_f in cascade connection. This controller provides sufficiently good performance and allows keep the model relatively simple.

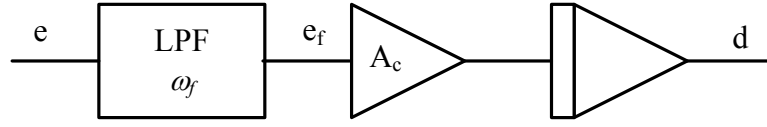


Figure 3.4 The controller of the PV system.

The equations that describe the controller are:

$$\begin{cases} \frac{1}{A_c} \frac{d}{dt} d = e_f \\ \frac{1}{\omega_f} \frac{d}{dt} e_f = \underbrace{v_{ref} - (v_{PV} - r i_{PV})}_e - e_f \end{cases} \quad (3.16)$$

Since the controller is linear the small-signal equations are the same as for large signal:

$$\begin{cases} \frac{1}{A_c} \frac{d}{dt} \hat{d} = \hat{e}_f \\ \frac{1}{\omega_f} \frac{d}{dt} \hat{e}_f = \hat{v}_{ref} - (\hat{v}_{PV} - r \hat{i}_{PV}) - \hat{e}_f \end{cases} \quad (3.17)$$

Combining (3.15) and (3.17) and substituting (3.9) provide the state-space small-signal model

of the PV system with the state variables \hat{v}_{PV} , \hat{v}_o , \hat{i}_L , \hat{d} , \hat{e}_f and the inputs \hat{i}_{ph} , \hat{i}_o , \hat{v}_{ref} :

$$\frac{d}{dt} \begin{bmatrix} \hat{v}_{PV} \\ \hat{v}_o \\ \hat{i}_L \\ \hat{d} \\ \hat{e}_f \end{bmatrix} = \begin{bmatrix} -\frac{1}{(r_{pvd}+R_S)C_i} & 0 & -\frac{1}{C_i} & 0 & 0 \\ 0 & 0 & \frac{1-D}{C_o} & -\frac{I_{PV}}{C_o} & 0 \\ \frac{1}{L} & -\frac{1-D}{L} & -\frac{R_L}{L} & \frac{V_o+V_{FW}}{L} & 0 \\ 0 & 0 & 0 & 0 & A_c \\ -\frac{(r_{pvd}+R_S+r)\omega_f}{r_{pvd}+R_S} & 0 & 0 & 0 & -\omega_f \end{bmatrix} \begin{bmatrix} \hat{v}_{PV} \\ \hat{v}_o \\ \hat{i}_L \\ \hat{d} \\ \hat{e}_f \end{bmatrix} + \begin{bmatrix} \frac{r_{pvd}}{(r_{pvd}+R_S)C_i} & 0 & 0 \\ 0 & -\frac{1}{C_o} & 0 \\ 0 & 0 & 0 \\ 0 & 0 & 0 \\ \frac{r r_{pvd} \omega_f}{(r_{pvd}+R_S)} & 0 & \omega_f \end{bmatrix} \begin{bmatrix} \hat{i}_{ph} \\ \hat{i}_o \\ \hat{v}_{ref} \end{bmatrix} \quad (3.18)$$

3.3 Verification of the small-signal model of the PV system

In order to verify the derived model, a Simulink time-domain simulation of the PV system was prepared. The simulated system is shown in Figure 3.5. In this simulation the PV source model from [52] was employed.

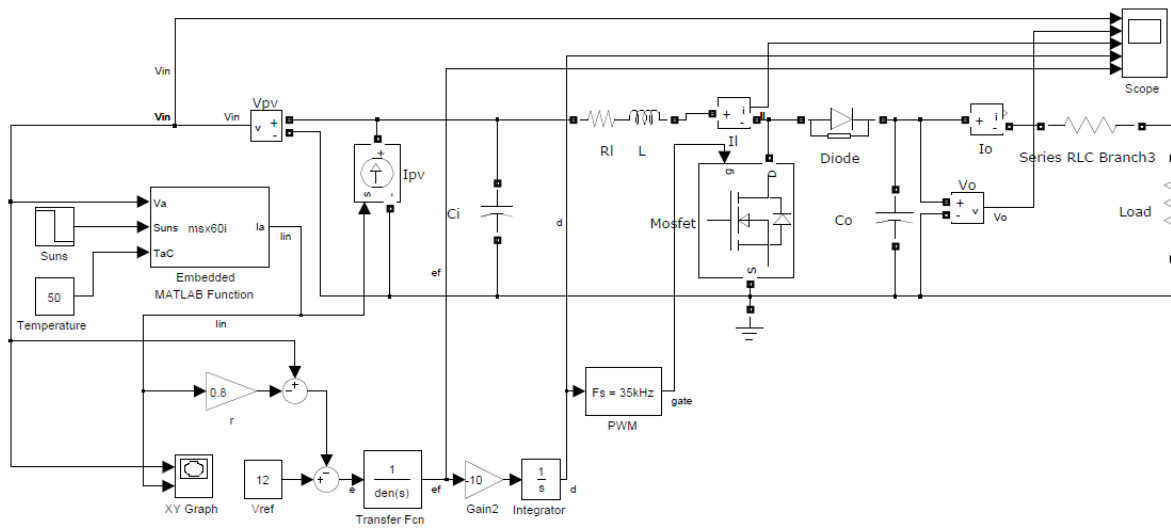
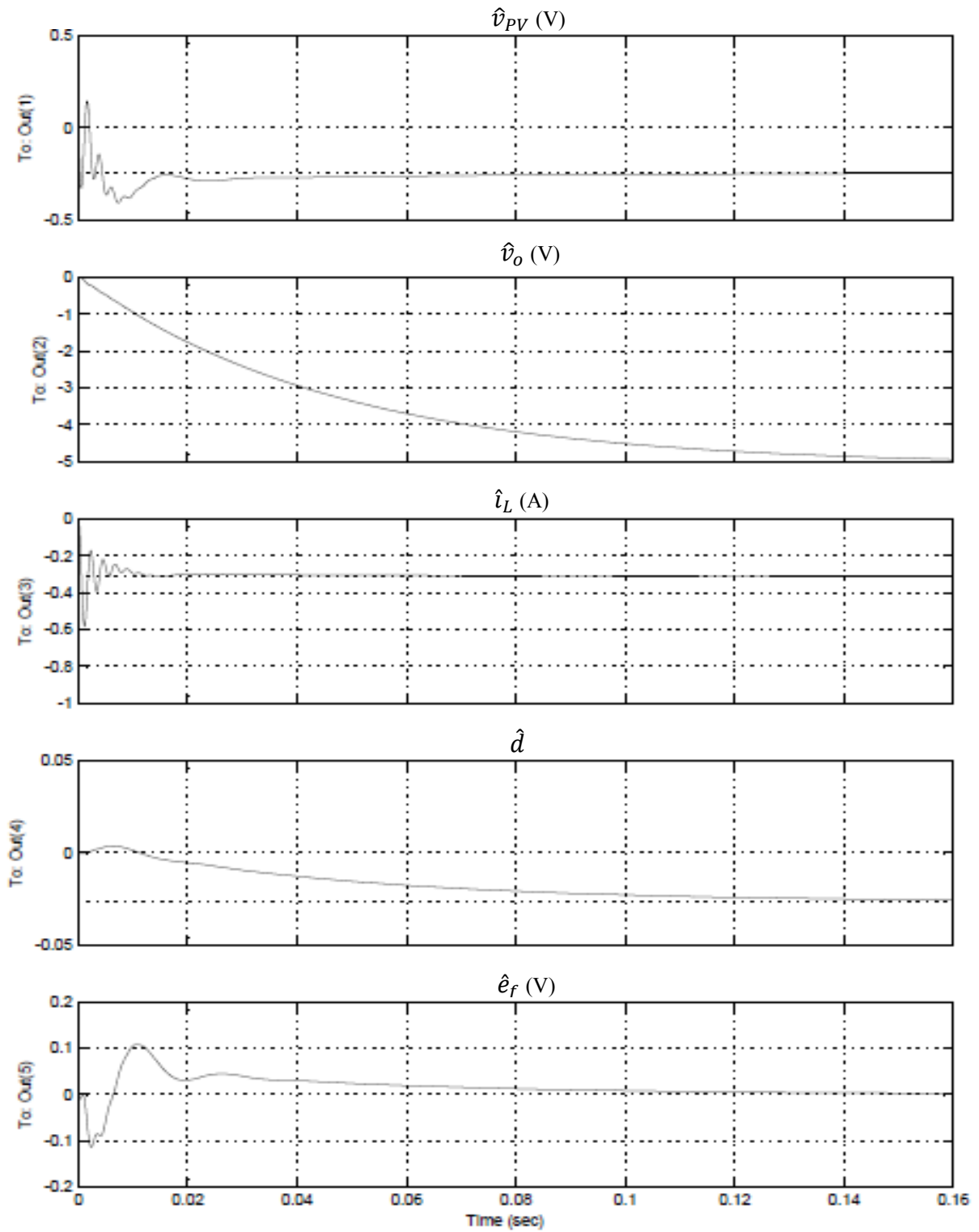


Figure 3.5 Simulink simulation of the PV system.

The simulation and the state-space model used the following parameters: $L = 380\mu\text{H}$, $R_L = 20\text{m}\Omega$, $C_i = 330\mu\text{F}$, $C_o = 1000\mu\text{F}$, $V_{fw} = 0.6\text{V}$, $r = 0.8\Omega$, $\omega_f = 300\text{rad/sec}$, $A_c = -10$. The state-space model required the presumed operating point to be defined which was done so in terms of the following values: $r_{pvd} = 3.72\Omega$, $R_s = 0.284\Omega$, $D = 0.7$, $I_{pv} = 3.5\text{A}$, $V_o = 48\text{V}$.

The simulation results for constant output current and a negative step of -0.1 Sun in irradiation are shown in Figure 3.6, where all state variables of the system can be observed after the irradiation step. In addition, simulations for a constant output voltage and for a resistive load were performed for the same irradiation step. The state-space model was modified to simulate these loads. The results of these simulations are shown in Figure 3.7 and Figure 3.8. It can be seen that the results of the state-space model are close to the results of time-domain simulations in all three cases and that the state-space model provide a good description of the system. Also, it can be seen that the state-space model provides representation of the averaged small-signals while in the time-domain simulation the switching ripples and the large signals are shown. As the state-space model represent only the

small perturbation signals all signals start from zero while in the time domain simulations the signals start from previous steady state values.



(a)

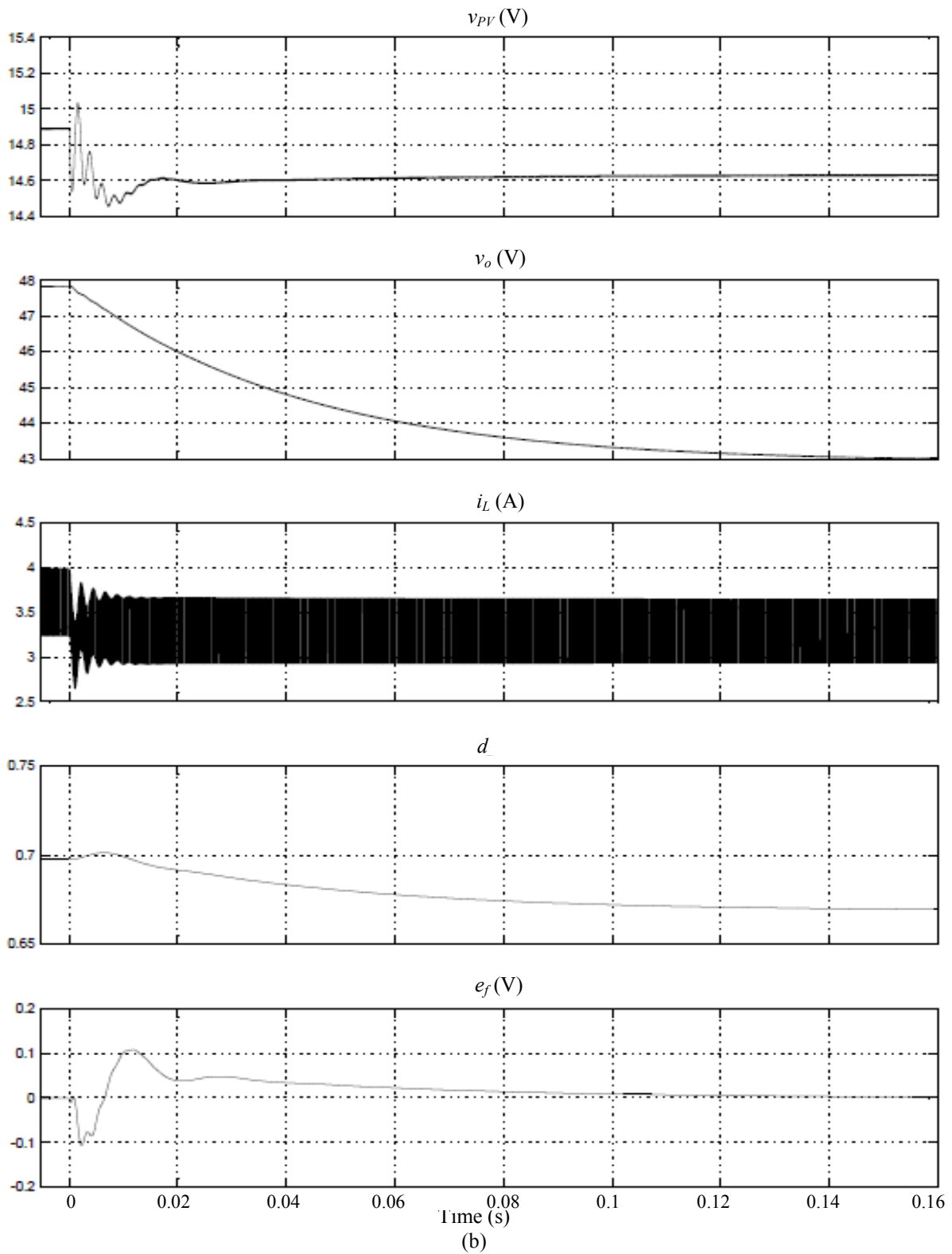
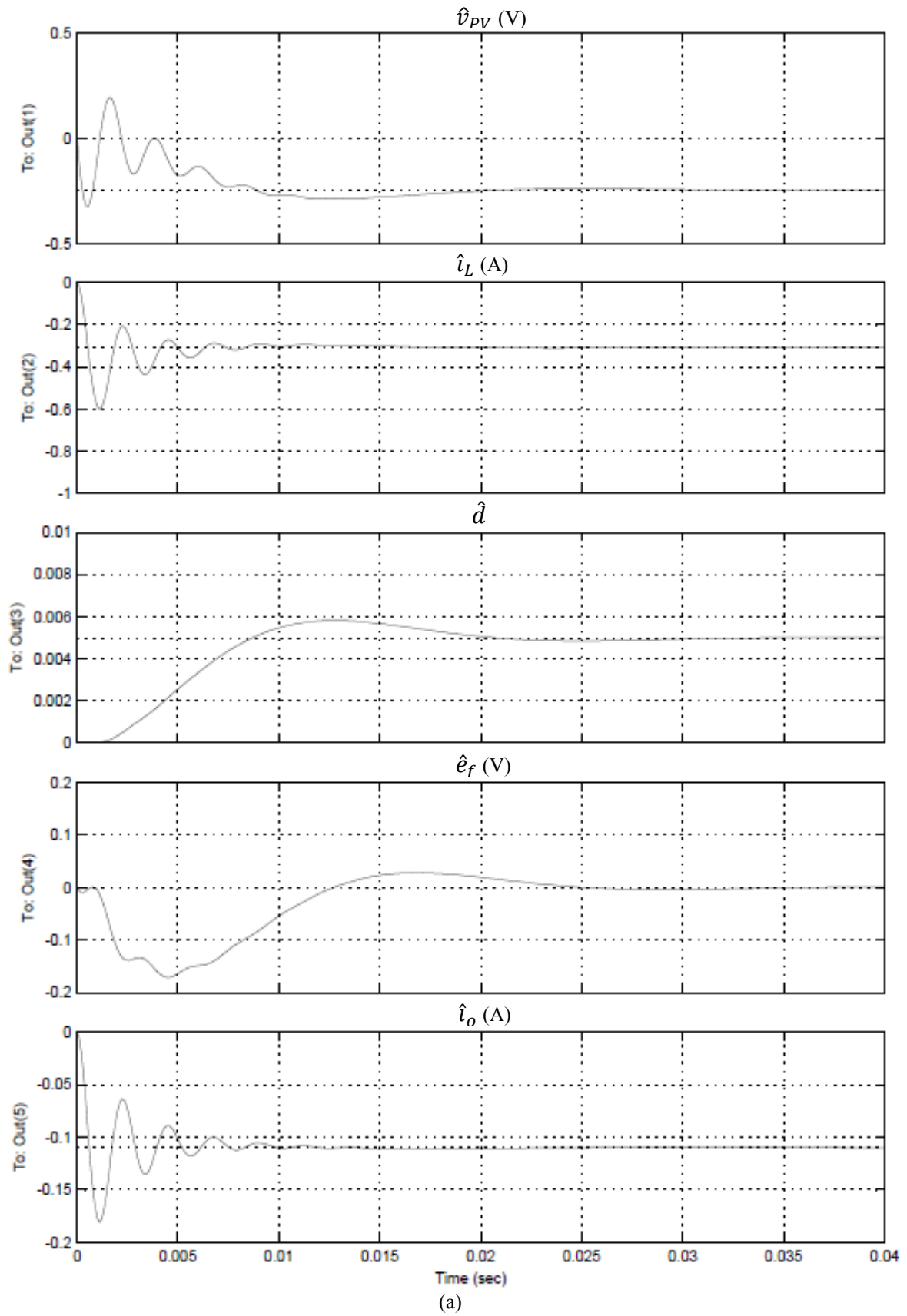


Figure 3.6 Simulation results for constant output current i_o : top to bottom: v_{PV} , v_o , i_L , d , e_f .
 (a) state-space model (b) time domain simulation.



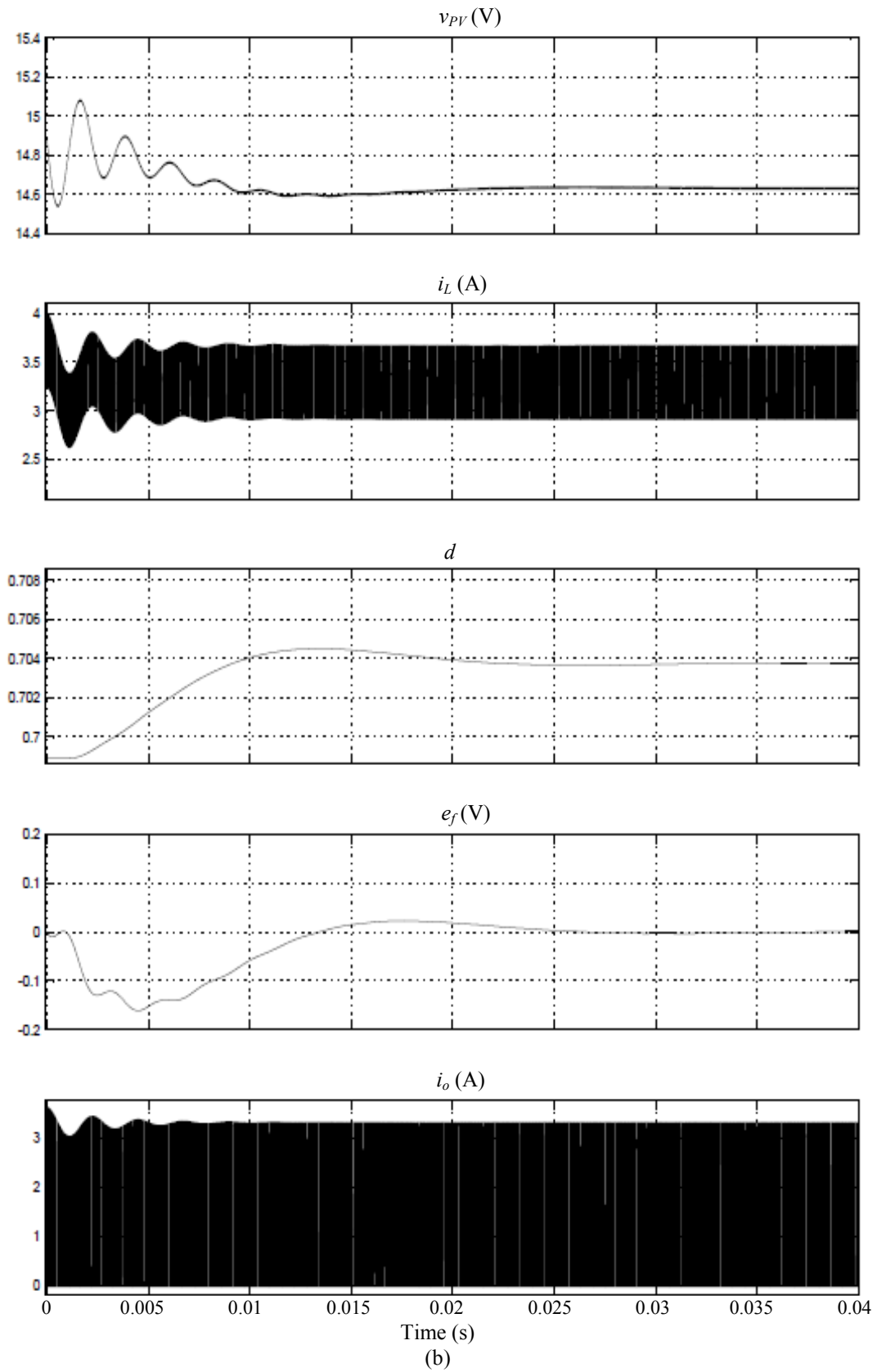
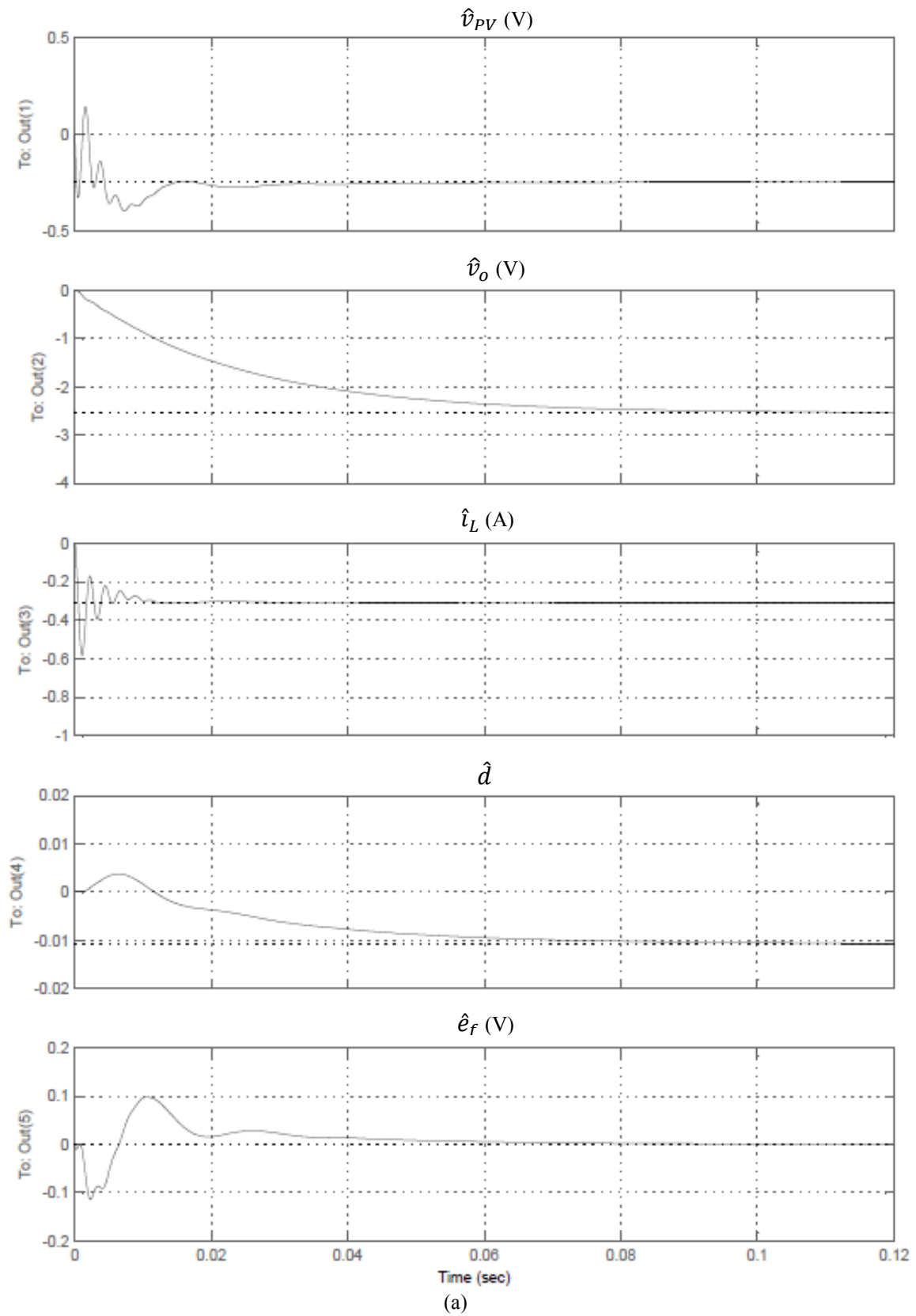


Figure 3.7 Simulation results for constant output voltage v_o : top to bottom: v_{PV} , i_L , d , e_f , i_o .
 (a) state-space model (b) time domain simulation.



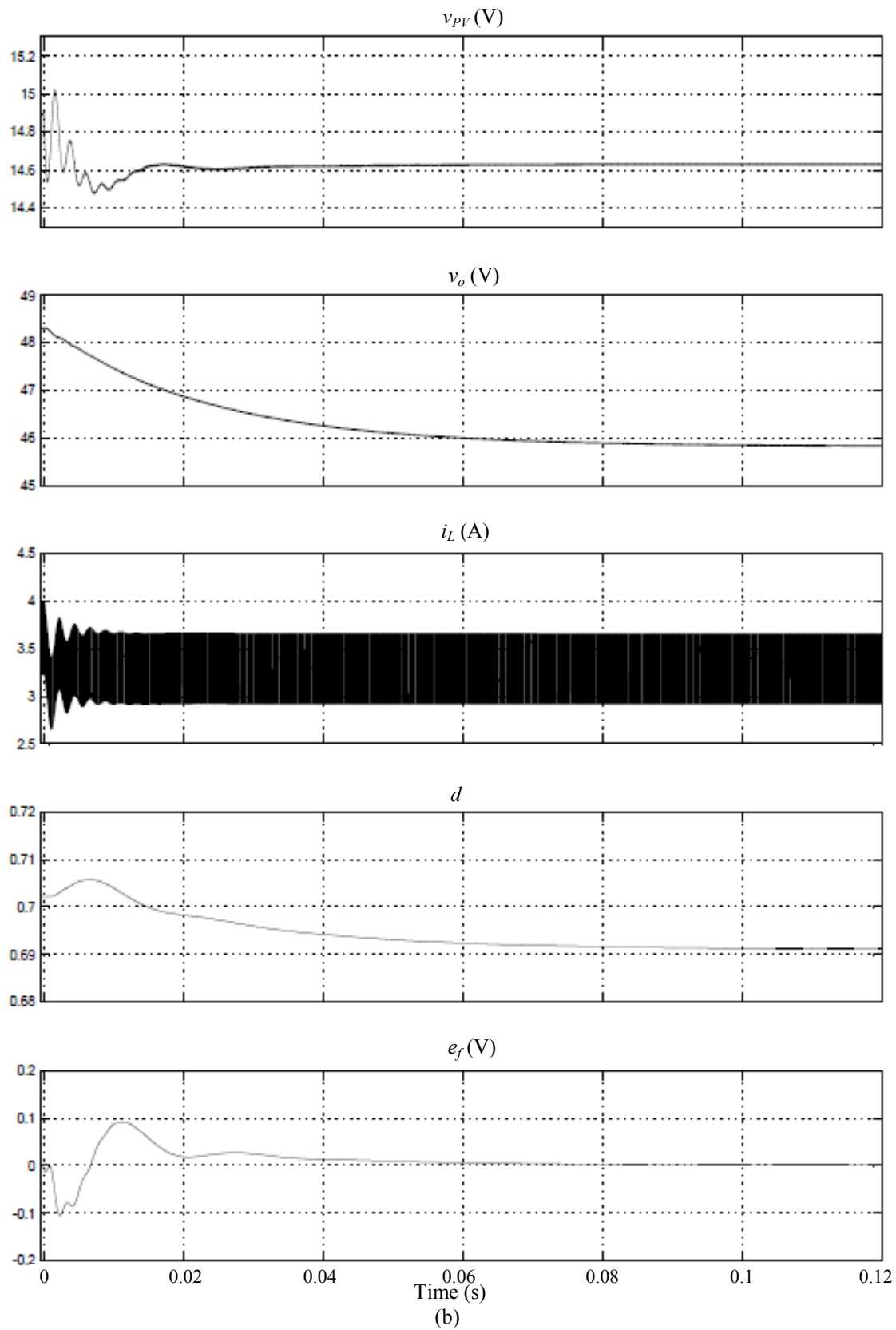


Figure 3.8 Simulation results for resistive load v_o : top to bottom: v_{PV} , v_o , i_L , d , e_f . (a) state-space model. (b) time domain simulation.

3.4 Use of Small-signal Model for Selection of Iteration Time Step for

MPPT Algorithm

As was mentioned in section 2.2.1, the time intervals between algorithm iterations should be short to allow faster tracking, but they must be longer than the settling time of the PV current and voltage (plus a signal processing filters) for reliable signal measurements. Analysis of PV system dynamics is required, therefore, to determine an appropriate time interval for the MPPT algorithm. A modified version of the model developed in this chapter was used for this purpose [53]. The modifications involved choosing a resistive load, R_{Load} , as the example load and setting the irradiation to be constant:

$$\frac{d}{dt} \begin{bmatrix} \hat{v}_{PV} \\ \hat{v}_o \\ \hat{i}_L \\ \hat{d} \\ \hat{e}_f \end{bmatrix} = \begin{bmatrix} -\frac{1}{(r_{pvd}+R_S)C_i} & 0 & -\frac{1}{C_i} & 0 & 0 \\ 0 & -\frac{1}{R_{Load}C_o} & \frac{1-D}{C_o} & -\frac{I_{PV}}{C_o} & 0 \\ \frac{1}{L} & -\frac{1-D}{L} & -\frac{R_L}{L} & \frac{V_o+V_{FW}}{L} & 0 \\ 0 & 0 & 0 & 0 & A_c \\ -\frac{(r_{pvd}+R_S+r)\omega_f}{r_{pvd}+R_S} & 0 & 0 & 0 & -\omega_f \end{bmatrix} \begin{bmatrix} \hat{v}_{PV} \\ \hat{v}_o \\ \hat{i}_L \\ \hat{d} \\ \hat{e}_f \end{bmatrix} + \begin{bmatrix} 0 \\ 0 \\ 0 \\ 0 \\ \omega_f \end{bmatrix} \hat{v}_{ref}. \quad (3.19)$$

As in previous section, the small-signal model simulation results were compared to results of component-level large-signal simulation in Simulink with the SimPowerSystems toolbox. The large- and small-signal simulations results are shown in Figure 3.9. A good match between time domain and small-signal simulation can be noticed. It should be noted that the time-domain simulation shows the complete system signals including the switching frequency ripple components while the small-signal simulation calculates only deviations from steady-state (average) values.

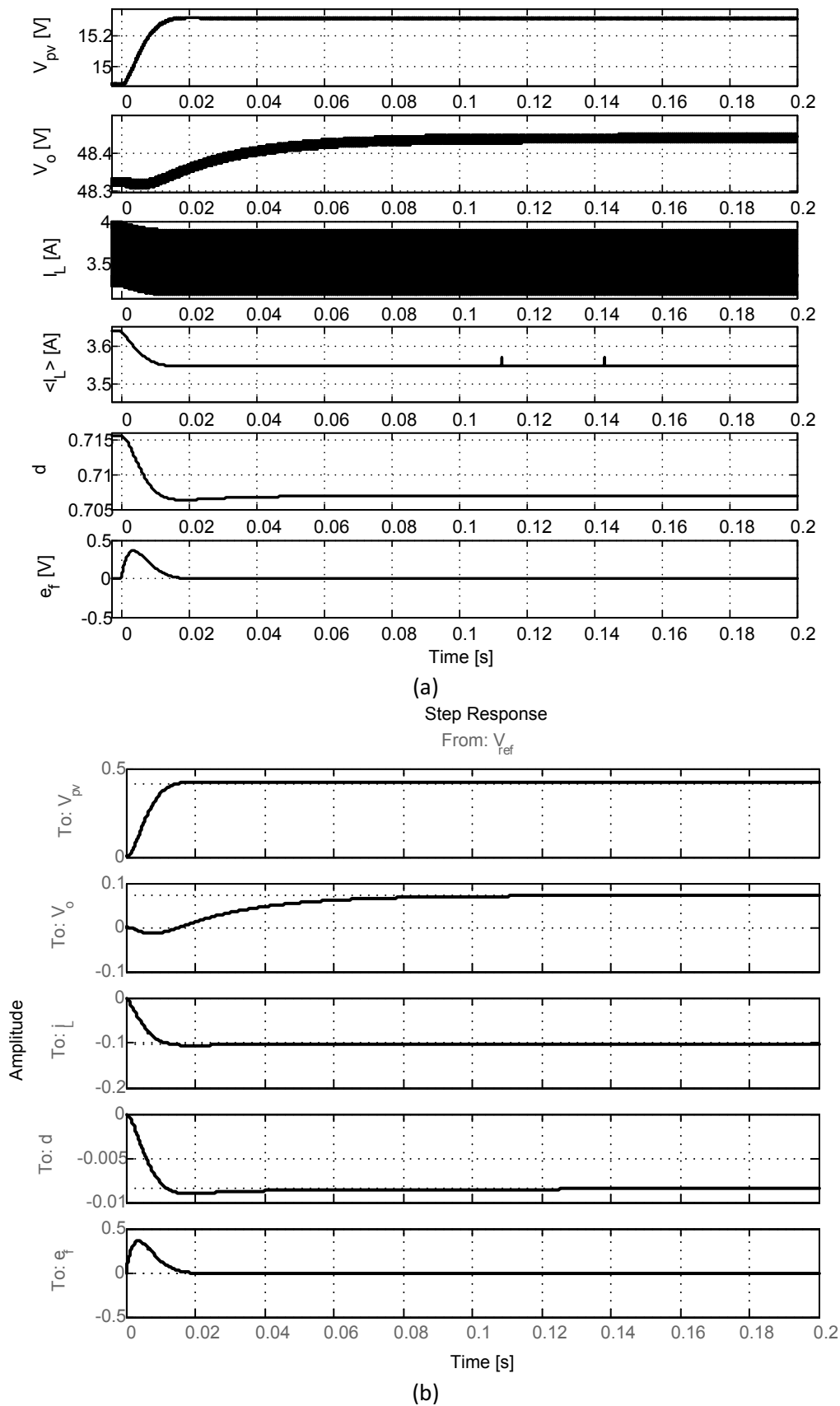


Figure 3.9 System response to a step of 0.5 V in v_{ref} . (a) Time-domain Simulink simulation, top to bottom: PV array voltage v_{pv} , output voltage v_o , inductor current i_L , average inductor current $\langle i_L \rangle$, duty cycle d , filtered error e_f . (b) small-signal model, top to bottom: PV array voltage v_{pv} , output voltage v_o , inductor current i_L , duty cycle d , filtered error e_f .

This simulation shows that the signals v_{pv} , i_L , d , and e_f settle after nearly the same time which is approximately 25 ms after the perturbation but that the output voltage v_o takes longer time to settle at approximately 80 ms. Even though the whole system settling time is long (80 ms), the signals of interest for the MPPT algorithm (PV voltage and current) converge significantly faster (25 ms) and the time interval between iterations can be set to a shorter time than the whole system settling time. Figure 3.10 shows Simulink simulation results of system response to a step in v_{ref} that occurs before output voltage v_o reaches steady state. The first step of 0.5 V occurs at time 0 s and the second step occurs after 25 ms when the PV voltage v_{pv} reaches the steady state but output voltage v_o is still changing. It can be seen that after the second step the PV voltage again converges within 25 ms. Hence the time interval does not need to be long enough to allow full system convergence to steady-state (i.e. the output voltage) but must be long enough to allow convergence of the PV voltage and current.

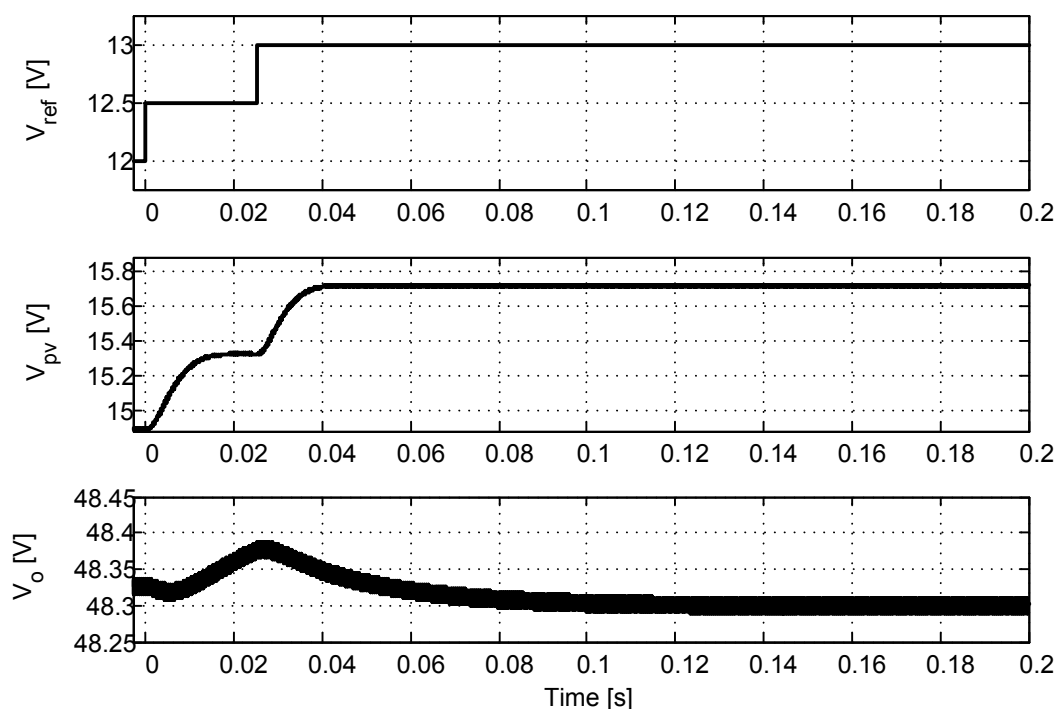


Figure 3.10 Response of the system to a step in v_{ref} that occurs before output voltage v_o reaches steady state.

3.5 Conclusions on small-signal modelling of PV systems

A linear model of a PV source, dc-dc boost converter and a controller with MPPT capability is presented. This model allows analysis of signals in the PV system for changing irradiation, output current and output voltage and allows derivation of transfer functions of the PV system. The model is suitable for inclusion in larger system models for power system stability studies. The linear model is verified by means of comparing its results with results obtained by full time-domain simulation of the PV system in various cases.

Chapter 4

Noise influence on Maximum Power Point Tracking

4.1 Introduction

A common form of the algorithm is perturb and observe (P&O) [14]-[21] in which small changes of operating point are used to test whether operation is at a maxima by observing changes in the measured power yield. The difference in power yield between two measurements, on which the decision of the MPPT algorithm is based, is small; therefore, it is possible for noise in the measured signals to affect the quality of the tracking of the MPP. Thermal random noise can be expected in measured voltage and in the current to voltage transducer for current measurement. Both the current and voltage are expected to have some ripple because of the switch-mode power converter. Measurement synchronized to the switching cycle can alleviate some of the effects of switching noise [54], but using this technique will increase the cost of the system. Quantization noise will also be present because of the ADC sampling before application of the MPPT algorithm. It is good practice to filter the noise out but the quantization and low frequency components of the noise cannot be filtered. In order to achieve better tracking, time intervals between algorithms iterations should be as short as the system's dynamics allow [53]. Switching frequency can be much closer to the algorithm iteration frequency in systems with fast dynamics such as those based on sliding mode control [55] or [56] (which also makes use of an emulated load control method [41]). In these fast systems it is difficult to filter out the switching ripple and not insert a delay that would degrade the performance. In grid connected systems, low frequency harmonics that are difficult to filter can propagate from the grid to the PV. The effect of the grid harmonics is similar to the effect of switching ripple. In addition, ripple levels in the

system may increase with the ageing of electrolytic capacitors [57]. For the above described reasons even after filtering, considerable noise can remain and it is important that the MPPT algorithm will operate efficiently even when noise is present in measured signals.

Despite its potential importance, the impact of measurement noise on MPPT algorithms has received much less attention than refinements to the algorithms themselves. In the studies that do exist, measurement noise is assumed to be Gaussian white noise [36],[37],[58] rather than a combination of random and systematic factors. In one of the few analytical studies [36], a probabilistic model accounting for noise was used to analyze steady-state accuracy of the P&O- ΔV algorithm [16]-[18]. Statistical representation of noise and its impact on the P&O- ΔV algorithm have shown that bias is introduced and the steady-state accuracy is impaired. The analysis explains some phenomena in operation of the P&O algorithm, but does not provide quantitative results and only one version of the P&O algorithm is discussed there. Quantitative assessment of MPPT steady-state operation in the presence of noise were reported in [37] using a Markov chain model for the P&O- ΔV_{ref} algorithm [19]-[21]. This Markov chain model is not suitable for all types of MPPT algorithms such as variable step algorithms [22] that do not fit the fixed node Markov chain model. In ideal conditions with no noise present there can be little to distinguish between some variants of the P&O algorithm (for example, P&O- ΔV [16]-[18] and P&O- ΔV_{ref} [19]-[21]) as they perform similarly. The dynamic performance of three-point weight P&O [23] and Inc [39] were compared in the presence of noise using simulations in [58]. This work [58] focused on transient rather than on steady-state performance and showed the disadvantage of the modified P&O algorithm [23] during irradiation transients.

The work to be reported in this chapter aims to evaluate and quantify the impact of measurement noise on most commonly used existing MPPT algorithms (P&O- ΔV_{ref} , P&O- ΔV , Inc and dP-P&O) in order to compare the algorithms impartially, to recognize most noise

immune algorithms versions, to provide some insight on the mechanisms of noise effect and to help adjust the MPPT algorithm's parameters for better efficiency. In addition, this work establishes simulation method for testing algorithms in the presence of noise that will be used to test new algorithms and the results will be used to compare the performance of the new algorithm to existing ones.

The work begins with measurement of noise in an experimental PV system. Next, a realistic noise model is synthesized and matched to the measured noise. A simplified model with Gaussian noise is established for comparison with the full model in order to assess the assumption that noise can be modelled as Gaussian. Noise models are used in simulations of four widely-applied MPPT algorithms (P&O- ΔV_{ref} , P&O- ΔV , Inc and dP-P&O). Different variations of the P&O algorithm P&O- ΔV [16]-[18] and P&O- ΔV_{ref} [19]-[21] are tested separately. The steady-state operation is simulated with a range of step sizes at various irradiances and the divergence of the operating point from the real MPP observed in terms of power foregone. The simulations are configured to allow observation of signals before noise is added. Finally, conclusions are drawn on selection of MPPT algorithms and step size adjustment in the presence of measurement noise.

4.2 Observation and representation of measurement noise

A realistic simulation of the operation of MPPT algorithms should include the noise of the measured signals. Noise in PV voltage and current signals typically has three main origins: thermal additive white Gaussian noise, ripple components from the power converter and quantization noise from the ADC. In order to obtain realistic noise levels, the voltage and current of a PV panel (the feedback variables for an MPPT algorithm) were recorded from an experimental PV system. The schematic of the dc-dc converter is shown in Figure 4.1. The switching frequency of the converter was set to 35 kHz and the output voltage held at 48 V

with a dc load. In order to achieve long measurement for statistical analysis at stable conditions without dependence on atmospheric variations, the converter was connected to a PV emulator consisting of power supply GW GPS-4303 (operating in constant current mode) in parallel with 30 serially connected diodes U1520. The converter was also connected to PV panel of type BP SX40M and the voltage and current waveforms were verified to have the same shapes. The voltage was measured by a simple voltage divider. The current was measured by current transducer of type LTS15-NP with the signal conditioning circuit of Figure 4.2. The voltage and current signal levels were adjusted to match the operating ranges to the level of 0-5 V and the signals were sampled by an analogue to digital converter of type NI PCI-6024E of 12 bits. The signals were recorded as they are seen by the MPPT controller with an effective resolution of 11 bits over the uni-polar range.

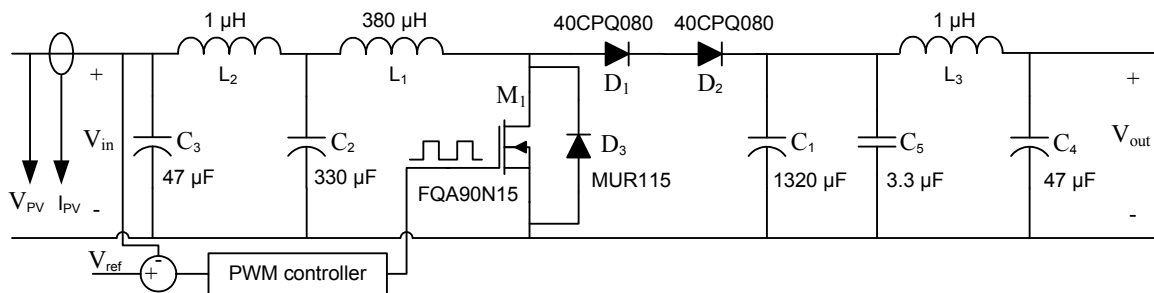


Figure 4.1 Schematic of dc-dc converter used for observation of measurement noise.

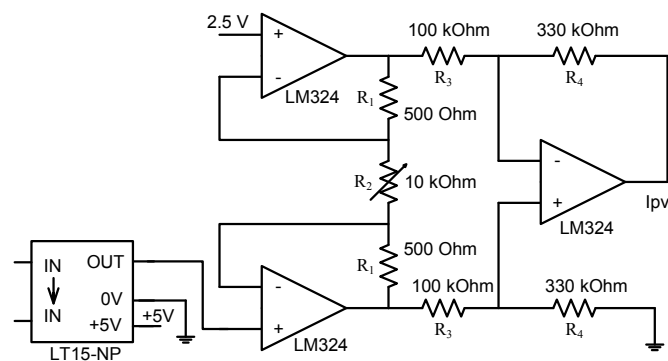


Figure 4.2 Current measurement circuit.

The PV voltage and current waveforms observed by an oscilloscope in the experimental

setup are shown in Figure 4.3. Histograms of the PV voltage and current waveforms once sampled by the ADC are shown in Figure 4.4. The histograms are based on 65,000 measurements of steady operation where the mean PV voltage and current are 17.78 V and 3.56 A respectively and the standard deviations of the signals are 27 mV and 7.5 mA respectively. It can be seen that the voltage signal histogram has two peaks that are caused by PV converter switching ripple. Each peak represents a slightly different PV voltage corresponding to each switch state. The relative height of the peaks relates to the duty cycle. In some implementations it is possible to reduce switching ripple noise by synchronizing the measurement with the PWM signal [54], but this feature was not available in the tested system. The histogram of the power calculated from the measured voltage and current is also shown in Figure 4.4.

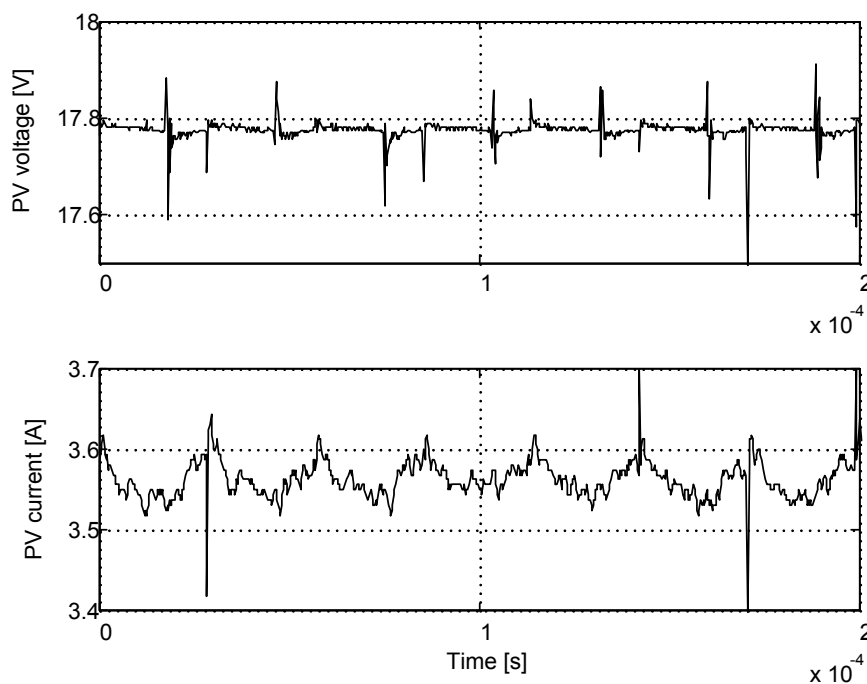


Figure 4.3 Experimentally measured PV voltage and current shapes.

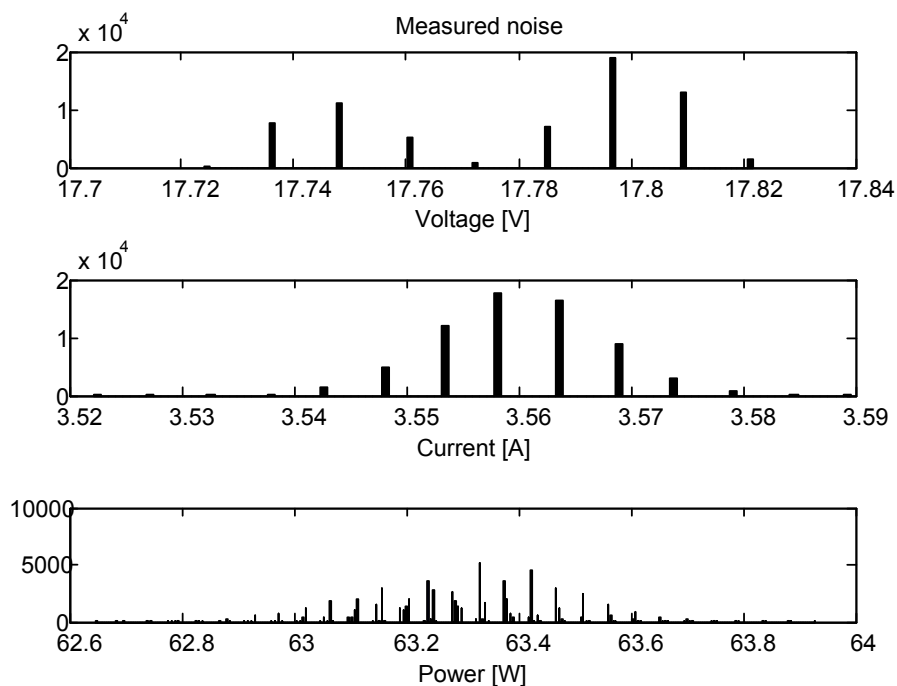


Figure 4.4 Histograms of experimentally measured PV voltage and current and calculated power.

The measured noise was reproduced in a simulation in Matlab using random number generation functions. The histograms of the signals with simulated noise representative of the signals measured in the experimental system are shown in Figure 4.5. The histograms in Figure 4.4 and Figure 4.5 are not identical but all of the noise components in the experimental measurements are well represented in the simulated noise. The simulated noise has slightly different quantization. However, it is the relationship between the average signal level and the middle of the quantization interval that is more important than the absolute quantization level and this changes anyway as the operating point moves.

For comparison, a simplified noise model was established using a Gaussian noise to give the same mean and standard deviation. The output of this model is shown in Figure 4.6. This Gaussian noise model will be used to establish whether similar results to the results of the more realistic three-component noise model are obtained and whether Gaussian

approximation that was used in the previous studies [[36],[37],[58]] are reasonable. If so, simpler simulations will suffice to assess algorithm performance under noise.

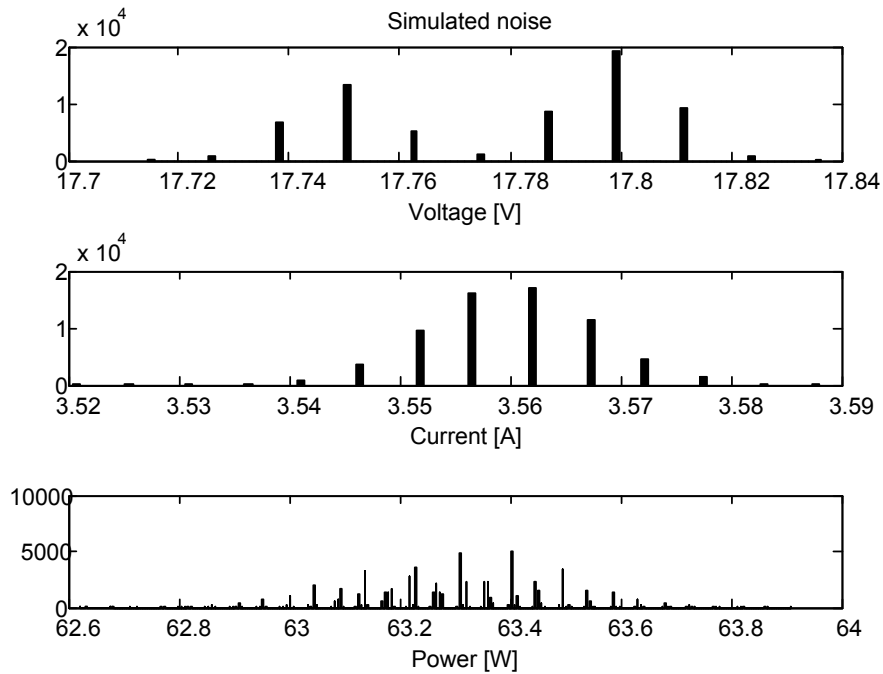


Figure 4.5 Histograms of simulated realistic PV voltage and current and calculated power.

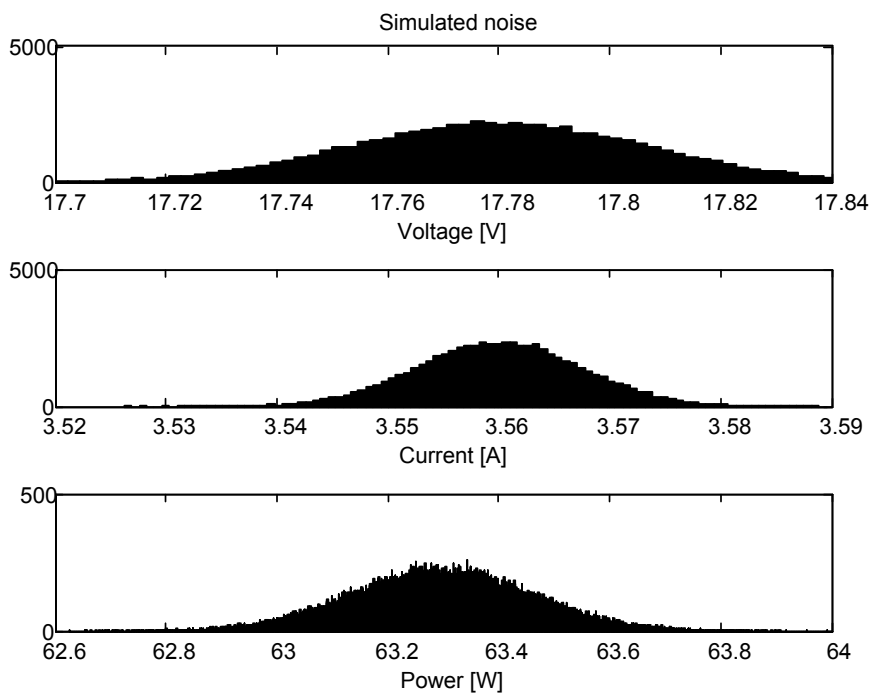


Figure 4.6 Histograms of simulated Gaussian PV voltage and current and calculated power.

4.3 Simulation method

It is difficult to keep experimental conditions the same for a range of tests so that reliable comparisons can be made. Thus simulation is used in this work for analysis of different algorithms. The simulation technique is based on recording the PV voltage and current signals before artificial computer generated noise is added to the signals. Thus the noise-less signals can be observed (and further data such as power can be calculated) for operation of the MPPT algorithm in a noise-affected environment. A flowchart of simulation procedure is shown in Figure 4.7.

The PV array was simulated using the model described in [52]. The MPPT algorithm sets the reference value for the PV panel voltage, V_{ref} . Rather than simulate the full converter and voltage control loop of Figure 4.1, a simplified model in which the converter applies a controlled voltage source to the PV panel and that voltage is assumed to reach the voltage V_{ref} before the next algorithm iteration. This assumption is realistic because the time between MPPT iterations should be larger than the settling time of the converter dynamics in order to achieve proper MPPT operation [34],[53].

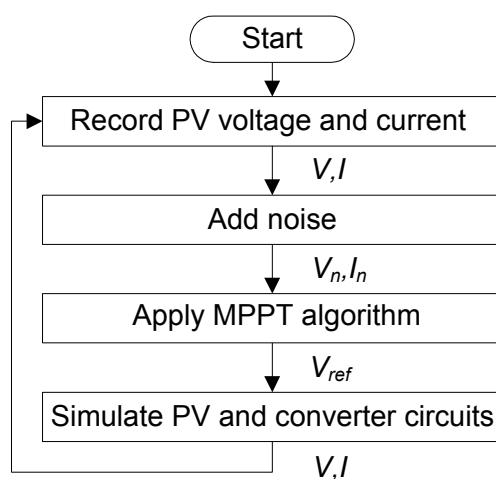


Figure 4.7 Flowchart of simulation procedure. (V and I are observations without noise. V_n , and I_n are observations with noise.)

4.4 Results

Simulations of steady-state operation at the MPP of the four previously described algorithms were performed using the realistic simulated noise and with equivalent Gaussian noise. In addition, the P&O algorithm without noise was simulated for reference. The efficiency of different algorithms with different step sizes ΔV_{ref} (from 13 mV to 0.9 V) are reported for three irradiation levels in Figure 4.8: 1 Sun with maximal power $P_{MPP}=60.47$ W at the voltage $V_{MPP}=17.01$ V, 0.5 Sun with $P_{MPP}=29.76$ W at $V_{MPP}=16.74$ V and 0.1 Sun with $P_{MPP}=5.46$ W at $V_{MPP}=15.41$ V. This data is also presented as power loss percentage in Table 4.1-Table 4.3.

It can be seen from Figure 4.8 that measurement noise affects the performance of all of the tested algorithms and that the noise influence is more significant at smaller step-sizes and at lower irradiances in comparison to the results without noise.

The algorithms were also tested using both realistic and Gaussian noise in order to evaluate the assumption of Gaussian noise in previously developed models. At a high irradiation of 1 Sun, the efficiencies for Gaussian noise were very similar to the efficiencies for realistic noise for the P&O- ΔV_{ref} and dP-P&O algorithms and for P&O- ΔV and Inc algorithms significant difference is observed only at very small step size of 13 mV. At an irradiation of 0.5 Sun, more differences can be seen at small step sizes and at low irradiation of 0.1 Sun differences between simulation with Gaussian and realistic noise can be seen at larger step sizes.

Table 4.1 Algorithms power losses [%] at 1 Sun, $P_{MPP} = 60.47$ W, $V_{MPP} = 17.01$ V.

ΔV_{ref} [V]	P&O no noise	P&O- ΔV		P&O- ΔV_{ref}		dP-P&O		Inc	
		realistic noise	Gaussian noise	realistic noise	Gaussian noise	realistic noise	Gaussian noise	realistic noise	Gaussian noise
0.013	0.01	32.1	37	0.08	0.08	0.22	0.22	30	37
0.05	0.01	0.33	0.34	0.08	0.09	0.22	0.23	0.3	0.33
0.1	0.01	0.1	0.1	0.1	0.1	0.24	0.24	0.1	0.1
0.2	0.05	0.15	0.15	0.15	0.14	0.28	0.27	0.15	0.15
0.3	0.12	0.22	0.22	0.22	0.22	0.33	0.33	0.22	0.22
0.5	0.34	0.38	0.38	0.38	0.38	0.52	0.51	0.36	0.36
0.9	1.11	1.21	1.21	1.11	1.11	1.22	1.22	1.11	1.11

Table 4.2 Algorithms power losses [%] at 0.5 Sun, $P_{MPP} = 29.76$ W, $V_{MPP} = 16.74$ V.

ΔV_{ref} [V]	P&O no noise	P&O- ΔV		P&O- ΔV_{ref}		dP-P&O		Inc	
		realistic noise	Gaussian noise	realistic noise	Gaussian noise	realistic noise	Gaussian noise	realistic noise	Gaussian noise
0.013	0.01	20.5	23.4	0.29	0.14	0.38	0.37	18	23
0.05	0.01	0.4	0.44	0.11	0.15	0.38	0.39	0.34	0.44
0.1	0.02	0.14	0.16	0.14	0.16	0.4	0.4	0.14	0.16
0.2	0.07	0.21	0.21	0.21	0.21	0.44	0.44	0.21	0.21
0.3	0.13	0.3	0.3	0.31	0.3	0.5	0.5	0.29	0.29
0.5	0.45	0.59	0.59	0.59	0.59	0.71	0.7	0.57	0.57
0.9	1.74	1.95	1.95	1.76	1.76	1.81	1.8	1.65	1.65

Table 4.3 Algorithms power losses [%] at 0.5 Sun, $P_{MPP} = 5.46$ W, $V_{MPP} = 15.41$ V.

ΔV_{ref} [V]	P&O no noise	P&O- ΔV		P&O- ΔV_{ref}		dP-P&O		Inc	
		realistic noise	Gaussian noise	realistic noise	Gaussian noise	realistic noise	Gaussian noise	realistic noise	Gaussian noise
0.013	0.01	91.2	23.8	7.4	0.64	2	1.9	88	23
0.05	0.01	5.42	1.1	2.1	0.69	2	1.85	4.36	1.1
0.1	0.02	0.81	0.71	0.81	0.72	1.9	1.86	0.81	0.72
0.2	0.07	0.85	0.78	0.85	0.78	1.9	1.9	0.85	0.77
0.3	0.19	0.93	0.87	0.93	0.87	2	2	0.93	0.87
0.5	0.48	1.19	1.18	1.23	1.18	2.2	2.2	1.17	1.16
0.9	1.3	2.23	2.31	2.34	2.4	3.13	3.1	2.24	2.29

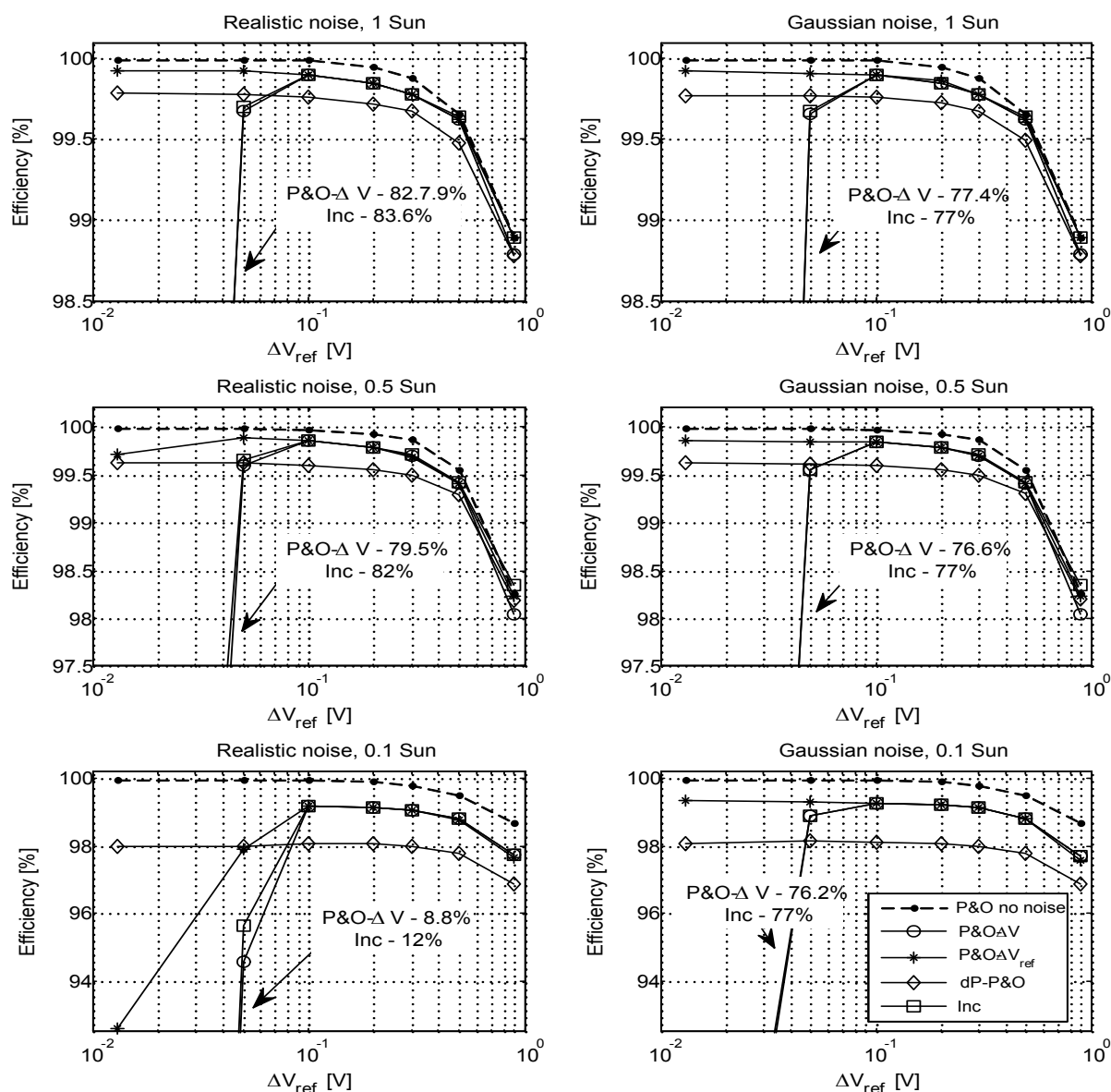


Figure 4.8 Efficiency of the algorithms with various step-sizes at different irradiation levels.

When no noise is present and under steady-state conditions, the P&O algorithm perturbs between three operating points around the MPP as shown in Figure 4.9 (a). This behaviour was achieved by the P&O- ΔV_{ref} algorithm at 1 Sun irradiation when realistic noise is present by enlarging the size of ΔV_{ref} to 0.9 V. When using a smaller step-size, such as $\Delta V_{ref} = 0.1$ V, the algorithm exhibited chaotic behaviour (Figure 4.9 (b)) but, somewhat surprisingly, achieved higher efficiency. It can be seen that for smaller step-size, the overall PV array voltage variations are smaller than for the larger step-size even though decisions at

many iterations were incorrect because of the presence of noise.

The P&O- ΔV and Inc algorithms suffer from a significant decrease in efficiency at small step-sizes. This is due to drift of the average PV panel voltage from the MPP to a higher voltage. For example, at irradiation of 1 Sun and a step-size of 13 mV, the average voltage of the P&O- ΔV algorithm was 19 V while the true MPP voltage was 17.01 V. The P&O- ΔV_{ref} and dP-P&O algorithms do not suffer from this phenomenon.

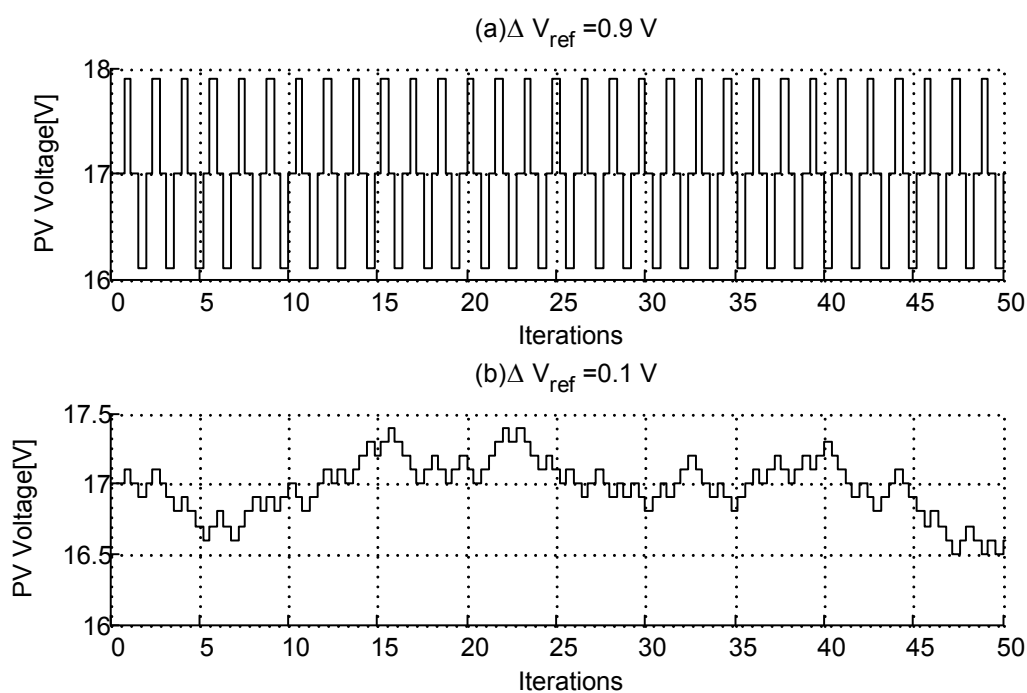


Figure 4.9 PV Voltage using as a result of operation of P&O- ΔV_{ref} algorithm (realistic noise) at irradiation of 1 Sun.

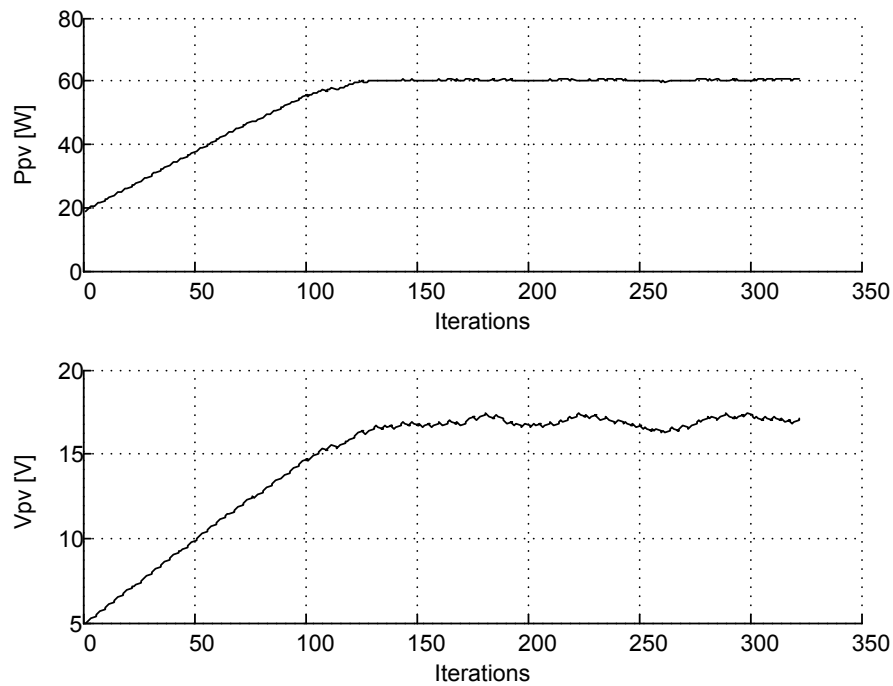


Figure 4.10 Convergence process of P&O- ΔV_{ref} algorithm with step size 0.1 V at irradiation of 1 Sun.

It can be seen that the dP-P&O algorithm had lower efficiency than the P&O- ΔV_{ref} algorithm during steady-state in the simulations, but dP-P&O is known to have better tracking performance during irradiation changes.

Figure 4.10 shows the convergence process of P&O- ΔV_{ref} algorithm with step-size 0.1 V at irradiation of 1 Sun starting from PV voltage of 5 V. This simulation shows that when operating at voltages away from MPP the MPPT algorithm is less affected by noise.

4.5 Results Verification

In order to verify the simulation results experimental tests were conducted. Figure 4.11 shows the convergence process from an initial low operating voltage to steady-state operation under the P&O- ΔV algorithm. The graphs show the PV module voltage and efficiency (calculated as $100\% \cdot P_{MPP}/P$). It can be seen that maximum efficiency was achieved at time of 10 s and at the voltage of 14.3 V. However, the voltage continued to increase and reached steady-state of about 15 V with the efficiency decreased to average below 99%.

Figure 4.12 shows results of a similar experiment for the P&O- ΔV_{ref} algorithm. It can be seen that the maximum efficiency was achieved at a time about 10 s at a voltage of 14.6 V. The algorithm continued to operate with an average voltage close to the MPP voltage and at average efficiency above 99%. These tests were conducted at different conditions from the simulations but the same behaviour can be seen in that the P&O- ΔV_{ref} algorithm is not systematically displaced from the MPP as is the P&O- ΔV algorithm.

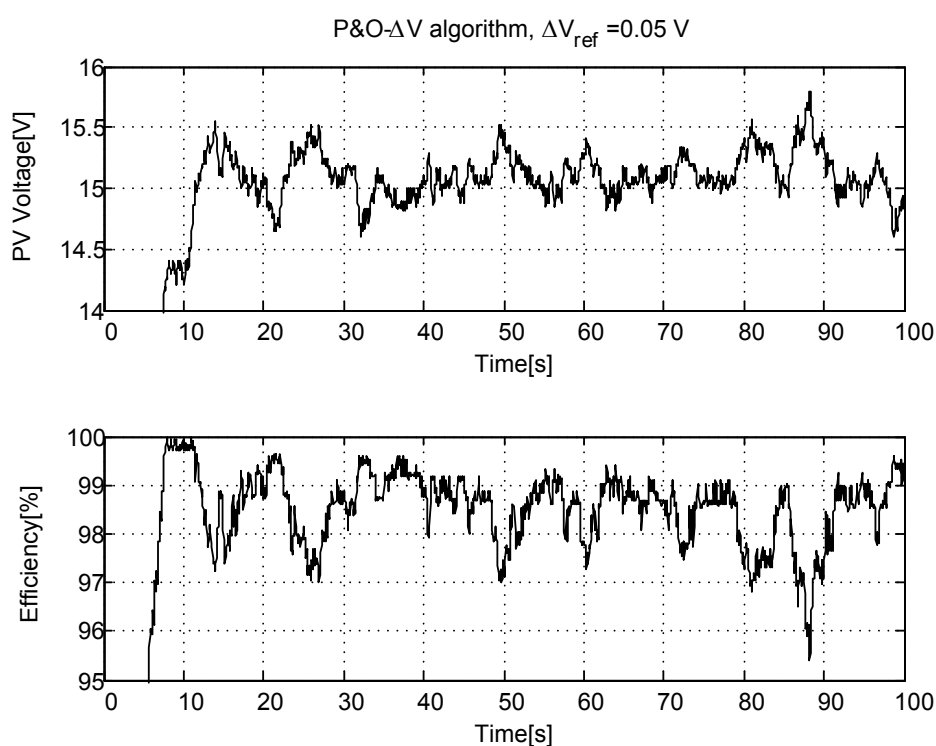


Figure 4.11 Experimental results of P&O- ΔV algorithm operation with step-size of 0.05 V.

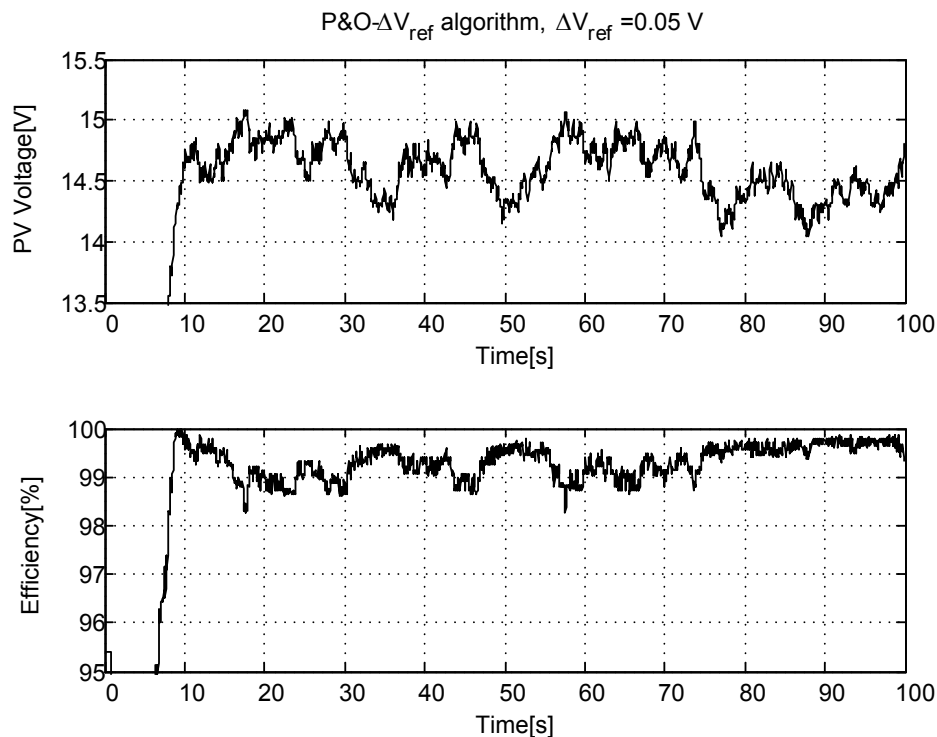


Figure 4.12 Experimental results of P&O- ΔV_{ref} algorithm operation with step-size of 0.05 V.

In addition, the results for P&O- ΔV algorithm can be verified against the experimental results in [36]. The results for Gaussian noise for the P&O- ΔV_{ref} algorithm can be verified against simulation results in [37]. Noise characteristics may be different for each particular implementation of an MPPT but common types of behaviour of the MPPT algorithms in presence of noise can be determined.

4.6 Discussion

Simulations produced with Gaussian noise provided very similar results to simulations with realistic noise for larger step sizes and higher irradiation levels. This verifies the validity of models based on Gaussian noise [36],[37] for these conditions, however differences in efficiencies were observed in simulation with a very small step size. For the dP-P&O and P&O- ΔV_{ref} algorithms, the results for Gaussian and realistic noise were similar for a wider range of conditions than they were for the P&O- ΔV and Inc algorithms. This indicates that

the acceptability of using a Gaussian noise model approximation depends on the type of MPPT algorithm being examined. In contrast to the results reported in [[37], the realistic noise simulations show that, at small step sizes, the efficiency decreases with a decrease of step size. This decrease of the efficiency is more significant at lower irradiations. That means that there is an optimum step size for maximizing steady-state efficiency of P&O- ΔV_{ref} and dP-P&O even if dynamic performance is not taken into account.

All the algorithms tested performed better at higher irradiation levels. Since the absolute values of the derivative dP/dV in vicinity of the MPP are larger at higher irradiation, the differences in power being measured by the MPPT algorithms are relatively large compared to the noise and the correct decisions will be made. This also indicates that MPPT will have better performance when applied to PV arrays with higher fill factor as they have larger dP/dV . Also, the absolute value of dP/dV is larger at voltages away from the MPP which helps the algorithms have good dynamic performance during transients even if the step size is chosen for better steady-state efficiency. It can be seen in Figure 4.10 that the algorithm operation is not affected by noise until the PV voltage is close to the MPP.

P&O- ΔV and Inc algorithms suffer from low efficiency when the step size ΔV_{ref} is close to or smaller than the voltage noise level due to operation at a higher average PV voltage than the MPP voltage. This can be explained by writing expansions for the terms ΔP and ΔV including the voltage noise (X_{mes} , X_{act} and X_{noise} represent the measured, actual and noise signals respectively) as:

$$\begin{aligned}\Delta P_{mes} &= V_{mes} I - V_{mes}(prev) I(prev) \\ &= (V_{act} + V_{noise}) I - (V_{act}(prev) + V_{noise}(prev)) I(prev) \\ &= \Delta P_{act} + I V_{noise} - I(prev) V_{noise}(prev).\end{aligned}\tag{4.1}$$

Using the approximation $I \approx I(prev)$ and similar development of ΔV gives:

$$\begin{aligned}\Delta P_{mes} &\approx \Delta P_{act} + I(V_{noise} - V_{noise}(prev)) \\ \Delta V_{mes} &= \Delta V_{act} + (V_{noise} - V_{noise}(prev)).\end{aligned}\tag{4.2}$$

When operating at a voltage higher than the V_{MPP} , ΔP_{act} and ΔV_{act} have opposite signs, but voltage noise has an effect of adding values with the same sign (positive or negative) to the ΔP_{act} and ΔV_{act} . This leads to an increase in the chance that ΔP_{mes} and ΔV_{mes} seen by the algorithm will have the same sign and the operating point will be moved to a higher voltage until ΔP_{act} is large enough to stop the drift of the average operating point. This phenomena is also explained in [[36]]. Thus it is recommended always to use the P&O- ΔV_{ref} algorithm which is not affected by this phenomena rather than the P&O- ΔV algorithm. When using the Inc algorithm one needs to make sure that the step size ΔV_{ref} is sufficiently larger than the voltage measurement noise.

The dP-P&O algorithm is known to have better performance than the P&O algorithm during changing irradiation conditions. But as is demonstrated here, the dP-P&O algorithm is more sensitive to noise as it is based on the difference between two small values that include noise and the dP-P&O algorithm has lower efficiency at steady state operation. In general, the modifications made to the algorithms to improve different aspects of their operation such as improved transient irradiation tracking may cause degradation of performance in the presence of noise.

4.7 Conclusions

Operation of four MPPT algorithms in the presence of measured noise were tested using a simulation technique in which signals are recorded before artificial noise is added. This simulation method can be readily applied to various MPPT algorithms. The artificial noise was based on experimental measurements and included Gaussian, switching and quantization components. Comparison with an equivalent Gaussian noise model in simulation showed that models based on only Gaussian noise can accurately represent the operation of MPPT systems in the presence of real noise at larger step sizes and high irradiation levels.

Differences become apparent between the P&O- ΔV [16]-[18] and P&O- ΔV_{ref} [19]-[21] algorithms. It was shown that the P&O- ΔV_{ref} algorithm has better performance than the P&O- ΔV algorithm in the presence noise. It was also shown that better steady-state efficiency of the P&O algorithm can be achieved using smaller step sizes when the algorithm operates mostly randomly; this does not necessarily lead to wrong steps being taken due to noise and the tracking speed reduction when operating far away from the MPP. It was also shown that some modifications of the P&O algorithm that are intend to improve different aspects of its performance like the dP-P&O algorithm can reduce the steady-state efficiency.

Chapter 5

Interpolation MPPT algorithm

5.1 Introduction

In order to derive representative model of the PV system, the MPPT should be included in the model. However, commonly used effective MPPT methods such as Perturb and Observe (P&O) have the nature of a search algorithm rather than control system and cannot be easily integrated in the state-space models of the overall system. In this work, the approach to cope with this problem is to develop an MPPT method in which the MPP search algorithm will be active for infrequent short periods of time and during most of the time the system will be operated by a linear controller.

The linear controller operation can be achieved using emulated load controller [41] introduced in Chapter 2 and modelled in Chapter 3. This controller can hold constant operating point when environmental conditions are stable and keep the operating point close to the MPP during changes in irradiation of about ± 0.2 Sun. With significant change of irradiation and change of the PV cells temperature the reference voltage of the emulated load controller V_{ref} needs to be readjusted by the MPPT algorithm.

In order to be active for short period of time, the MPP search algorithm should be able to find the maximum point using a small number of measurement points of the PV characteristic and to do so accurately for measurement points at some significant distance from the MPP. The need for a small number of measurements arises from the settling time requirement imposed by that converter's dynamic allow [53]. It would seem that polynomial interpolation of measurement points and an estimation of the MPP from these could be used. Actually, the P&O method can be seen as a first order interpolation that provides the

direction of power increase whereas a second order polynomial interpolation could provide the location of MPP directly. Figure 5.1 shows the PV characteristic sampled at three points (V_l , V_c and V_r), a parabola through those points and maximum of the parabola and the real MPP of PV characteristic. In this problem we require that calculated maximum of the parabola is sufficiently close to the real MPP.

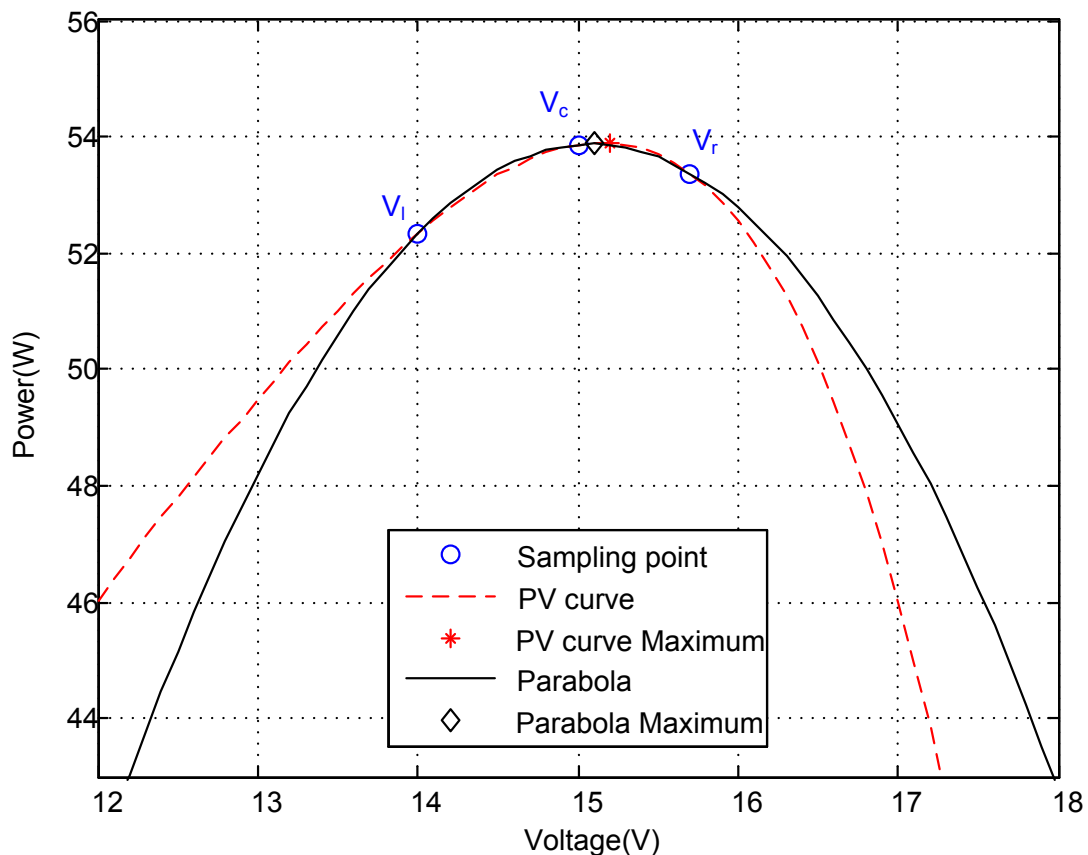


Figure 5.1 PV characteristic sampled at three points, calculated parabola and maximum points.

Several MPPT algorithms have been developed recently based on the principle of second order interpolation [59]-[62]. In [59], measurement of open circuit voltage is used for calculating the starting point for second order interpolation. Measurement of open circuit voltage requires additional hardware and causes loss of power output during the measurement. The methods in [60] and [61] are based on convergence by reducing the distance between sample points until the result of last set of sample points is close enough to

the result of previous set of measurements with larger distance between the sample points. This convergence process can take a long time during which some power is lost. In [62] the convergence process includes use of the P&O algorithm, which brings the operating point close to the MPP, before the interpolation occurs. There is no convergence process for the interpolation used in [62], i.e. the first value for the MPP is used, but no assessment of the error or the result of the interpolation calculations was done. These methods [59]-[62] provide alternative means to locate the MPP but do not address the question how frequently the interpolation process should be activated and how well the algorithms operate under changing irradiation. Because the sampled points used in interpolation methods are relatively far from each other, and far from the MPP, a lot of power is foregone if the sampling is repeated often. On the other hand, continuing to operate at an out-of-date operating point after the PV characteristic has changed also leads to power being lost.

An intended contribution of this work is in choosing the distance between sampling points to minimise the error in calculation of the MPP. The optimization is based on offline analysis that also helps to determine a range of voltage within which the result has a low error and can be considered as a valid MPP. It is intended that this check of validity can be made alongside the calculation of the MPP and if the indication is that the error is low then the result can be applied directly without additional iteration. If the result is not within the required accuracy range then an additional point can be measured to the left or right of the sample current points and the MPP calculated again. Once the MPP has been established, the algorithm is suspended until there is an indication that the irradiance may have changed. By combining this method with the emulated load controller, small changes in irradiance can be accommodated with reasonable accuracy without re-invoking the search for the MPP. In order to achieve efficient operation of the algorithm, the measurements of the sampling points need to be done during periods of time when the irradiation level is constant. This would not

be suitable for constantly fluctuating irradiation profile; however, the realistic irradiance profiles normally have sufficient periods of time of constant irradiation levels to allow taking the measurements and readjusting the operating point.

5.2 Theoretical background of polynomial interpolation

This section summarises some background material about polynomial interpolation and draws on material presented in “Numerical Analysis” by Burden and Faires [63].

If a function $f(x)$ is sampled at $n+1$ points with values x_i then a polynomial

$$p(x) = a_n x^n + a_{n-1} x^{n-1} + \dots + a_2 x^2 + a_1 x + a_0 \quad (5.1)$$

of n^{th} order can be found so that at the sampling points the values of the polynomial and the given function will be equal

$$p(x_i) = f(x_i), \text{ for all } i \in \{0, 1, \dots, n\} \quad (5.2)$$

The polynomial coefficients a_i can be found by solving the equation:

$$\begin{bmatrix} x_0^n & x_0^{n-1} & x_0^{n-2} & \dots & x_0 & 1 \\ x_1^n & x_1^{n-1} & x_1^{n-2} & \dots & x_1 & 1 \\ \vdots & \vdots & \vdots & & \vdots & \vdots \\ x_n^n & x_n^{n-1} & x_n^{n-2} & \dots & x_n & 1 \end{bmatrix} \begin{bmatrix} a_n \\ a_{n-1} \\ \vdots \\ a_0 \end{bmatrix} = \begin{bmatrix} f(x_0) \\ f(x_1) \\ \vdots \\ f(x_n) \end{bmatrix} \quad (5.3)$$

The interpolation error is given by:

$$f(x) - p_n(x) = \frac{f^{(n+1)}(\xi)}{(n+1)!} \prod_{i=0}^n (x - x_i), \text{ where } \xi \in [x_0, x_n] \text{ is unknown.} \quad (5.4)$$

The absolute maximal error is given by substituting in the maximum values for each term:

$$|f(x) - p_n(x)| \leq \max_{\xi \in [x_0, x_n]} |f^{(n+1)}(\xi)| \frac{1}{(n+1)!} \left| \prod_{i=0}^n (x - x_i) \right| \quad (5.5)$$

The error equation can be seen as product of three terms:

The term $\frac{1}{(n+1)!}$ depends on the interpolation order.

The term $f^{(n+1)}(\xi)$ depends on the sampled function.

The term $\prod_{i=0}^n (x - x_i)$ depends on sampling points.

This final term, $\prod_{i=0}^n (x-x_i)$, can be minimised by sampling at Chebyshev points. In case of second-order interpolation, the Chebyshev points will be simply equi-distant points (i.e., $x_2-x_1 = x_1-x_0$). Figure 5.2 shows the function $\prod_{i=0}^2 (x-x_i)$ for the second order case with equi-distant points and three different distances. It can be seen that the closer the points one to another, the lower the interpolation error.

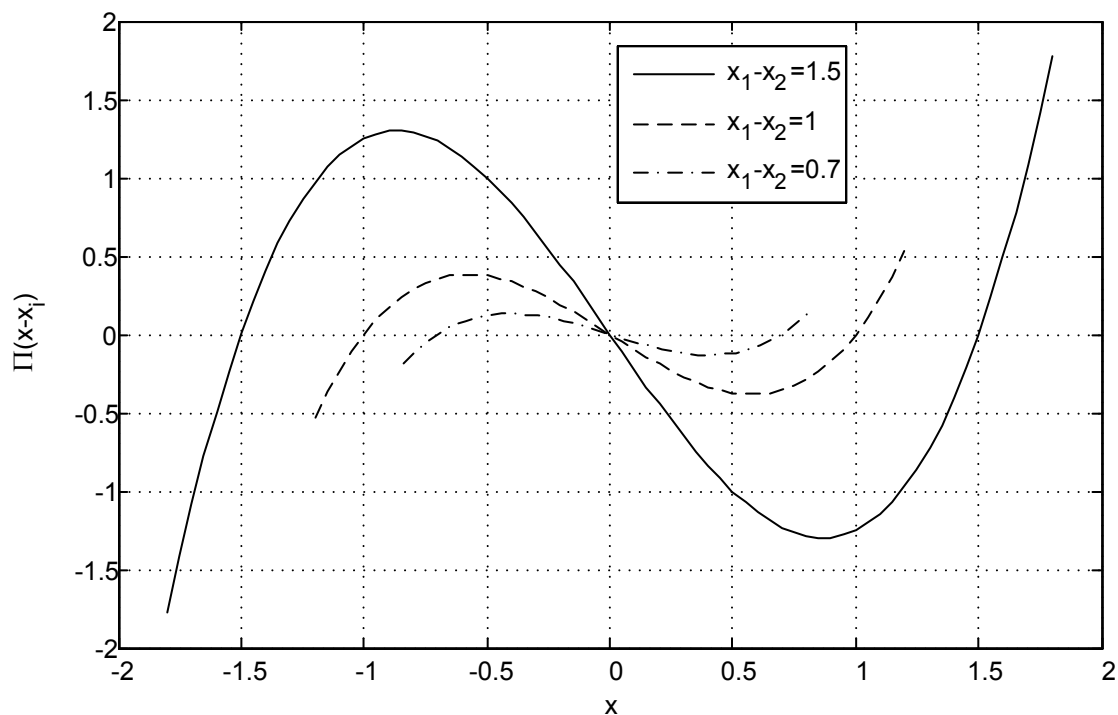


Figure 5.2 The function $(x-x_0)(x-x_1)(x-x_2)$, $x_1=0$.

5.3 Assessment of interpolation of PV power curves

In the case of second-order interpolation, the term $f^{(n+1)}(\xi)$ in the interpolation error equation is third derivative of the sampled function. Figure 5.3 shows the PV power-voltage characteristic and its third derivative at three irradiation levels. Even though the absolute maximum of the third derivative does not vary much with irradiation it can be seen that at voltages close to the MPP (at 14-16.5 V) the absolute values of the derivative are higher for

higher irradiation levels. This suggests that the interpolation error will be larger for higher irradiances if all three sample-points are close to the MPP.

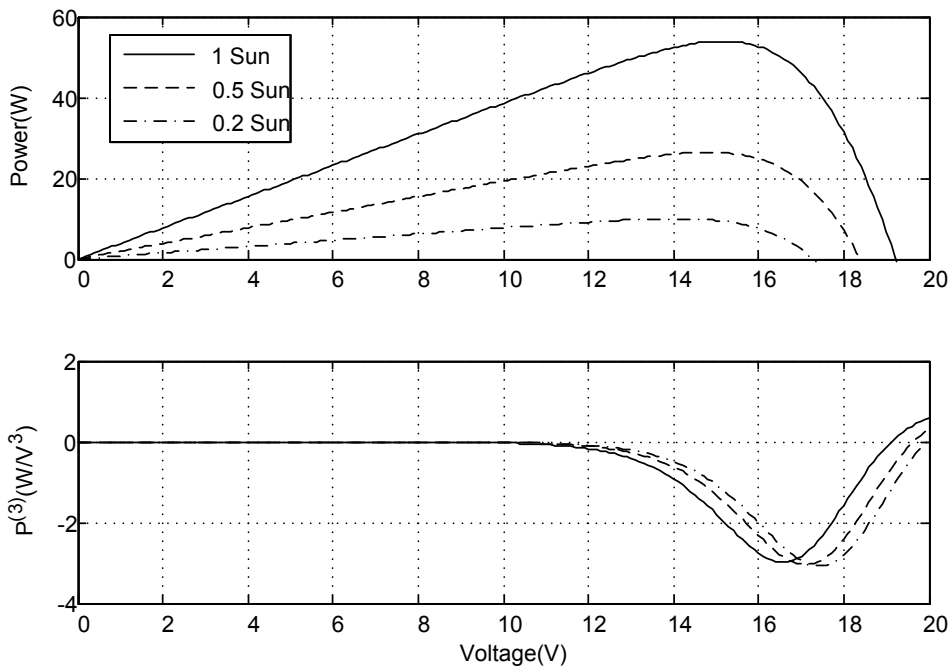


Figure 5.3 Power – voltage characteristic of PV panel and its third derivative.

When the emulated load controller is used, it is more natural to perform the interpolation on PV power as a function of the reference voltage V_{ref} so that the outcome of the search for the MPP is expressed in terms of the V_{ref} to be passed to the controller without the need of further calculation. Figure 5.4 shows the PV power versus V_{ref} characteristic and its third derivative at an irradiation of 1 Sun when an emulated load controller with a gain of $r=0.8$ is used. It can be seen from Figure 5.4 that the absolute maximum value of the derivative is reduced in comparison to PV power versus PV voltage graph in Figure 5.3. This shows that careful choice of the function to interpolate can improve the interpolation error. However, it should be noted that the gain r of the emulated load controller is chosen in order to match the emulated load characteristic to the MPP locus (in order to properly track small changes in irradiance) and not with reference to improving the interpolation error. In some cases, even a negative value of r is required [64] and this can increase the interpolation error.

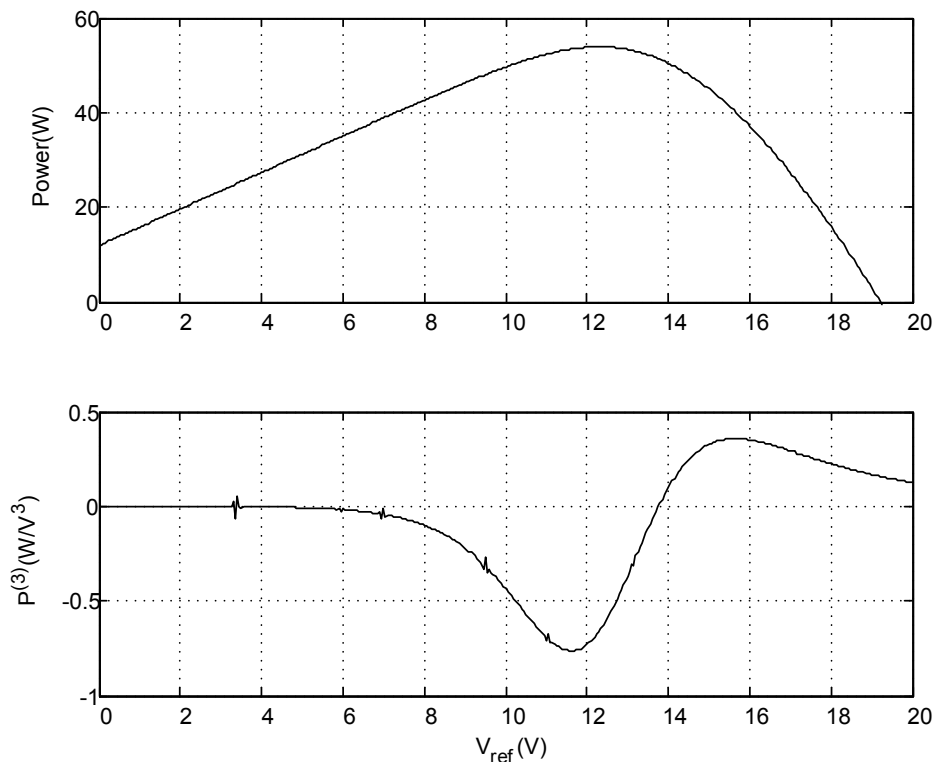


Figure 5.4 Power – V_{ref} characteristic of PV panel and its third derivative at irradiation of 1 Sun.

It was realised that if the natural choice of independent and dependant variables for the interpolation function does not provide sufficiently low error it is possible to reduce the error by rotation of the axis. Figure 5.5 shows power versus voltage characteristics with the axis rotated by 3° . It can be seen that absolute maximal value of the third derivative is reduced in comparison to the value in Figure 5.3.

The axis transformations will also influence the sampling points term $\prod_{i=0}^n (x - x_i)$ of the error equitation, but this change is not significant and may even reduce this term's contribution to the error.

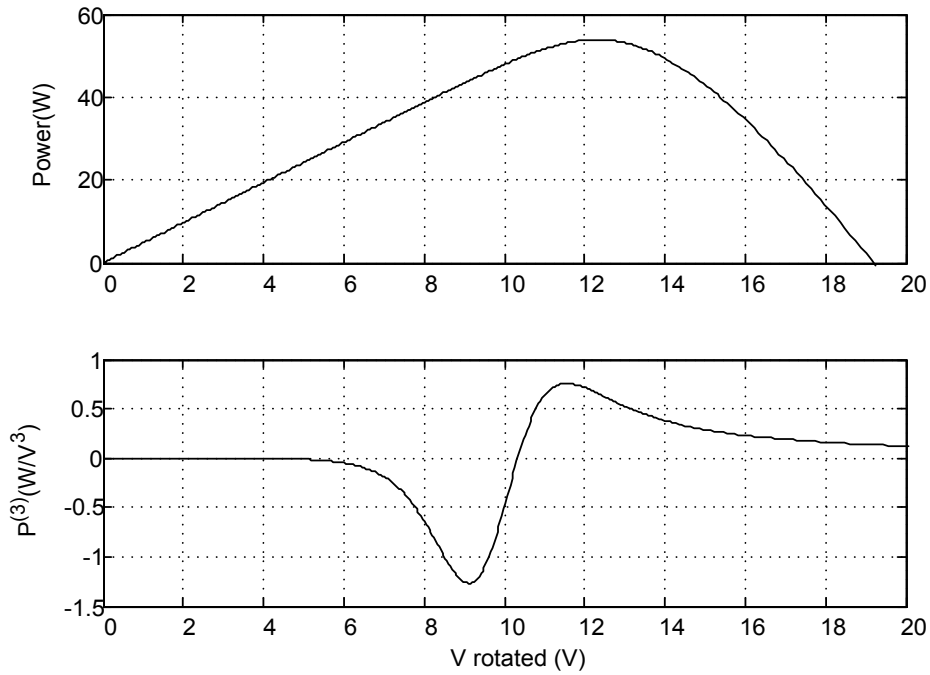


Figure 5.5 Power – voltage characteristic of PV panel and its third derivative at irradiation of 1 Sun in axis system rotated by 3°.

The preceding analysis helps to estimate how close the approximated by parabola power-voltage PV characteristic to the real characteristic, however, for MPPT application, it is the location of the MPP that is important i.e. how close the MPP calculated from the parabola is to the real MPP and how much power is lost due to operation at the calculated MPP. The estimated location of the MPP is calculated by finding the stationary point on the parabola

$$x_{est_max} = -\frac{a_1}{2a_2} \quad (5.6)$$

and the estimated maximal power can be calculated by

$$P_{est_max} = a_0 + \frac{a_1 x_{est_max}}{2} \quad (5.7)$$

It is possible to calculate the maximum location directly, without calculating the polynomial coefficients a_0, a_1, a_2 . The direct calculations from sampling points and development of maximum estimation calculations for rotated axis appear in Appendix A and Appendix B

respectively. In those appendices an effort made to reduce the amount of calculations for microcontroller.

In order to evaluate the error in calculation of the estimated MPP, simulations of such calculations with various locations of the sampled points around the real MPP were conducted. Figure 5.6 shows simulation results of MPP location calculation from three points at equal distances of 1 V in the control variable V_{ref} axis with emulated control employed. The horizontal axis shows the location of the sampling points by providing the difference between the central sampling point V_c and the V_{refMPP} , the value of V_{ref} that provides the real MPP location calculated in advance. Three different arrangements of the sampling points are illustrated in Figure 5.7. Figure 5.7(a), (b) and (c) describe the sampling points positions that relates to the left, central and right parts of Figure 5.6 respectively. The top graph of Figure 5.6 shows the difference between the real maximal power P_{MPP} and $P_{op_est_MPP}$ the generated power when the PV panel operates at calculated estimation of MPP location $V_{ref_est_MPP}$. The second graph shows the difference between the real maximal power P_{MPP} and the estimated maximal power P_{est_MPP} calculated using (5.7). The bottom graph of Figure 5.6 shows the difference between the real MPP voltage V_{MPP} and $V_{op_est_MPP}$ the PV voltage when the PV panel operates at calculated estimation of MPP location $V_{ref_est_MPP}$.

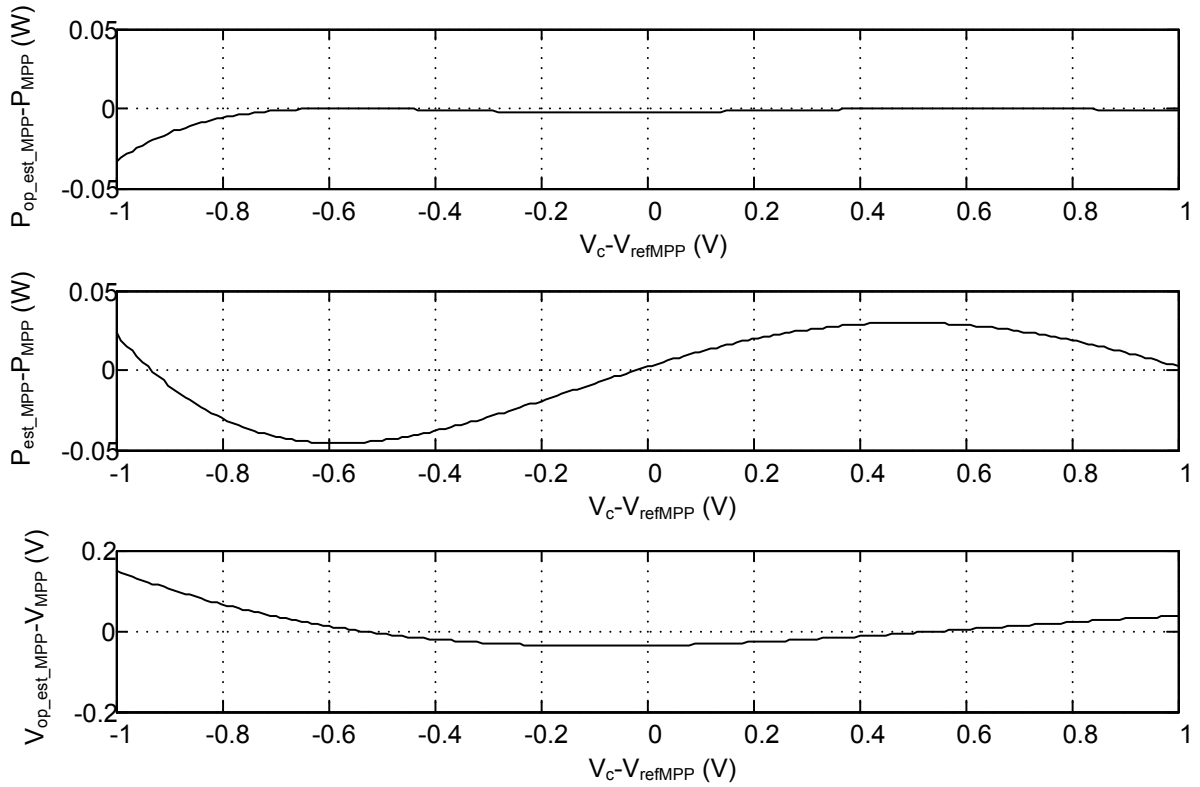
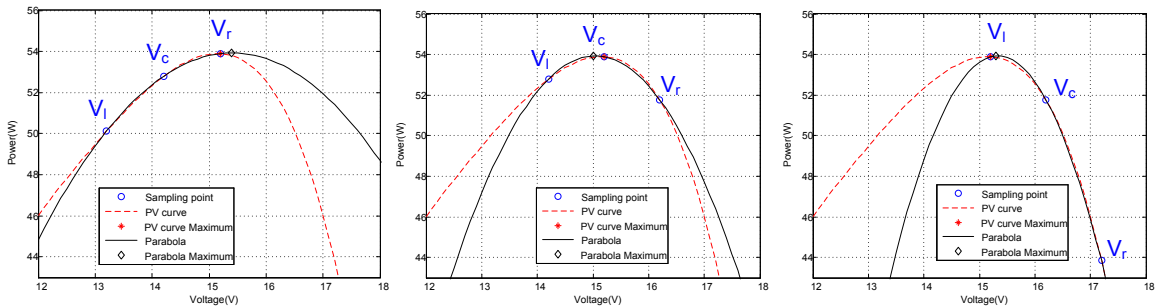


Figure 5.6 Simulation results of maximum calculation at different sampling points. Top to bottom: power loss, error of maximal power estimation, error of maximum location.



(a) $V_c - V_{refMPP} = -1 \text{ V}$ (b) $V_c - V_{refMPP} = 0 \text{ V}$ (c) $V_c - V_{refMPP} = 1 \text{ V}$

Figure 5.7 Different positions of the sampling points.

Figure 5.6 can help to identify how the expected error in the estimation of the MPP could be evaluated using only information available to the algorithm. It can be seen from the top and middle graphs of Figure 5.6 that the error in estimating the power at the MPP ($P_{est_MPP} - P_{MPP}$) is larger than the difference between the actual power obtained when the estimated reference voltage for the MPP is used and power at the true MPP ($P_{op_est_MPP} - P_{MPP}$). This shows that calculation of the estimated MPP power (P_{est_MPP}) cannot be used to

evaluate the error. But it is possible to identify that for some distances of the central sampled point (V_c) from the reference voltage at the MPP (V_{refMPP}) the power loss is lower than for other distances. Since the V_{refMPP} is unknown in real-time, the error evaluation will need to be done on the basis of distance of the V_c from $V_{ref_est_MPP}$. It is possible to find an interval in vicinity of V_c such that if the calculated maximum is within that interval V_c then the error is low.

It can be seen from the bottom graph of Figure 5.6 that when V_{refMPP} is far from V_c , the operating voltage at the estimated MPP ($V_{op_est_MPP}$) is higher than the voltage of actual MPP (V_{MPP}) and hence $V_{ref_est_MPP}$ is higher than V_{refMPP} . In addition, it can be seen that a larger error occurs when V_{refMPP} is higher than V_c , i.e. the error is large when $V_{ref_est_MPP} > V_{refMPP} > V_c$. This observation can be used to set a minimum limit for the term $V_c - V_{ref_est_MPP}$ since $V_c - V_{ref_est_MPP} < V_c - V_{refMPP}$. This means that if $V_c - V_{ref_est_MPP}$ is greater than a preset value then $V_c - V_{refMPP}$ is also greater than a predetermined value and the result can be considered to have low error.

Setting the maximal value for $V_c - V_{ref_est_MPP}$ cannot guarantee maximal value for $V_c - V_{refMPP}$ but this is not problematic as the error is much lower at higher $V_c - V_{refMPP}$ and $V_c - V_{refMPP}$ cannot be much higher than $V_c - V_{ref_est_MPP}$. To summarise, if the value of the term $V_c - V_{ref_est_MPP}$ is within a predetermined “low error” interval then the error can be expected to be considered low. This mechanism can be used in the algorithm to decide whether the estimated MPP should be trusted as having a low error and applied immediately or whether additional measurements should be taken to obtain a better estimate. If additional measurements are needed but one wishes to use only one further measurement (and retain two from the previous set) then the length of the low error interval should be equal or larger than distance between the sampled points in order to ensure that MPP can be found from at least one set of sampling points.

5.4 Interpolation of PV power curves in presence of noise

As discussed in Chapter 4, noise is always going to be present in measured voltage and current signals in a PV system and it is important to examine the error in the proposed interpolation method caused by measurement noise. Simulations similar to those in previous section (which produced the results in Figure 5.6) were performed again but with noise added to the measured signals. Gaussian noise with standard deviations of 27 mV and 7.5 mA were added to the PV voltage and current respectively, as was the case in Chapter 4. A simplified Gaussian noise model can be used here because the step-size in the interpolation method is relatively large. In Chapter 4 it was shown that for large step-sizes the Gaussian noise model provides accurate results. Simulation for each set of interpolation points was repeated 10,000 times. Figure 5.8 and Figure 5.9 show mean values of power foregone ($P_{MPP} - P_{op_est_MPP}$) plotted against the location of the sampling points (provided as the difference between the central sampling point V_c and the $V_{ref(MPP)}$) for four different choices of the distance between the sampling points (known here as the sampling interval). Figure 5.8 applies for calculations in power-voltage plane and Figure 5.9 for calculations in power- V_{ref} plane. Appendix C contains further detailed plots including maximal error on both linear and logarithmic scales.

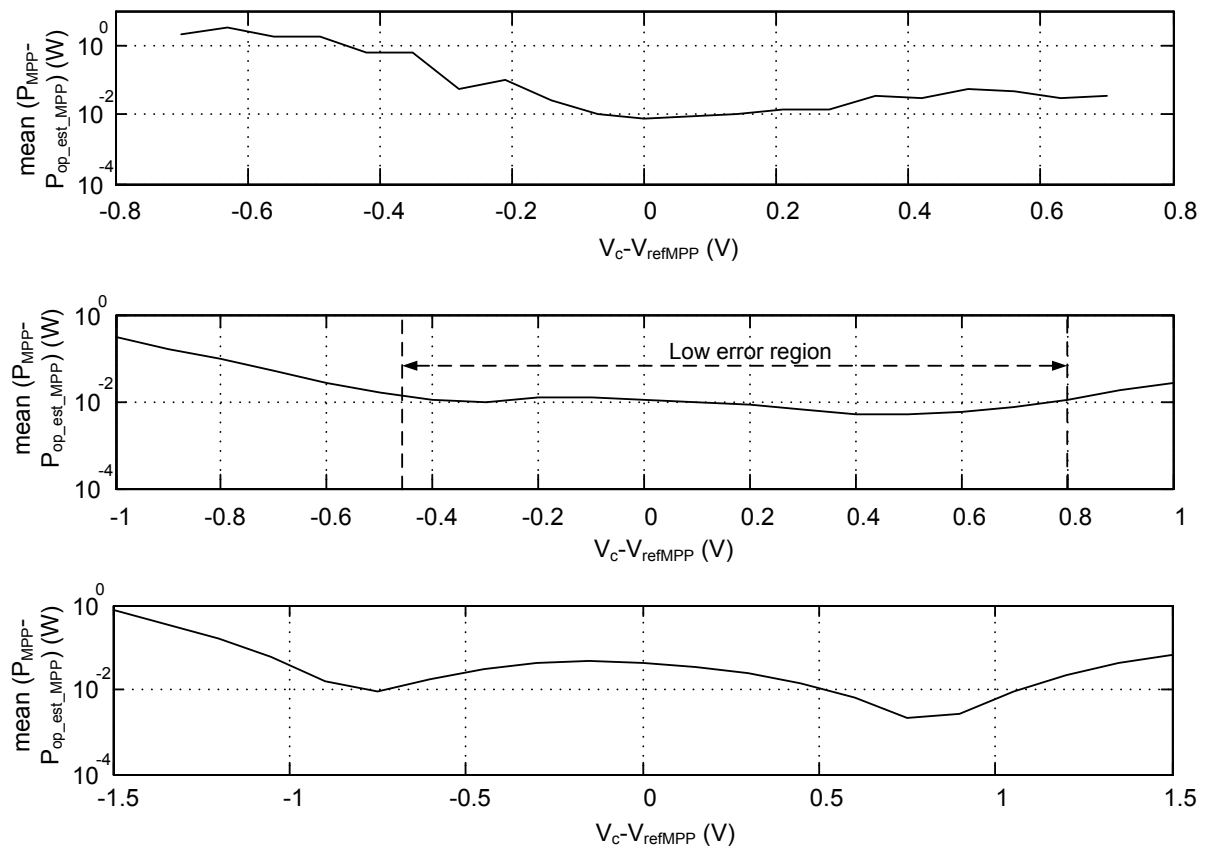


Figure 5.8 Simulation results of mean power loss in maximum calculation in V-P plane at different sampling points in presence of noise. Distance between sampling points, top to bottom: 0.7 V, 1 V, 1.5 V.

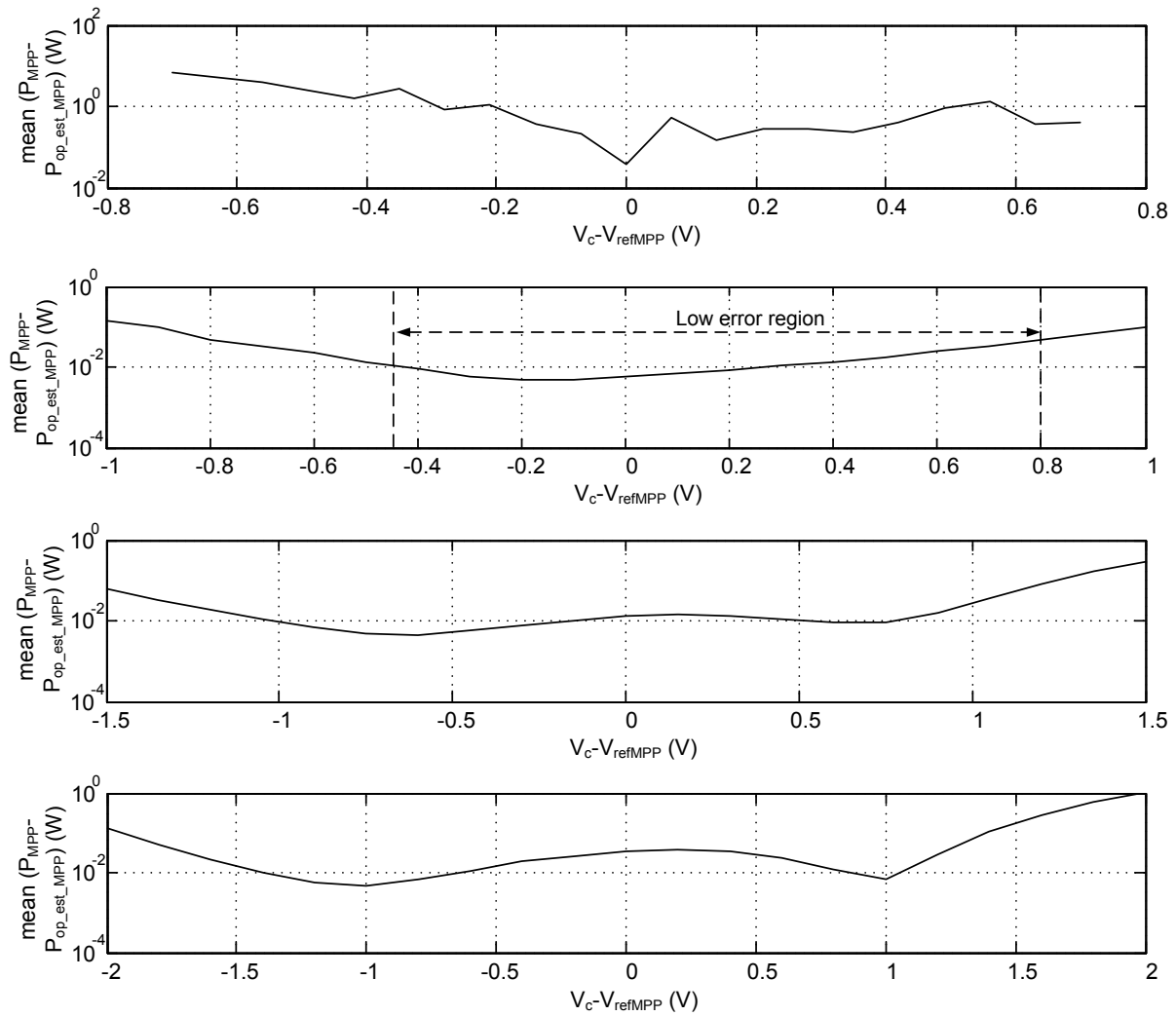


Figure 5.9 Simulation results of mean power loss in maximum calculation in V_{ref} -P plane at different sampling points in presence of noise. Distance between sampling points, top to bottom: 0.7 V, 1 V, 1.5 V, 2 V.

In order to achieve reliable operation of the MPPT algorithm, it is important that the error in the calculation of the location of the MPP is low over large part (at least 50%) of the sampling interval. The analysis in previous section (where noise was not included) suggested that the interpolation error decreases with a narrowing of the sampling interval, however, Figure 5.8 and Figure 5.9 show that there is an optimal sampling interval for minimal error. In Figure 5.8, the error for an interval of 1 V is lower than the error for intervals of 0.7 V and 1.5 V. In Figure 5.9, the error for an interval of 1 V and 1.5 V is lower than the error for intervals of 0.7 V and 2 V. Thus, it is proposed that the developed MPPT algorithm should

use an optimally chosen sampling interval and the sampling points will be moved to cover different parts of the PV characteristic. This is different from the approach in [60],[61] in which the sampling interval was adjusted. Basing on the simulation results presented here, the distance between sampled points was chosen to be 1 V (for the conditions tested) since it provides sufficiently low error when using either the power-voltage and power- V_{ref} planes. It was decided that the region $-0.45 \text{ V} < V_c - V_{ref_est_MPP} < 0.8 \text{ V}$ could be considered to be of low error. This region covers 62.5% of the sampling interval of 2 V and provides sufficient overlap between two sets of subsequent measurements that share two out of three sampling points.

5.5 Algorithm development

The intention of developing the interpolation-based algorithm was to find the MPP accurately and quickly using only a small number of measurement points of the PV characteristic. After the MPP is located, the algorithm will suspend its active operation and will only monitor the operating point in order to detect changes in irradiation or temperature that require the algorithm to activate again.

A flowchart of the algorithm is shown in Figure 5.10. After setting the initial operating point, the algorithm waits for stable conditions in order to start the sampling of the three interpolation points. Waiting for a stable condition helps to ensure that the three sampled points are measured at the same irradiation level and temperature, i.e., the three points can be considered to belong to the same P-V characteristic. The initial operating point is taken as the central sample point of the three and two additional points to left and right are then measured. This order was chosen so that in continuous operation the central point will be close to the MPP. After the algorithm has measured the three points, it measures the central point again to ensure that there was no change in environmental conditions during the sampling process. If a change is detected then those measurements will be discarded and the algorithm will wait for

a stable condition before taking a fresh set of samples. When satisfactory samples have been obtained, the location of the MPP is calculated using the interpolation method. If the calculated MPP lies in the range which is considered to be the low-error range (defined above) then that MPP location is accepted as the new operating point. Operation at this point continues until a change in environmental conditions is detected or until some preset maximum period is reached. If the calculated MPP lies outside the low-error range, an additional point to the right or left of the existing points is measured and used together with two of the previously measured points to form a new estimation of the MPP.

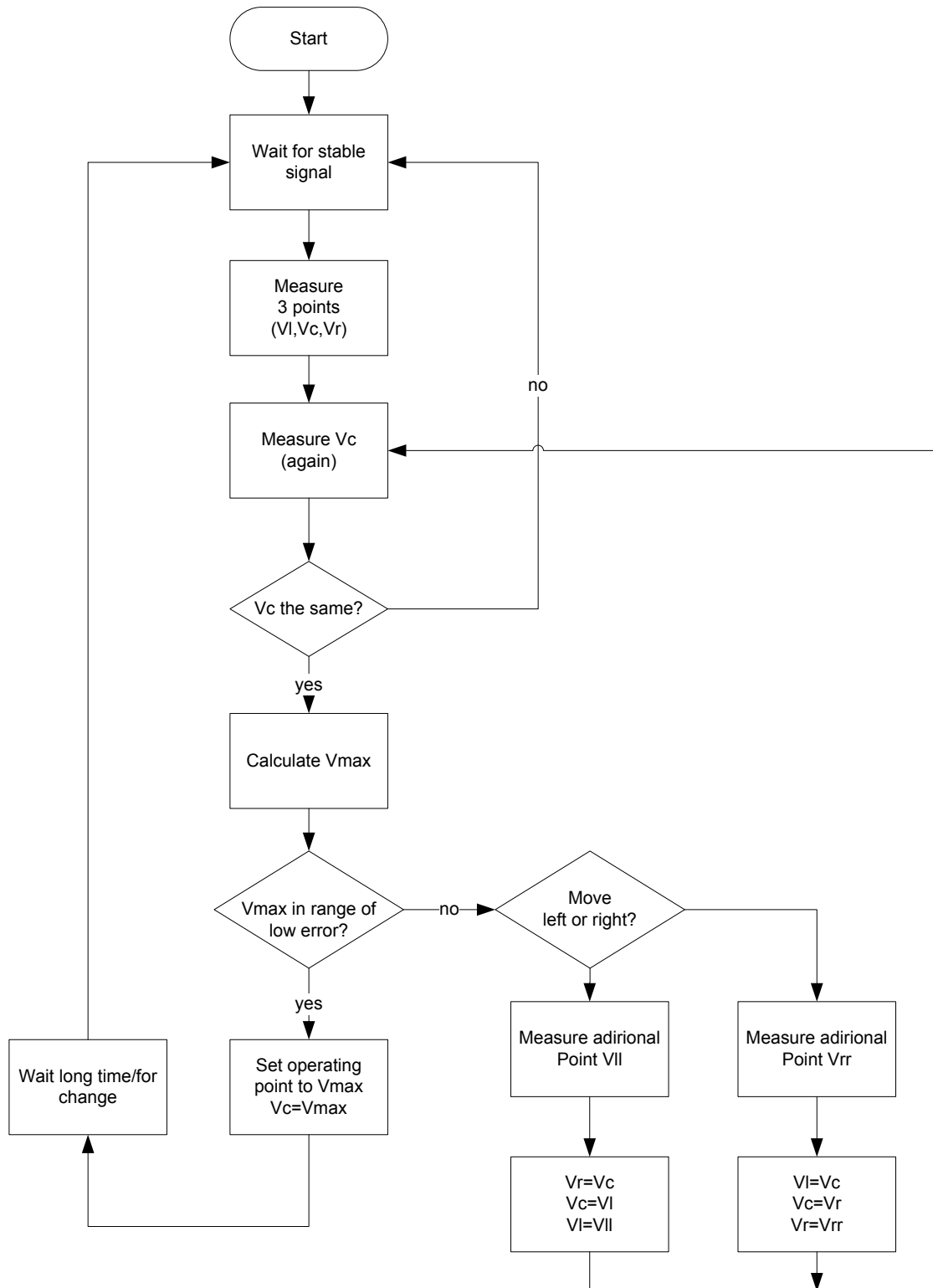


Figure 5.10 Flowchart of the interpolation MPPT algorithm.

5.6 *Simulation and experimental tests*

5.6.1 **Simulation results**

Simulation results of the interpolation-based MPPT algorithm (including noise effects) are now examined and compared to results for the P&O- ΔV_{ref} algorithm. In these simulations, the minimum time interval between the iterations is set to 30 ms for the interpolation method and 20 ms for the P&O- ΔV_{ref} algorithm.

Figure 5.11 shows steady-state operation of the two algorithms at an irradiation of 1 Sun. It can be seen that, unlike the P&O- ΔV_{ref} algorithm, the interpolation algorithm does not perform perturbations after the initial calculation (using three measured points). The measured efficiency of the interpolation algorithm was 99.97% versus 99.85% for the P&O- ΔV_{ref} algorithm. Figure 5.12 shows similar results for an irradiation of 0.3 Sun for which the algorithm efficiencies are 99.68% and 99.66% respectively.

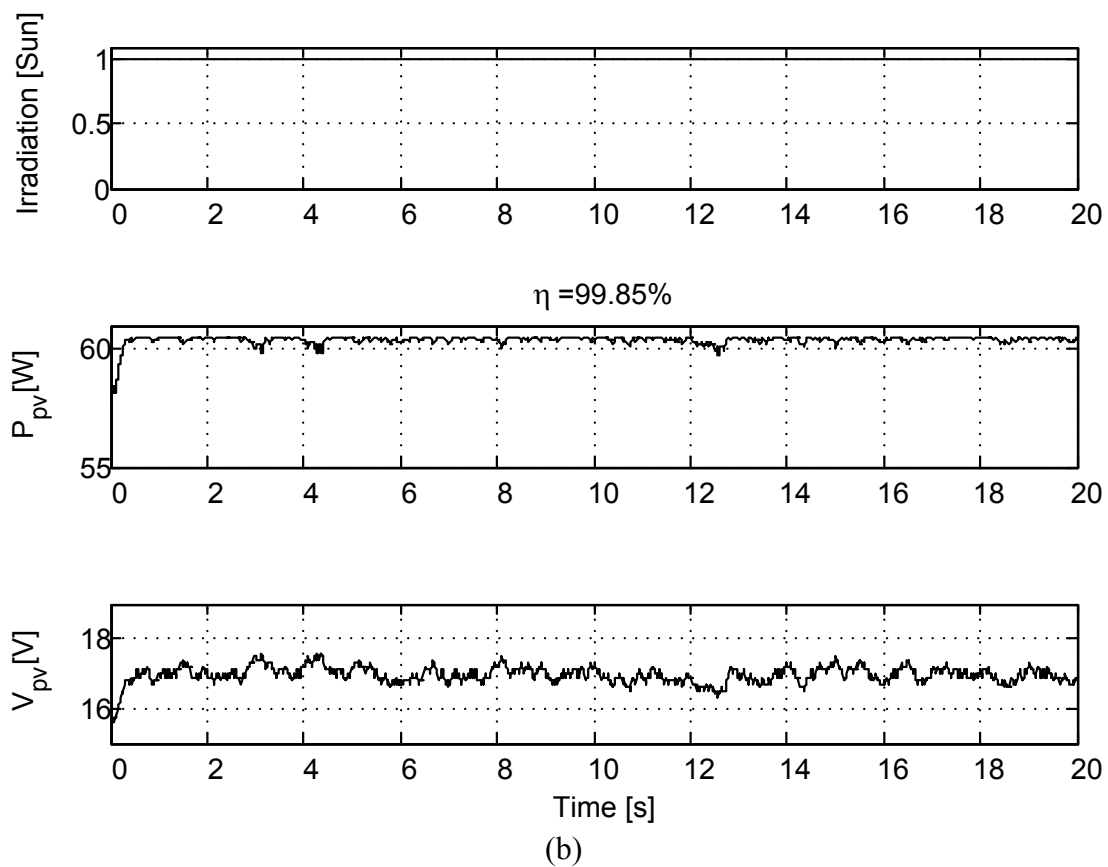
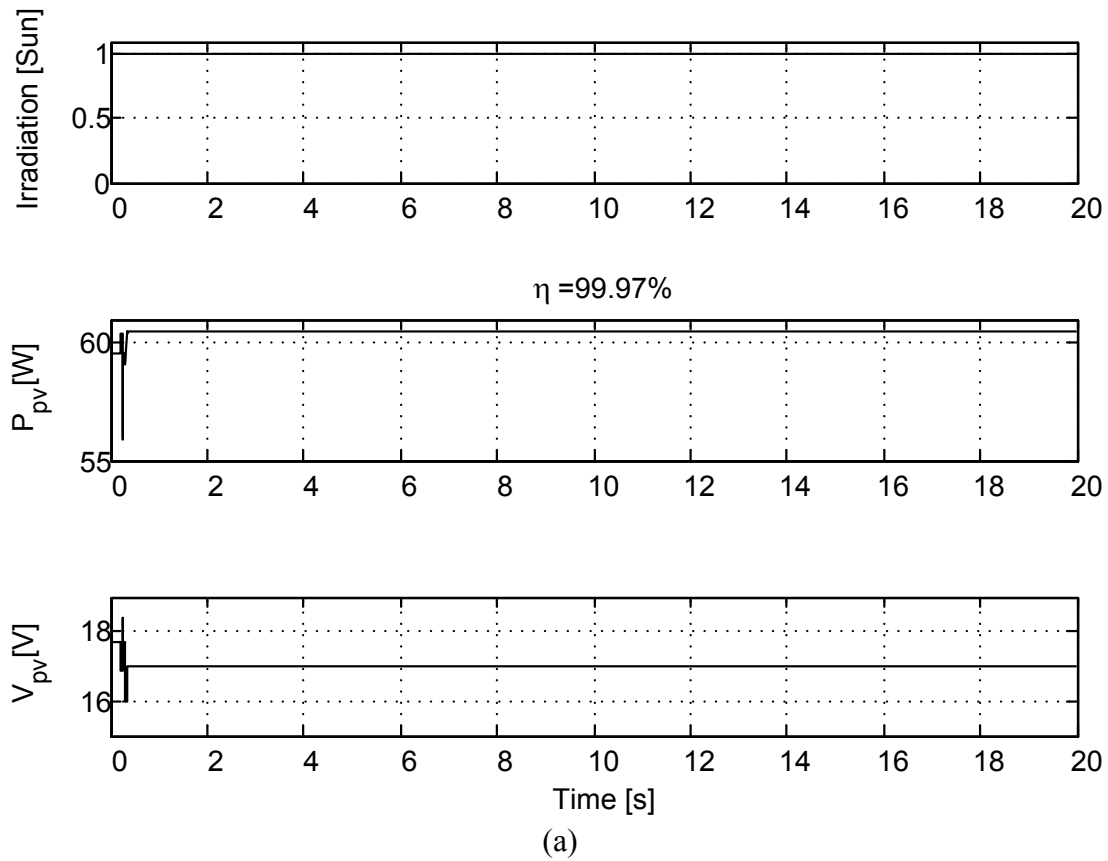


Figure 5.11 Steady state operation at the irradiation of 1 Sun. (a) Interpolation algorithm. (b) P&O- ΔV_{ref} algorithm.

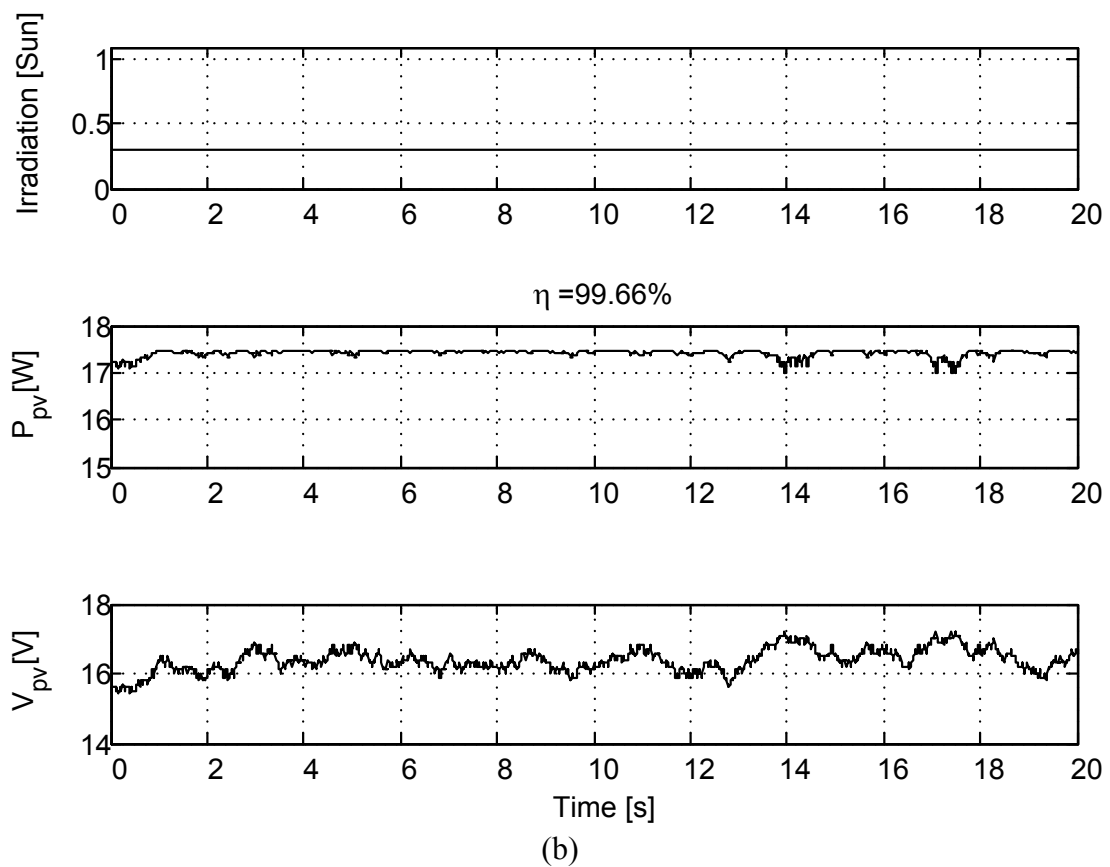
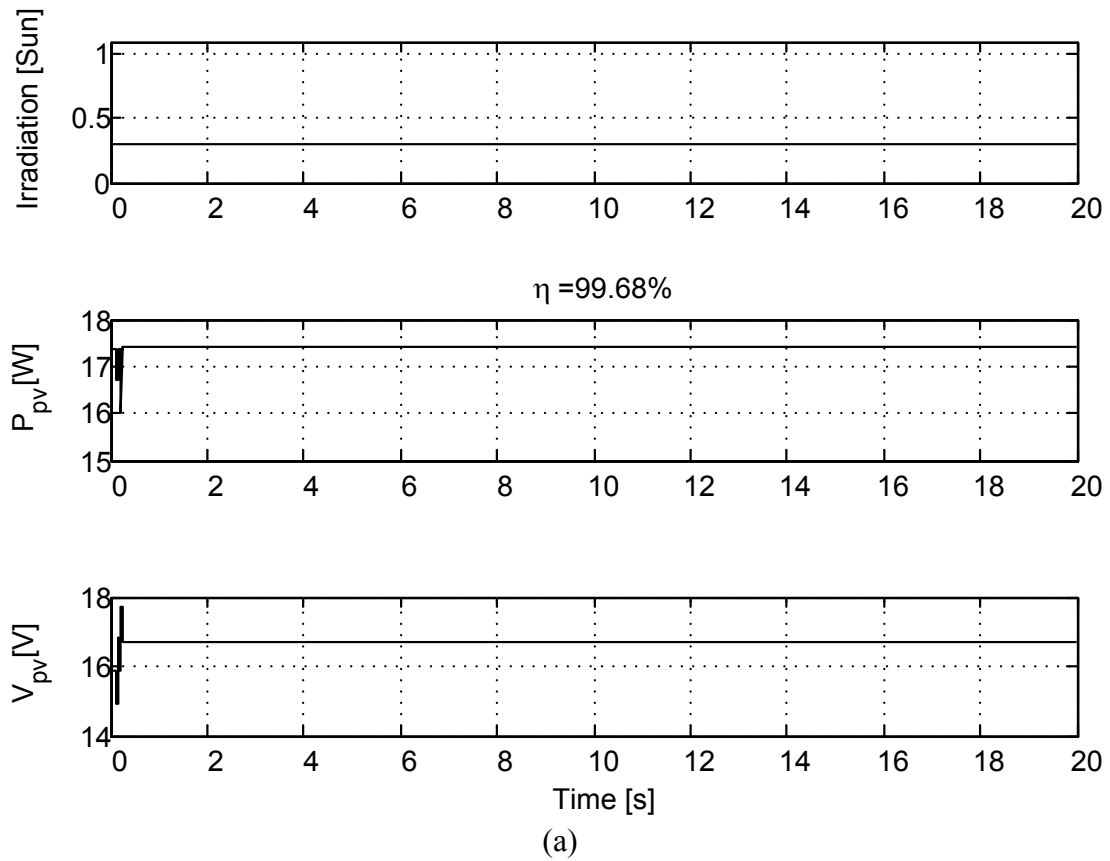


Figure 5.12 Steady-state operation at the irradiation of 0.3 Sun. (a) Interpolation algorithm. (b) P&O- ΔV_{ref} algorithm.

Figure 5.13 shows the algorithms operation during an increase of the irradiation level from 0.3 Sun to 1 Sun which lasts 1 s. It can be seen in Figure 5.13(b) that the P&O algorithm changes the operating point in the wrong direction during the irradiation change. The operation of the interpolation algorithm is shown in Figure 5.13(a). When the change in irradiation started the interpolation algorithm detected it but only after the irradiation became stable and a new operating point was calculated, while during the irradiation change the MPP was tracked approximately by the emulated load controller. It can be seen that the interpolation algorithm achieved significantly higher efficiency than the P&O algorithm. Figure 5.14 shows the algorithms operation during the irradiation decrease. In Figure 5.14(a) the initial operation of the interpolation algorithm took five measurements (two additional measurements were required because the result of first three measurements was not within the required range). It can be seen that the P&O algorithm does not change the operating point during irradiation decrease. The P&O- ΔV_{ref} achieved slightly better results. Similar tendencies can be noted in test for lower irradiation level in Figure 5.15 and Figure 5.16. The results for the P&O algorithm under changing irradiation agree with the description in [35]. If the irradiation increases between steps, the P&O algorithm will see the increase in power as a reason to make the next perturbation in the same direction as the previous one. If irradiation decreases between steps, the reduction of power will cause the P&O algorithm to reverse the direction of the perturbation at the next step. If this happens continuously then the algorithm will stay at a nearly constant point during the power decrease.

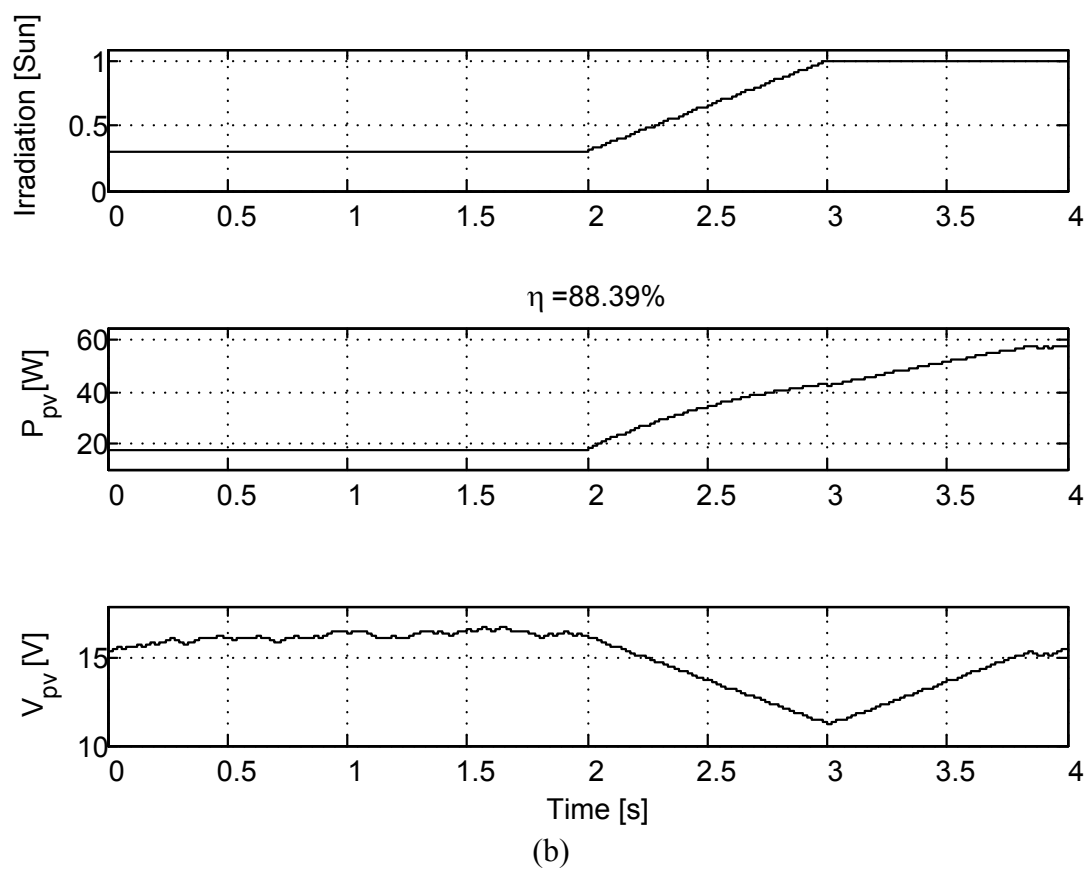
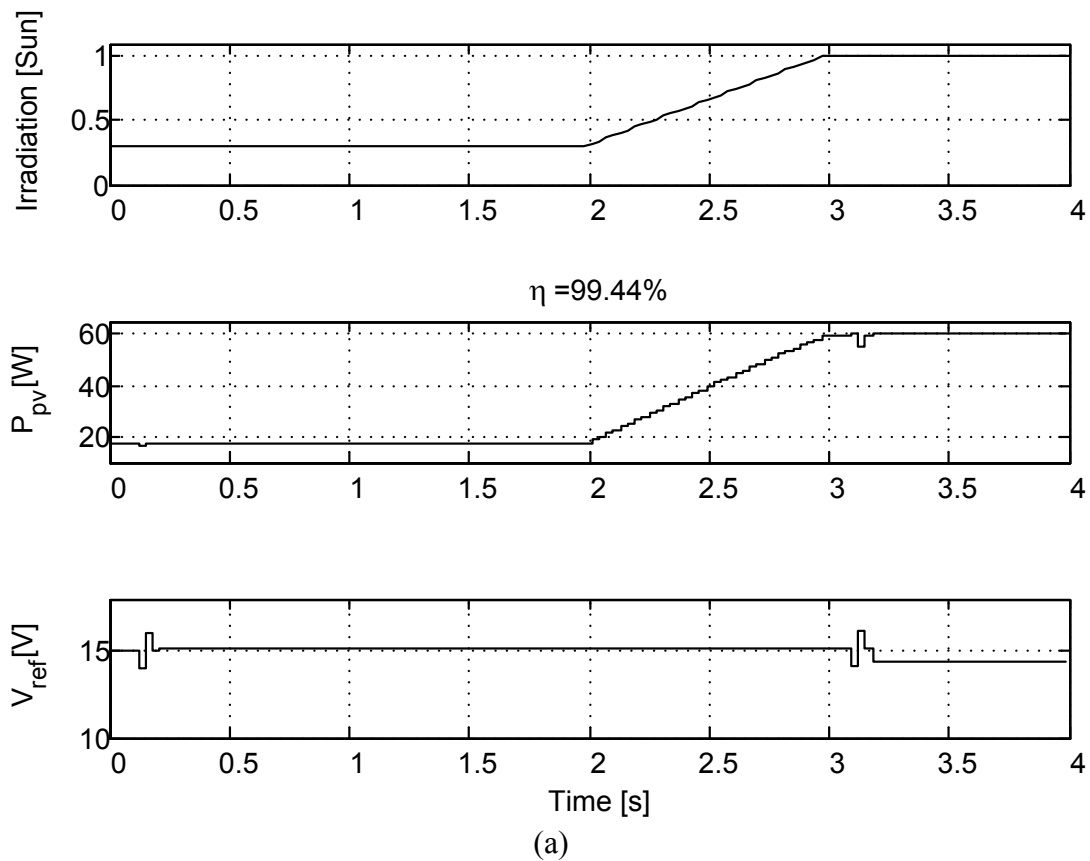


Figure 5.13 Operation during irradiation increase from 0.3 Sun to 1 Sun.

(a) Interpolation algorithm. (b) P&O- ΔV_{ref} algorithm.

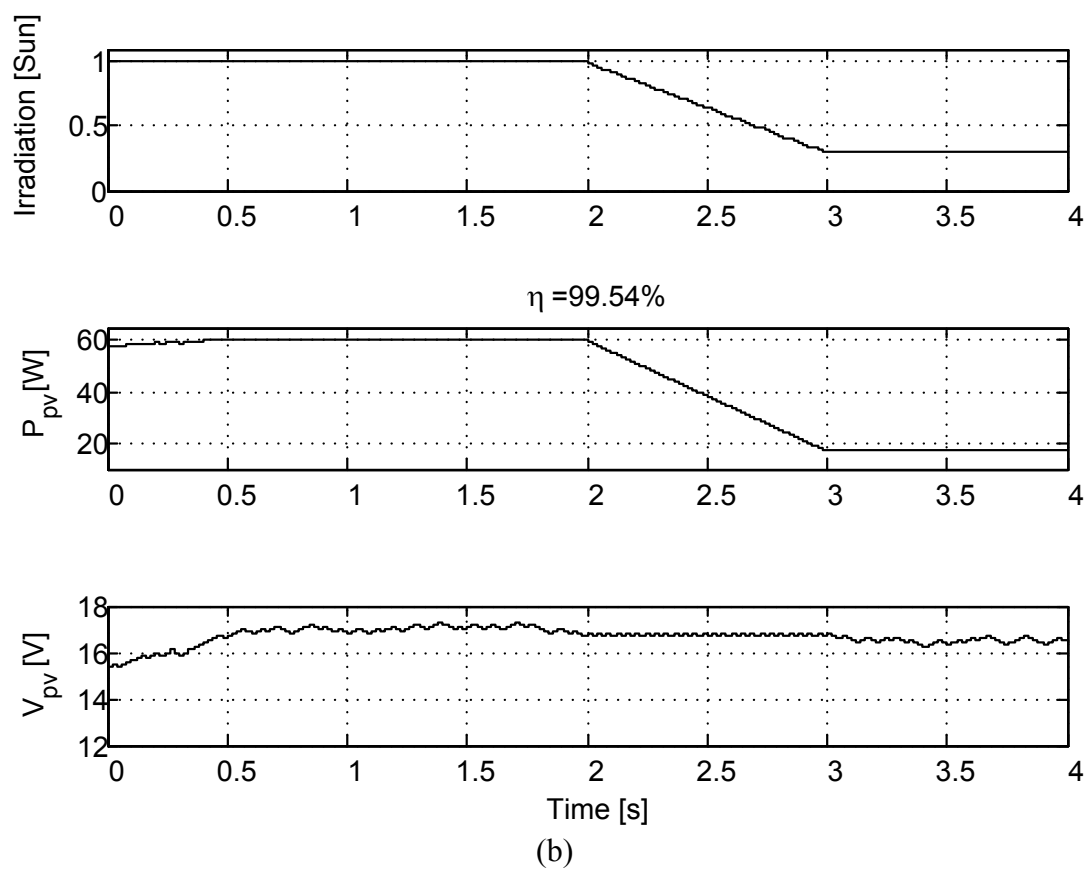
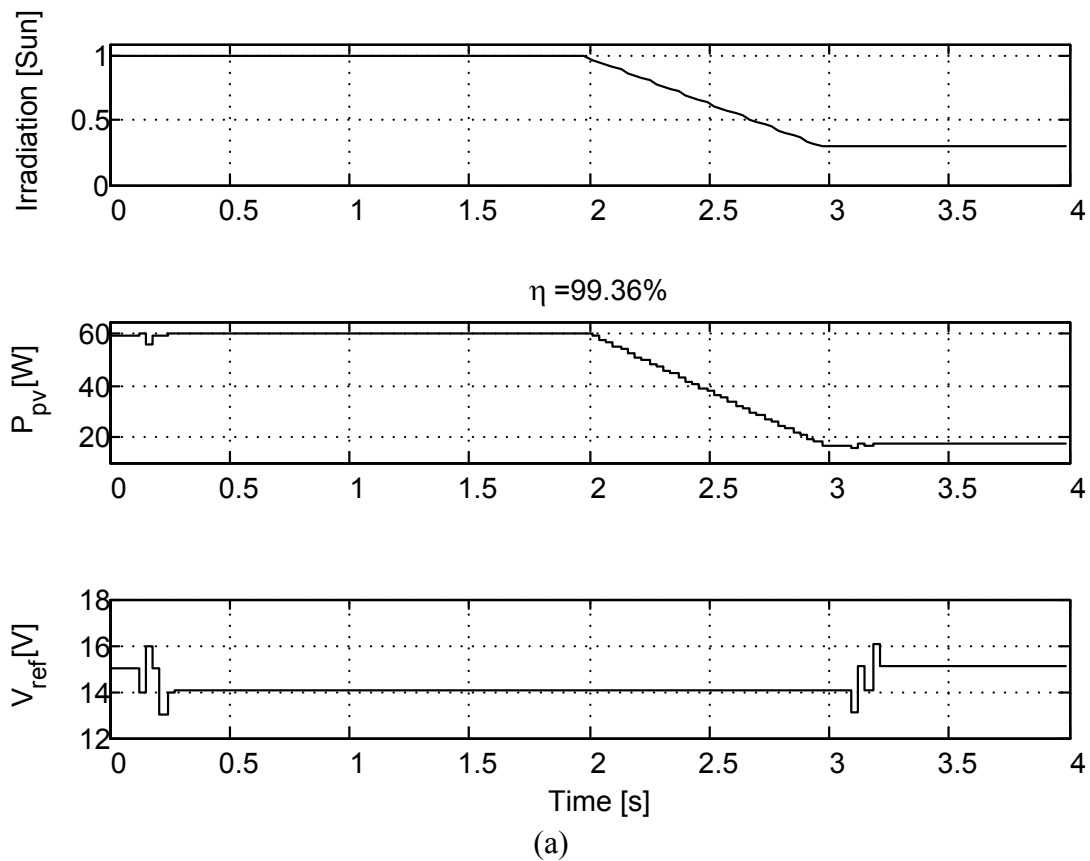
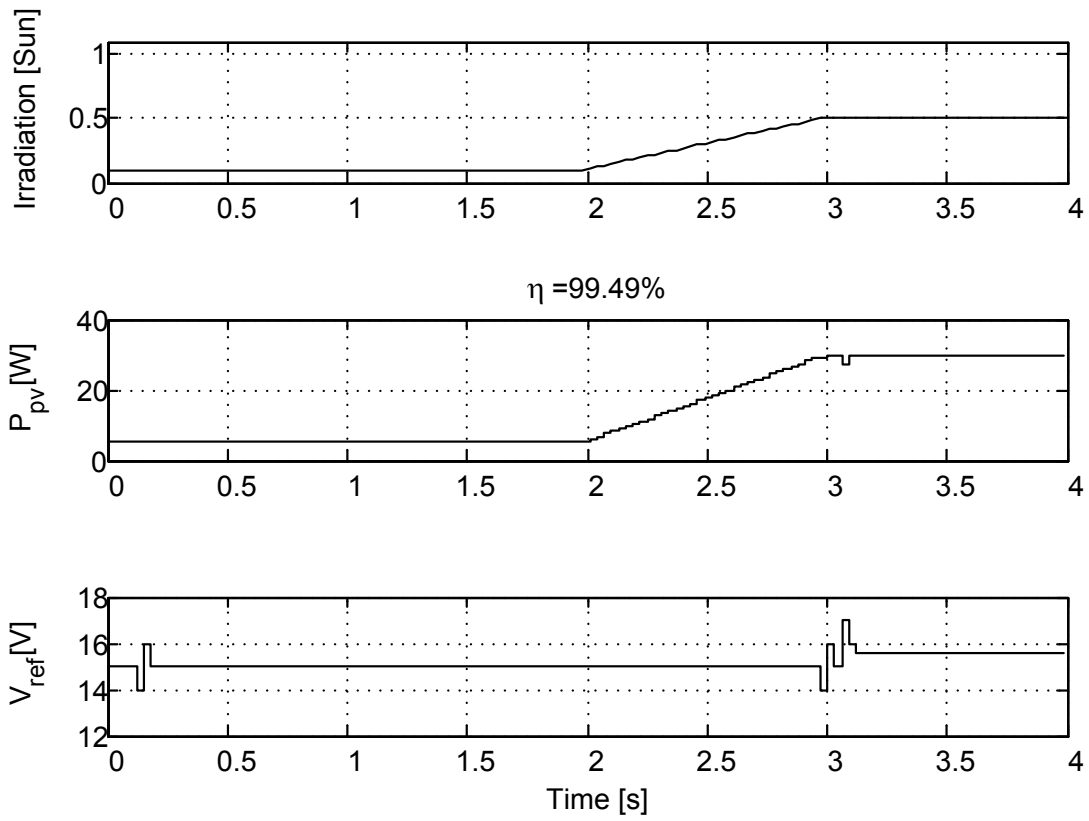
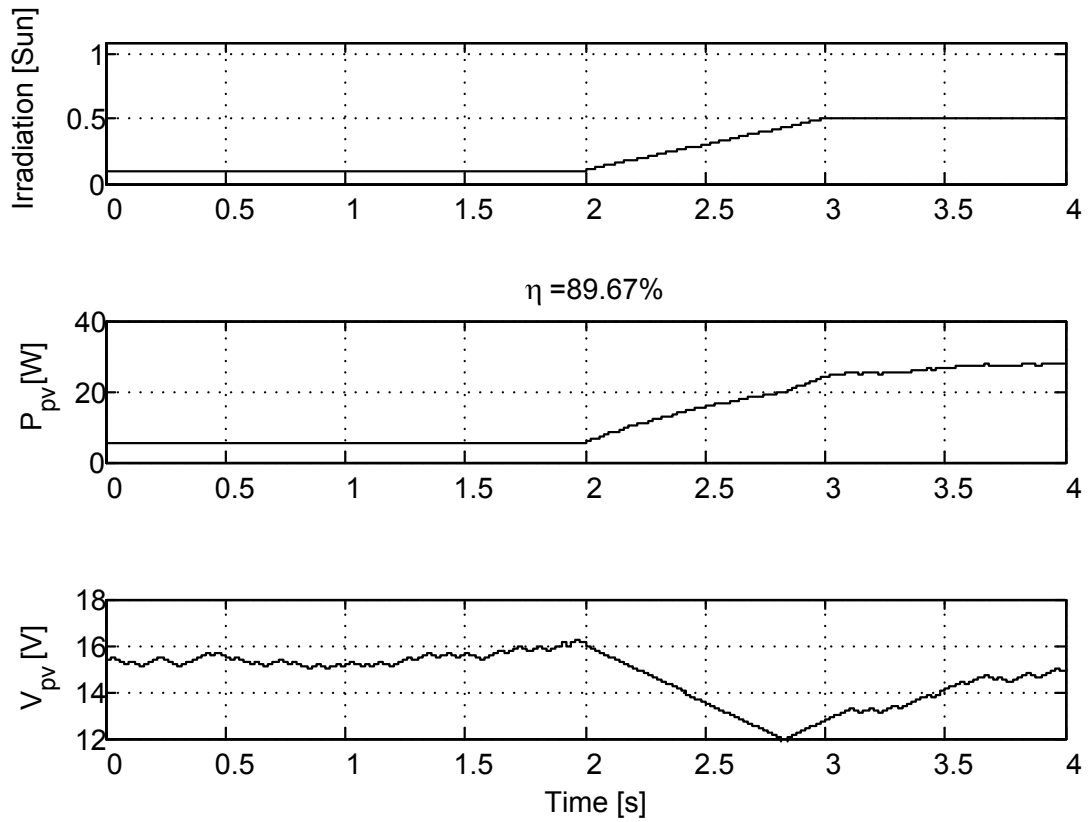


Figure 5.14 Operation during irradiation decrease from 1 Sun to 0.3 Sun.
 (a) Interpolation algorithm. (b) P&O- ΔV_{ref} algorithm.



(a)



(b)

Figure 5.15 Operation during irradiation increase from 0.1 Sun to 0.5 Sun.
 (a) Interpolation algorithm. (b) P&O- ΔV_{ref} algorithm.

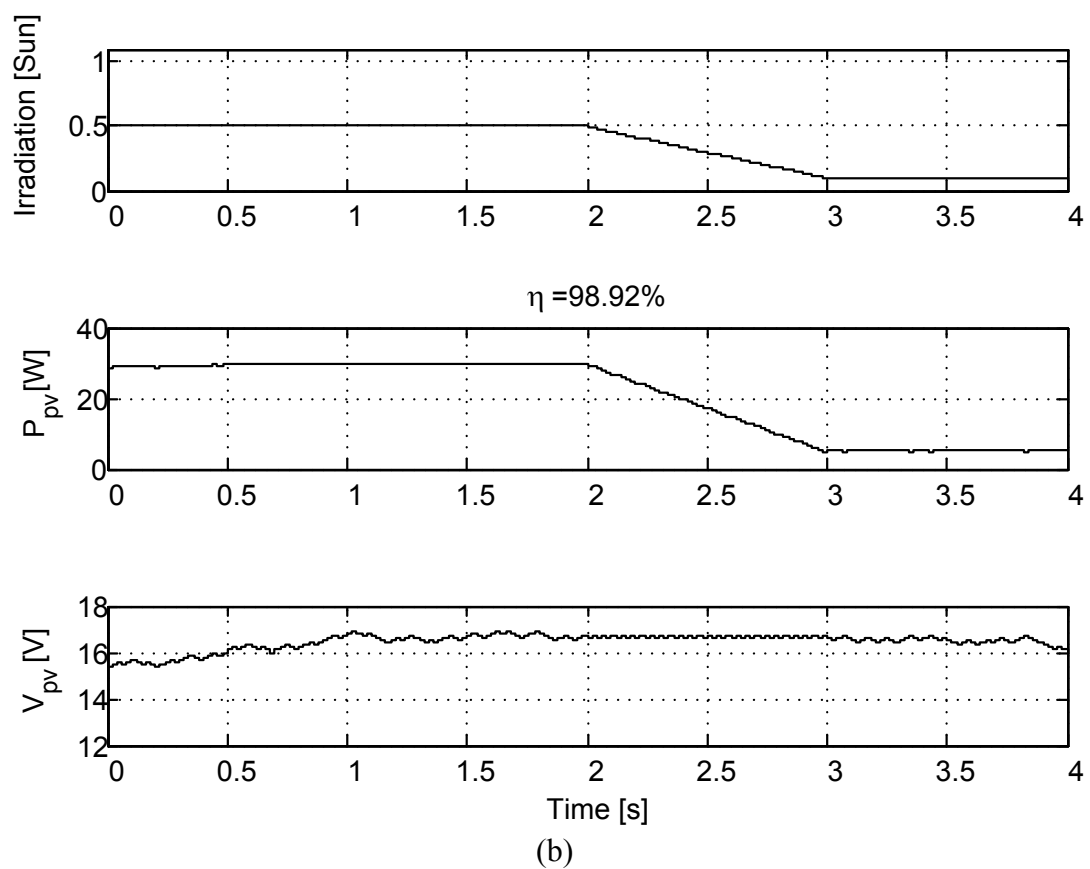
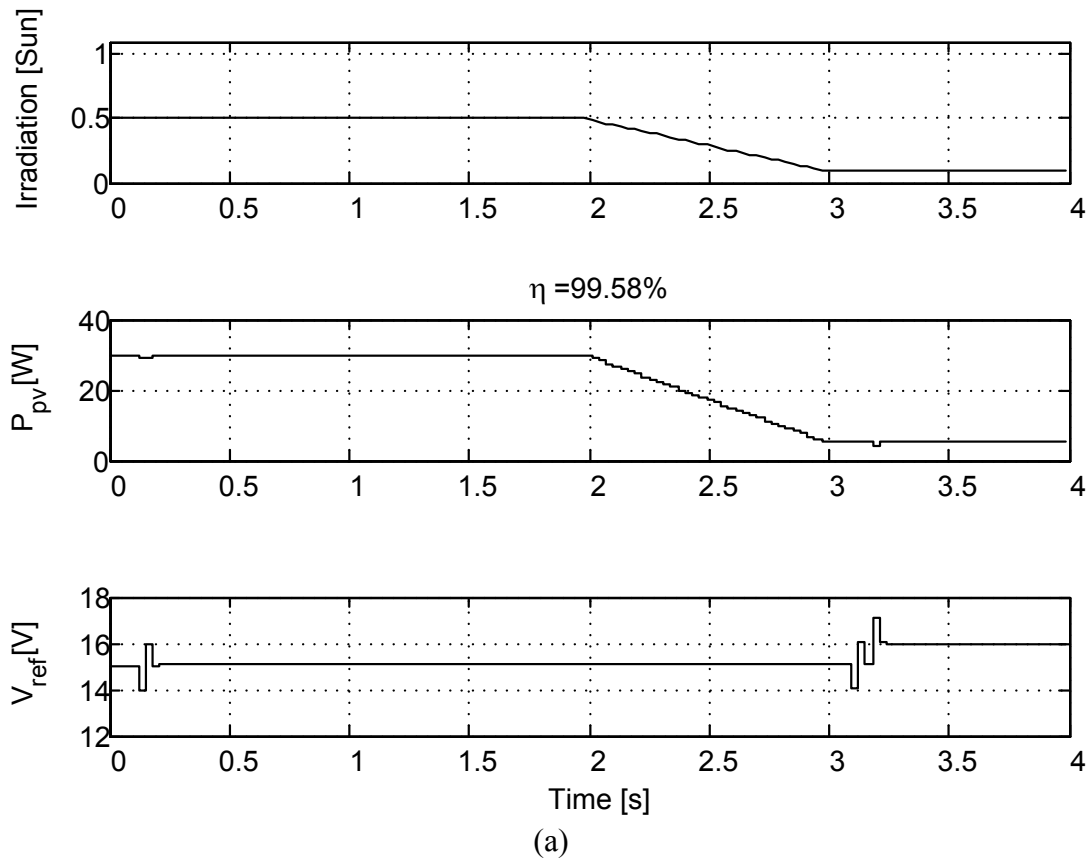


Figure 5.16 Operation during irradiation decrease from 0.5 Sun to 0.1 Sun.
 (a) Interpolation algorithm. (b) P&O- ΔV_{ref} algorithm.

5.6.2 Experimental results

The P&O and interpolation algorithms were tested experimentally on the setup described in section 4.2. The following were tested: P&O- ΔV_{ref} , two versions of the interpolation algorithm. All algorithms used the emulated load control scheme and the operating point was adjusted by the signal V_{ref} . The characteristic of the PV emulator is shown in Figure 5.17. For changing irradiation conditions the short circuit current I_{sc} was changed.

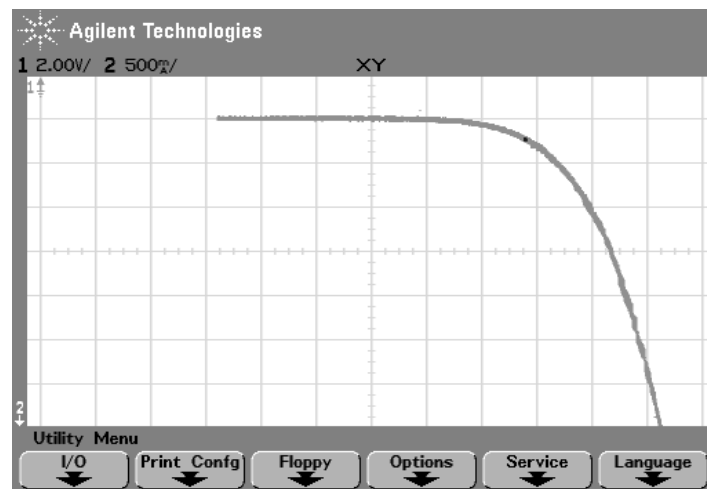


Figure 5.17 Characteristic of the PV emulator at short circuit current $I_{sc}=3.5$ A (x: 2V/div, y: 0.5A/div).

Figure 5.18-Figure 5.22 show the operation of different algorithms at different conditions. The following signals are shown, top to bottom: 1: V_{pv} 10V/div, 2: I_{pv} 2A/div, M1: Power 100W/div, 3: V_{ref} 5V/div, 4: I_{sc} (equivalent to irradiation) 2A/div. Figure 5.18 and Figure 5.19 show the steady-state operation of the P&O- ΔV_{ref} and interpolation algorithms respectively. Variations in the signals of the P&O- ΔV_{ref} algorithm due to perturbations can be noted while signals of the interpolation algorithm remain stable. The sampling and readjustment of the operating point by the interpolation algorithm can be seen at time 6.1 s in Figure 5.19.

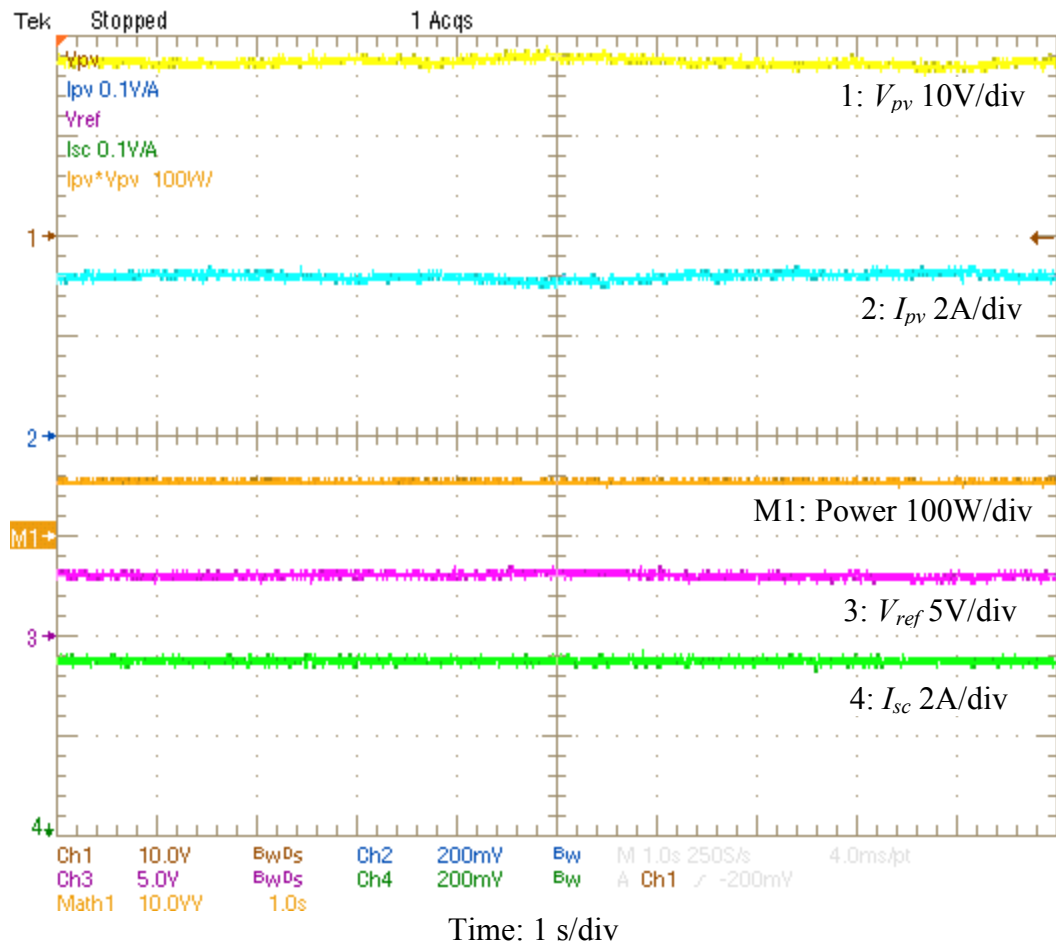


Figure 5.18 P&O- ΔV_{ref} algorithm at steady irradiation.

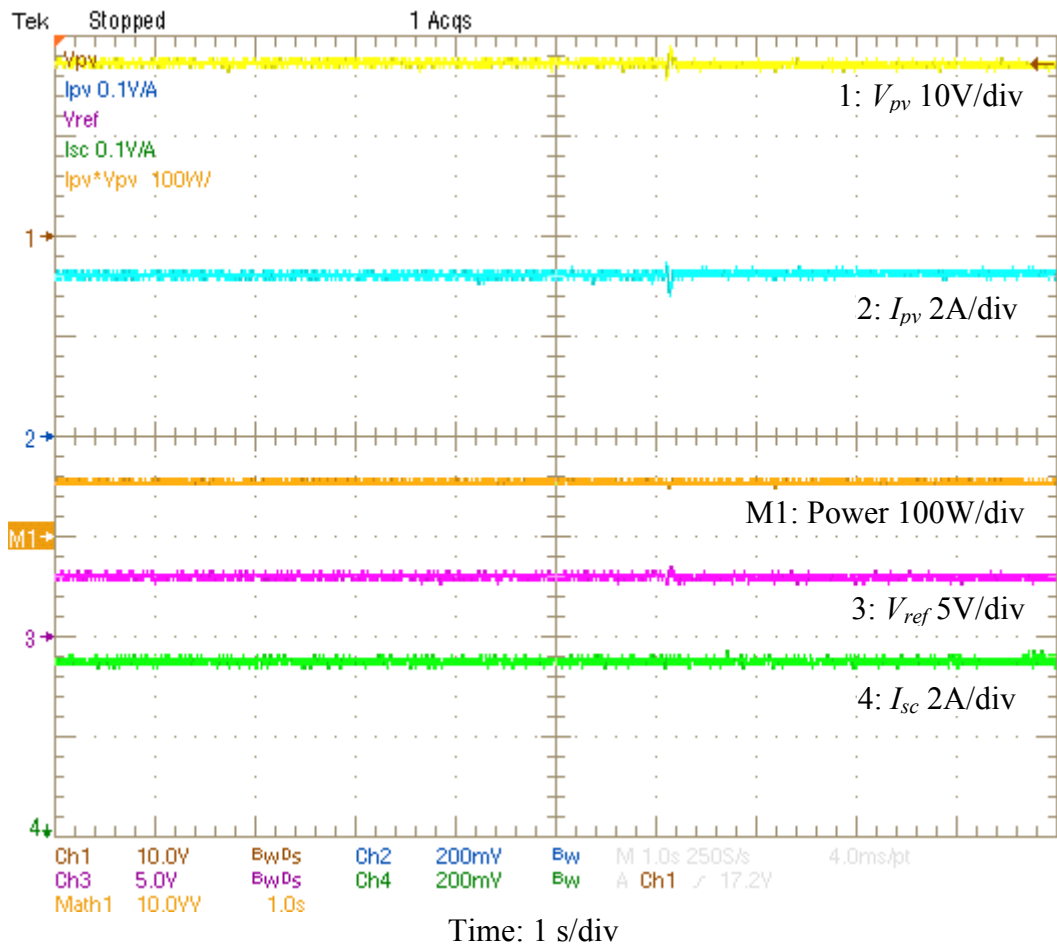


Figure 5.19 Interpolation algorithm at steady irradiation.

Figure 5.20 demonstrates operation of the P&O- ΔV_{ref} algorithm at changing irradiation conditions. Similar behaviour of the P&O- ΔV_{ref} algorithm to the behaviour shown in simulations in section 5.6.1 can be noted.

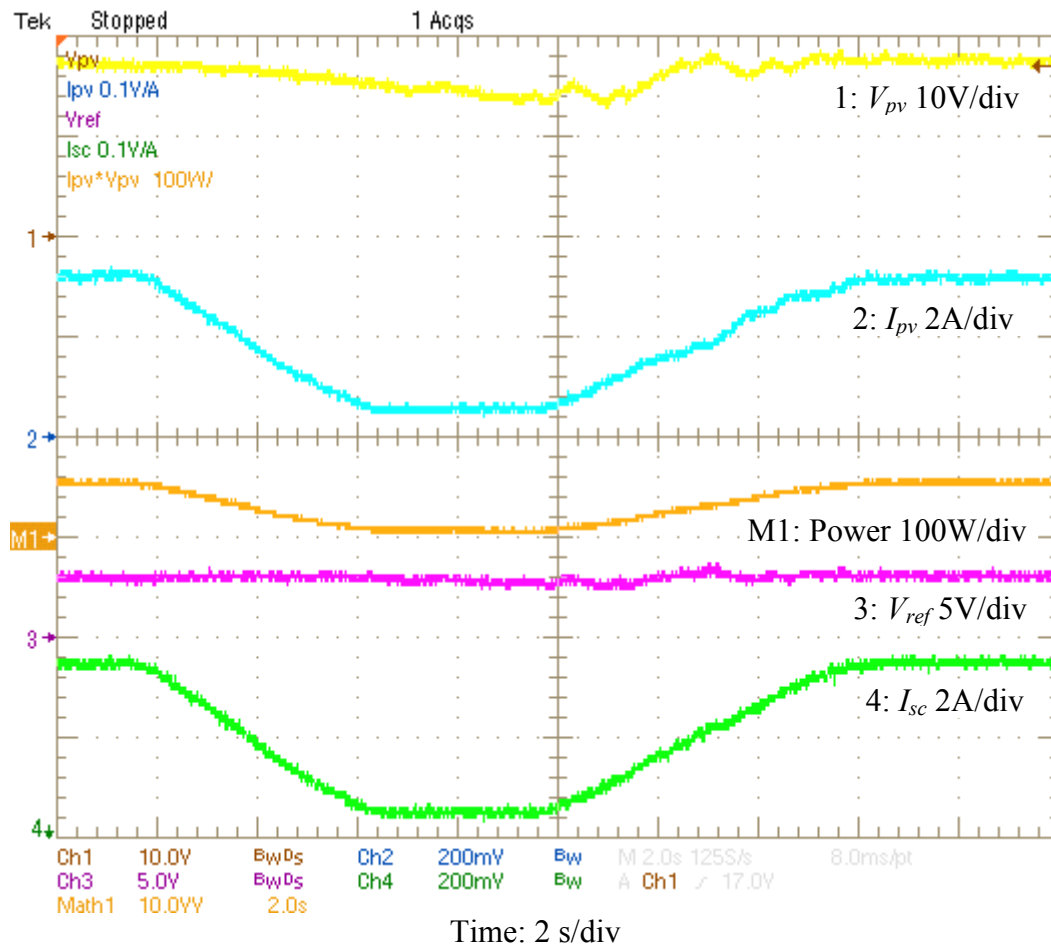


Figure 5.20 P&O- ΔV_{ref} algorithm at changing irradiation.

Figure 5.21 and Figure 5.22 show operation of the interpolation algorithm with measurement at constant time intervals and after detection of change in irradiation respectively. It can be seen in Figure 5.22 that the version of the algorithm that detects changes in irradiation readjusted the operating immediately when the irradiation became stable after change at the time 3.1 s and 7.2 s. But this version performed series of readjustment during slow change in irradiation at the time 4-5 s. However this could be caused by not continuous change in irradiation since it was changed manually.

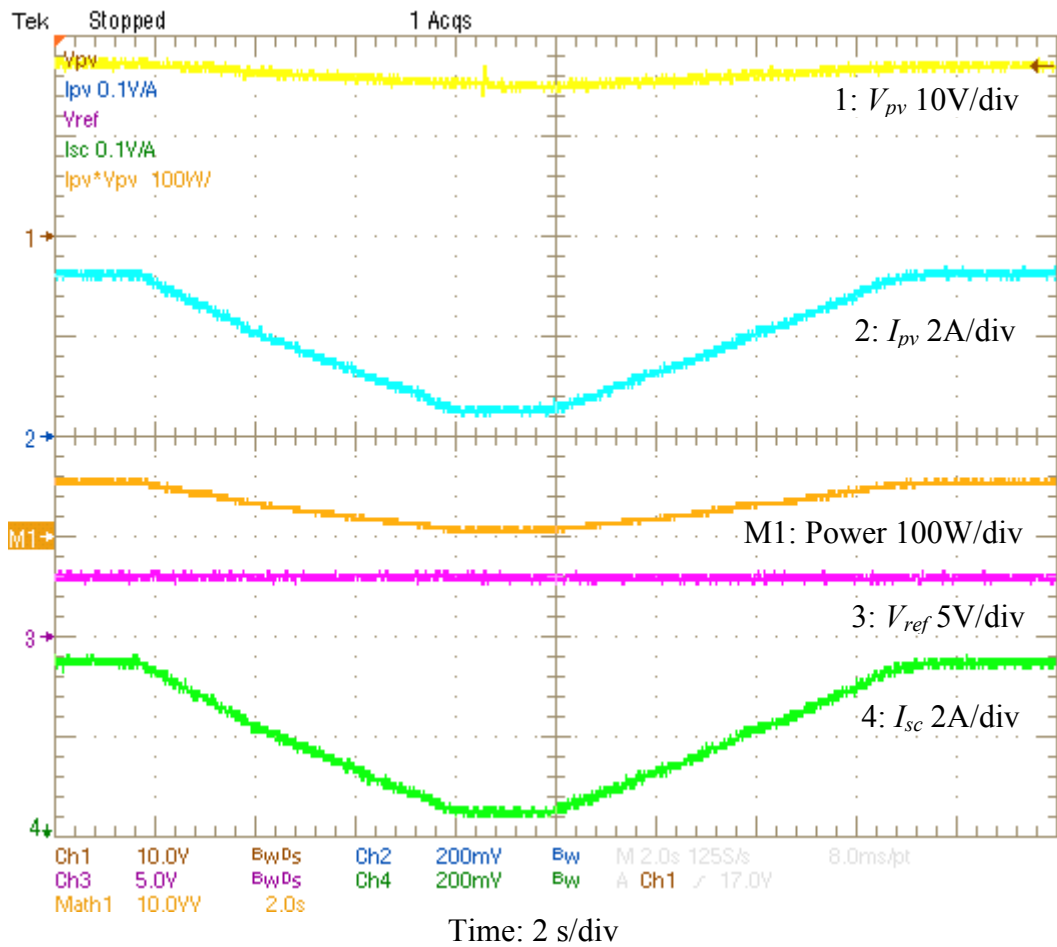


Figure 5.21 Interpolation algorithm at changing irradiation (version with measurement at constant long time intervals).

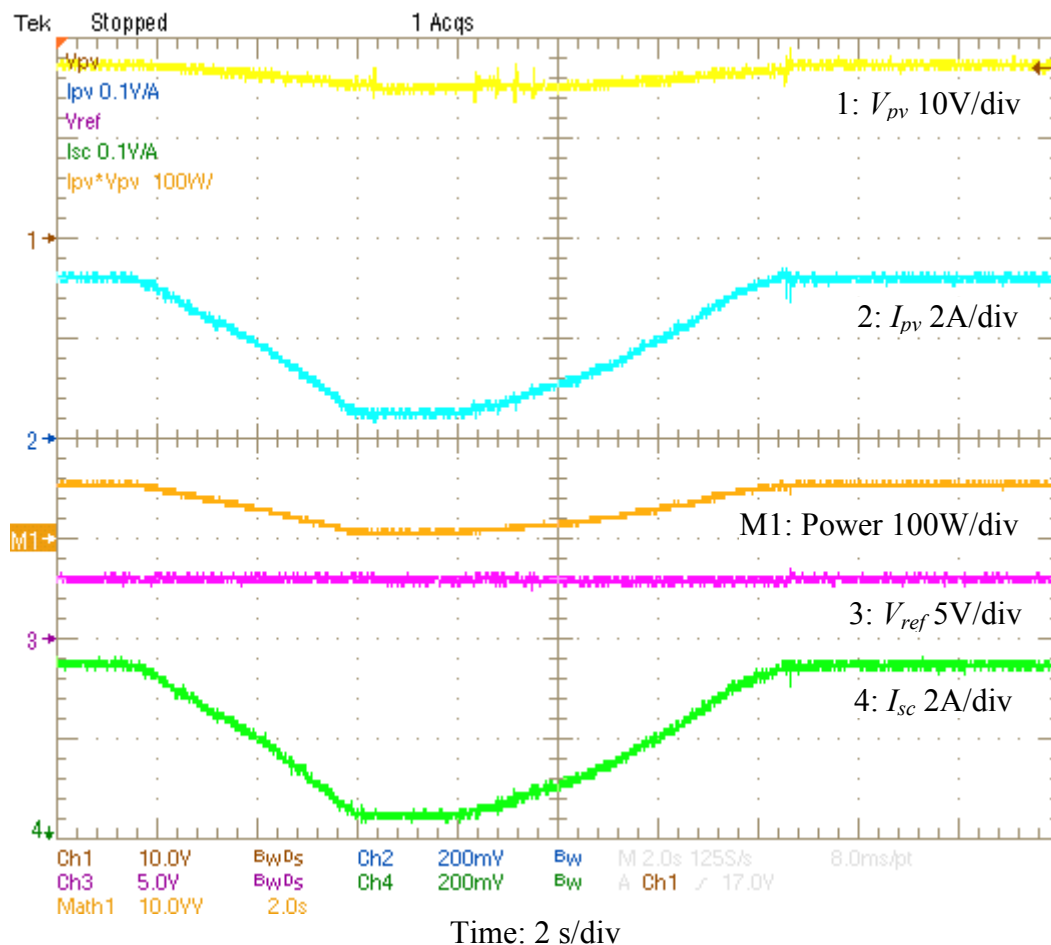


Figure 5.22 Interpolation algorithm at changing irradiation (version with measurement after change in irradiation is detected).

The interpolation and P&O- ΔV_{ref} algorithms convergence process from low PV voltage operating point were also tested at constant irradiation with a different PV emulator, characteristic of which is shown in Figure 5.23. Figure 5.24 and Figure 5.25 show the convergence process of the interpolation and P&O- ΔV_{ref} algorithms respectively. It can be seen that the interpolation algorithm reached the MPP about five times faster than the P&O- ΔV_{ref} algorithm. It worth noting that the algorithms parameters were not readjusted for a different PV characteristic, which shows robustness of the interpolation algorithm.

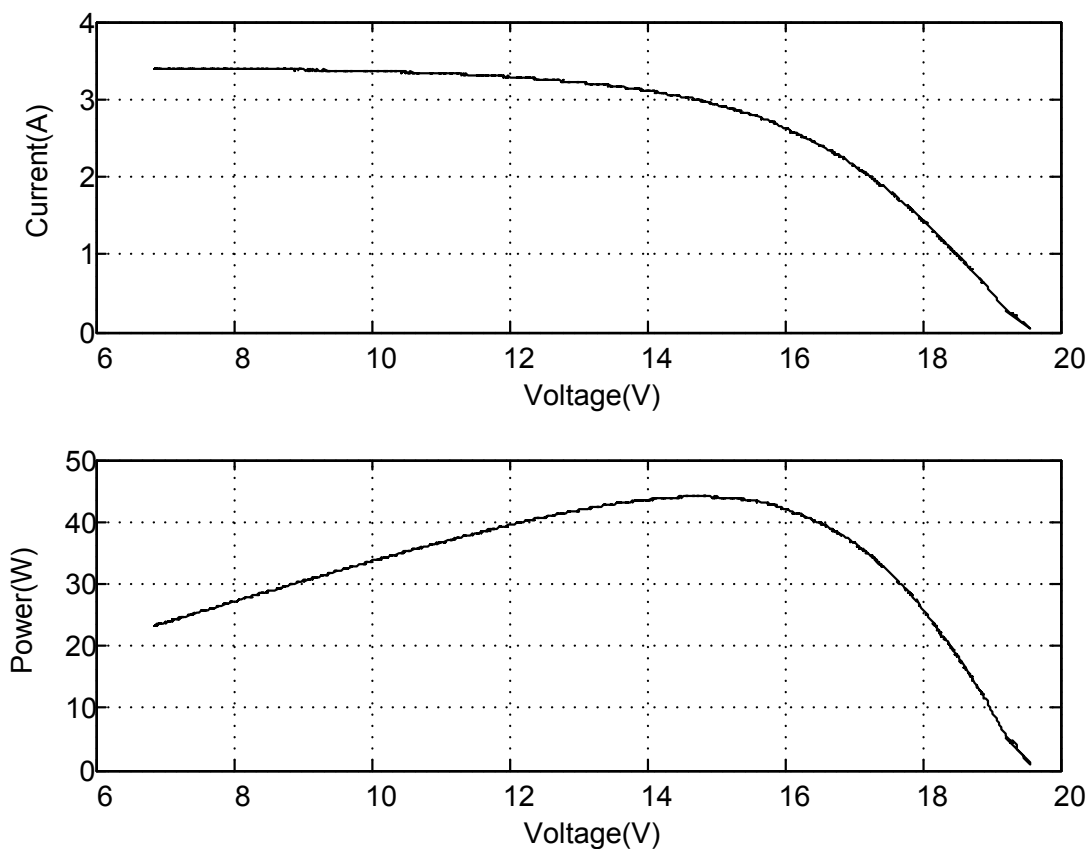


Figure 5.23 Characteristic of the PV emulator.

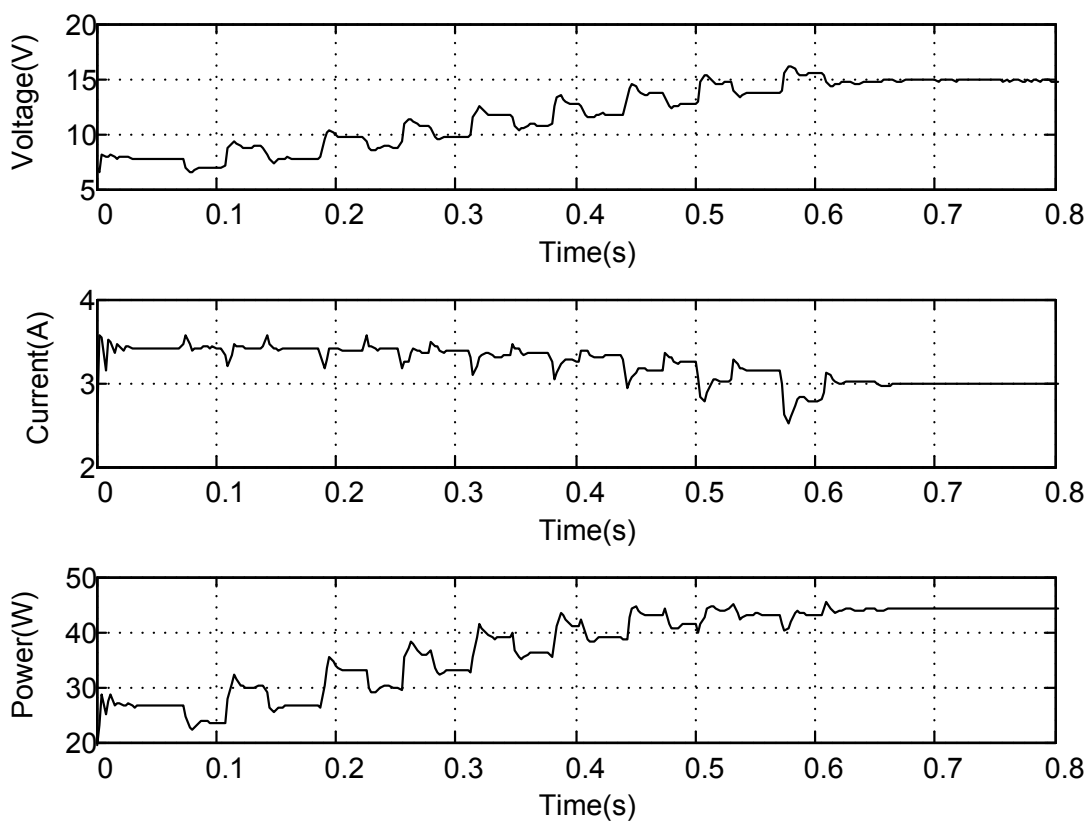


Figure 5.24 Convergence process of the interpolation algorithm.

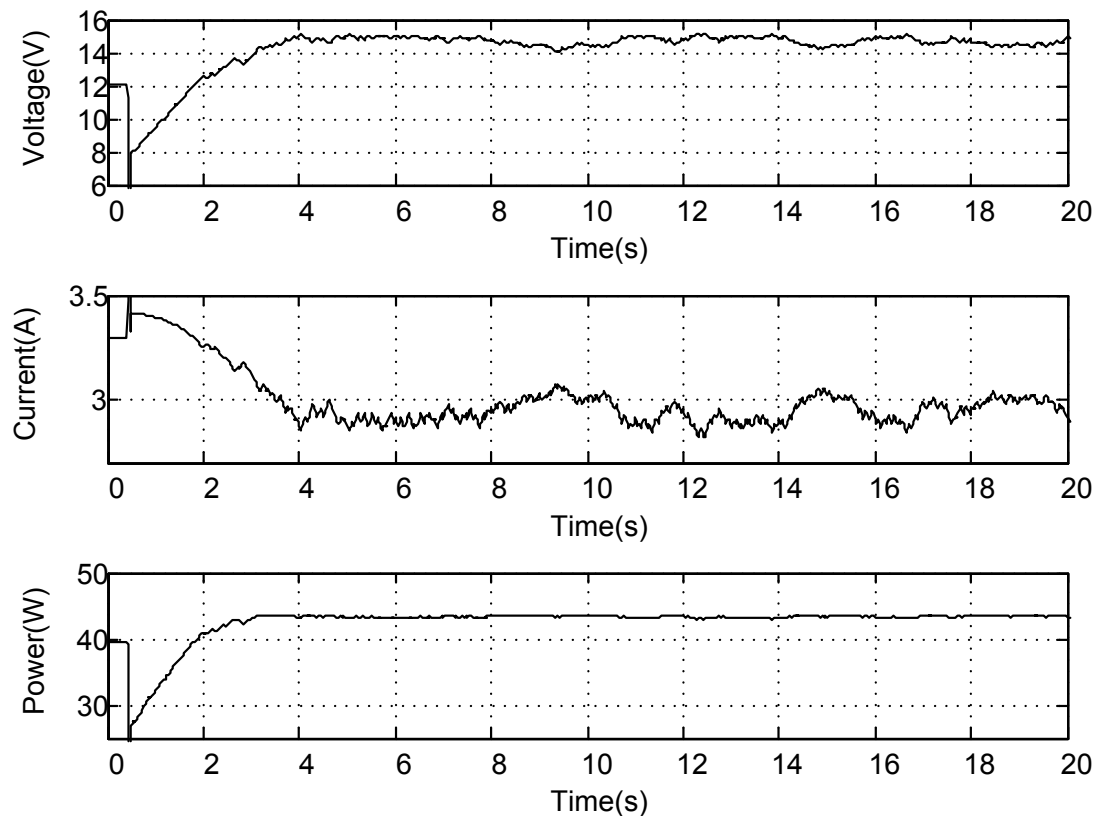


Figure 5.25 Convergence process of the P&O- ΔV_{ref} algorithm.

5.6.3 Simulation comparison with other algorithms according to EN 50530 standard

The P&O- ΔV_{ref} , dP-P&O and interpolation algorithms were tested in simulation according to the EN 50530 standard [65] for MPPT efficiency. The P&O- ΔV_{ref} algorithm was selected for comparison to the interpolation algorithm because it demonstrated good steady-state performance in tests in Chapter 4. The dP-P&O algorithm was selected because it is known to have better dynamic performance. The time between iterations was 0.4 s for P&O- ΔV_{ref} and dP-P&O algorithms and 0.6 s for the interpolation algorithm. Like in section 5.6.1, the measurement noise was taken into account. The test consists of static and dynamic efficiency parts. The static efficiency is calculated as weighted average of steady state efficiencies at different irradiation levels.

$$\eta = \sum_i W_i \eta_i \quad (5.8)$$

There are two sets of weights for calculating EU and CEC (California Energy Commission) efficiencies. Table 5.1 summarises the efficiencies of the tested algorithms at different irradiances and the calculated EU and CEC efficiencies. It can be seen that the interpolation method does not have best efficiency for lowest irradiation level but its average EU and CEC efficiencies are higher than in other tested algorithms.

Table 5.1 Static MPPT efficiency

Irradiation (Sun)	0.05	0.1	0.2	0.3	0.5	0.75	1		
EU weights	0.03	0.06	0.13	0.1	0.48	0	0.2	η_{EU} (%)	η_{CEC} (%)
CEC weights	0	0.04	0.05	0.12	0.21	0.53	0.05		
$\eta_{P\&O-\Delta V_{ref}}$ (%)	98.3	99	99.5	99.66	99.8	99.85	99.89	99.67	99.77
$\eta_{dP-P\&O}$ (%)	95.1	97.65	98.74	99.23	99.49	99.67	99.73	99.17	99.46
$\eta_{Interpolation}$ (%)	97.2	98.53	99.68	99.85	99.96	99.97	99.98	99.75	99.88

The dynamic efficiency measured in series of tests at irradiation profiles defined in the standard. The irradiation profile in each test consists of a number of sequences that include up and down ramps and dwell times between them as shown in Figure 5.26. There are two series of tests for low irradiances of 0.1-0.5 Sun and high irradiances of 0.3-1 Sun. The total dynamic efficiency of an algorithm is calculated as average of all dynamic tests. Table 5.2 summarises the results of dynamic tests. It can be seen that the interpolation algorithm does not have the best efficiency for all test, but it has better overall dynamic efficiency than other tested algorithms.

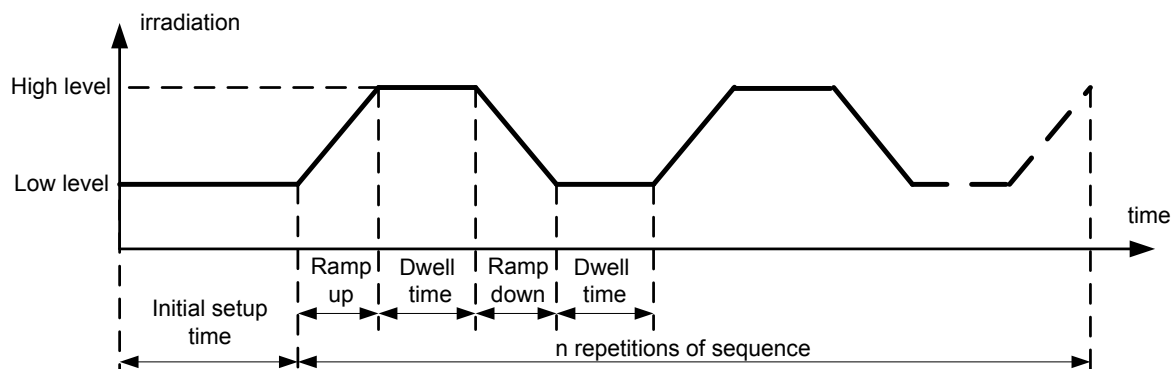


Figure 5.26 Irradiation profile for dynamic efficiency tests according to EN 50530 standard.

Table 5.2 Dynamic MPPT efficiency

Number of sequences	Slope (W/m ² /s)	Ramp up (s)	Dwell time (s)	Ramp down (s)	Dwell time (s)	$\eta_{\text{P\&O-}\Delta V_{\text{ref}}}$ (%)	$\eta_{\text{dP-P\&O}}$ (%)	$\eta_{\text{Interpolation}}$ (%)
Low irradiation 0.1-0.5 Sun								
2	0.5	800	10	800	10	99.7	99.2	99.7
2	1	400	10	400	10	99.6	99.2	99.7
2	2	200	10	200	10	99.6	99.1	99.5
3	3	133	10	133	10	99.6	99	99.4
4	5	80	10	80	10	99.5	98.9	99.3
6	7	57	10	57	10	99.4	98.8	99.2
8	10	40	10	40	10	99.2	98.8	99.2
10	14	29	10	29	10	98.7	98.6	99.5
10	20	20	10	20	10	96.1	98.7	99.5
10	30	13	10	13	10	90.6	98.6	99.5
10	50	8	10	8	10	94.1	98.5	99.4
High irradiation 0.3-1 Sun								
10	10	70	10	70	10	99.7	99.6	99.2
10	14	50	10	50	10	99.6	99.6	98.5
10	20	35	10	35	10	99	99.5	98.6
10	30	23	10	23	10	95	99.5	98.5
10	50	14	10	14	10	93.7	99.5	98.5
10	100	7	10	7	10	97.6	99.4	98.1
Total η_{dynamic} (%)						97.69	99.09	99.14

Table 5.3 summarises the efficiencies of three algorithms according to EN 50530 standard. It can be seen that the interpolation algorithm has better efficiency in both static and dynamic tests, while P&O- ΔV_{ref} and dP-P&O algorithms showed good performance only in one of tests.

Table 5.3 MPPT efficiency according to EN 50530 standard.

Algorithm	$\eta_{\text{EU}}(\%)$	$\eta_{\text{CEC}}(\%)$	$\eta_{\text{dynamic}}(\%)$
P&O- ΔV_{ref}	99.67	99.77	97.69
dP-P&O	99.17	99.46	99.09
Interpolation	99.75	99.88	99.14

Chapter 6

Conclusions

6.1 *Concluding Remarks*

This work aimed to develop small-signal models of grid connected PV systems for grid stability analysis. Although there is no small-signal model of a PV system that incorporate the commonly used MPPT algorithms, this work suggests a solution for detailed modelling of grid connected PV systems. This solution is based on development of a new interpolation MPPT algorithm that actively involves changing the PV operating point only for short periods of time. The rest of the time the PV system is controlled by the emulated load controller while the MPPT algorithm only monitors the operating point and its changes. The emulated load controller tracks the MPP approximately during irradiation changes providing high MPPT efficiency. The small-signal state space model of a PV system that consists of a boost dc-dc converter, PV power source and the emulated load controller is provided. The model was verified against time domain simulations of the system and a good match between signals shape was demonstrated. The model was tested with several loads types including a variable current source, constant voltage source and a constant resistance. This can be used for inclusion of the proposed PV system model in larger models of the electrical grid. The model was also used for finding minimal time intervals of the MPPT algorithms as limited by the converter dynamics. Since modelling of switching mode power converters is well established, this method can be readily adopted for various converter topologies.

Clearly, the developed model will accurately represent the physical system only if the proposed MPPT method is actually used. An MPPT interpolation algorithm was developed and effort was made to ensure good system performance with this algorithm. The

interpolation MPPT method was designed to find the MPP quickly and accurately and includes mechanisms that prevent it from moving the operating point incorrectly during changing irradiation conditions. Simulations and experimental tests showed the advantage of the proposed method in both static and dynamic environmental conditions. The interpolation algorithm was developed and optimised taking measurement noise into account. In addition, tests of other MPPT methods that were conducted for comparison by taking the measurement noise into consideration there also. The developed technique of testing MPPT algorithms with noise allowed work to be conducted of performance on comparison of different MPPT algorithms in presence of noise.

It is known that noise present in measured signals in photovoltaic (PV) systems can have a detrimental effect on Maximum Power Point Tracking (MPPT) but systematic studies are few. In this work, noise in voltage and current measurements is modelled and as a combination of quantization, switching ripple and white Gaussian noise and compared to experimental measurements. The full noise model and a Gaussian simplified noise model are incorporated in simulations of four MPPT variants for a range of step sizes and irradiation levels. The results show that the Gaussian noise assumption can be used for large step sizes. The simulation method used can be simply applied to various MPPT algorithms. From the insights gained from these results, guidance is provided for selection of the most suitable algorithm to use in the presence of noise and for the adjustment of algorithm parameters. Also, the importance of testing MPPT in the presence of noise was demonstrated. It was found that algorithms that would be considered to perform similarly if no presence of noise is assumed actually have different MPPT efficiency.

6.2 Future work

A natural continuation of this work is incorporating the developed here PV system model in grid models for stability analysis. Such modelling would be an important

contribution to the effort of analysis of the electrical grid with a high influence of distributed generation. In previously developed micro-grid models, several power generators were controlled to share the power demand using frequency droop. On the contrary, when renewable sources are connected to the grid it is desirable to enable the renewable sources to produce maximum possible energy while the rest of the demanded power production is shared between the non renewable sources. On the other hand if the power production by the renewable sources exceeds the power demand, the renewable sources should stop the MPPT operation and share the power production while non renewable generators should be switched off. Hence new grid control techniques needed to be developed for both cases and for smooth transition between them. The model developed in this work can help for modelling and stability analysis of future grid control methods.

The MPPT method proposed in this work was optimised using the target system parameters in simulations. Even though the MPPT performed well even in different conditions from those for which it was optimised, it would be useful to develop methods for automatic adjustment of the MPPT algorithm parameters. The parameters that need to be adjusted are the step size and the boundaries of low error region. In addition the parameter r of the emulated load controller can be adjusted automatically. The parameter adjustments could be based on an initial procedure that is conducted upon system installation or on an ongoing monitoring process.

A MPPT solution based on 2nd order polynomial interpolation was developed as part of this work. It was shown that interpolation of the same set of points conducted in different axis systems can have different levels of accuracy. A rotation of the axis was suggested here to reduce the interpolation error. It could be useful in future to develop a theoretical background for manipulations with axes in which the interpolation is conducted. In particular, it would be interesting to see how axis transformations influence the interpolation error and

how transformation that provides minimal error can be chosen. Such work could be useful in many fields and applications other than MPPT.

Author's publications

Previous publications

M. Sokolov, D. Shmilovitz, "A Photovoltaic Maximum Power Point Tracking Scheme Realizing" Nearly Optimal Load Emulation", *IEEE 24th Convention of Electrical & Electronics Engineers in Israel*, Nov. 2006, pp. 381-383.

M. Sokolov, D. Shmilovitz, "Photovoltaic Maximum Power Point Tracking based on an Adjustable Matched Virtual Load", *IEEE Applied Power Electronics Conference (APEC'07)*, Feb. 2007, pp. 1480-1484. (Also presented at Aegean Conference on Electric Machines, Power Electronics and Electromotion Joint Conference (ACEMP'07), Sept. 2007.)

M. Sokolov, D. Shmilovitz, "A Modified MPPT Scheme for Accelerated Convergence", *IEEE Transactions on Energy Conversion*, vol.23, no.4, pp.1105-1107, Dec. 2008.

M. Sokolov, D. Shmilovitz, "Linear load line emulation based maximum power point tracking", *IEEE Power Electronics Specialists Conference (PESC'08)*, June. 2008, pp. 4098-4101.

Publications derived from this work

M. Sokolov, T.C. Green, P.D. Mitcheson, D. Shmilovitz, "Dynamic analysis of photovoltaic system with MPP locus emulation", *2010 IEEE 26th Convention of Electrical and Electronics Engineers in Israel (IEEEI)*, Nov. 2010, pp. 212-215.

M. Sokolov, T.C. Green, P.D. Mitcheson, D. Shmilovitz, "Small-signal Model of Photovoltaic Power Converter for Selection of Perturb and Observe Algorithm Step Time", *14th European Conference on Power Electronics and Applications, EPE 2011*, Sept. 2011, pp. 1-5.

M. Sokolov, T.C. Green, P.D. Mitcheson, D. Shmilovitz, "Practical Considerations of Noise Effects on Maximum Power Point Algorithms in Photovoltaic Systems", in preparation.

Bibliography

- [1] B. Azzopardi, J. Mutale, D. Kirschen, "Cost boundaries for future PV solar cell modules," *IEEE International Conference on Sustainable Energy Technologies, ICSET 2008*, pp.589–594, 24–27 Nov. 2008.
- [2] L.R. Brown, *Plan B 3.0: Mobilizing to Save Civilization*. New York, USA: Earth Policy Institute, 2008.
- [3] C. Herig, "Solar Power: Using photovoltaics to preserve California's electricity capacity reserves", NREL, USA, Report No. NREL/BR-520-31179, Sept. 2001.
- [4] P. Eiffert, G.J. Kiss, "Building-Integrated Photovoltaic Designs for Commercial and Institutional Structures: A Sourcebook for Architects", NREL, USA, Report No. BK-520-25272, Feb. 2000.
- [5] T.C. Green, P.D. Mitcheson, D. Shmilovitz, *Building Energy Management for Integration of Photovoltaic Energy*, Imperial College London, Tel Aviv University, Alan Howard Scholarship Proposal, February 2008.
- [6] N. Jenkins et al., "Introduction," in *Embedded Generation*, London, UK: IEE, 2000, ch.1 sec. 1.4, pp. 9–11.
- [7] J.H.R. Enslin, P.J.M. Heskes, "Harmonic interaction between a large number of distributed power inverters and the distribution network," *IEEE Transactions on Power Electronics*, vol.19, no.6, pp. 1586–1593, Nov. 2004.
- [8] E. Ares, O. Hawkins and P. Bolton, "Feed-in Tariffs: Solar PV Review", *UK Parliament Standard notes*, SN/SC/6112, April 2012. <http://www.parliament.uk/briefing-papers/SN06112>.
- [9] P. Kundur, *Power System Stability and Control*, New York, McGraw-Hill, 1994.
- [10] N. Pogaku, M. Prodanovic, T.C. Green, "Modeling, Analysis and Testing of Autonomous Operation of an Inverter-Based Microgrid," *IEEE Transactions on Power Electronics*, vol.22, no.2, pp.613–625, March 2007.
- [11] N. Pogaku, *Analysis, Control and Testing of Inverter-Based Distributed Generation in Standalone and Grid-Connected Applications*, Ph.D. thesis, Imperial College London, 2006.
- [12] D.P. Hohm and M.E. Ropp, "Comparative study of maximum power point tracking algorithms," *Progress Photovoltaics: Res. Appl.*, vol. 11, no. 1, pp. 47–62, Jan. 2003.
- [13] Z. Zinger, A. Braunstein, "Dynamic Matching of a Solar-Electrical (Photovoltaic) System An Estimation of the Minimum Requirements on the Matching System," *IEEE Transactions on Power Apparatus and Systems*, vol.PAS-100, no.3, pp.1189–1192, March 1981.
- [14] T. Esumi and P.L. Chapman, "Comparison of photovoltaic array maximum power point tracking techniques," *IEEE Transactions Energy Conversion*, vol. 22, no. 2, pp. 439–449, Jun. 2007.
- [15] G. Petrone, G. Spagnuolo, R. Teodorescu, M. Veerachary, M. Vitelli, "Reliability Issues in Photovoltaic Power Processing Systems," *IEEE Transactions on Industrial Electronics*, vol.55, no.7, pp.2569–2580, July 2008.

- [16] E. Koutroulis, K. Kalaitzakis, and N. Voulgaris, "Development of a Microcontroller-based, Photovoltaic Maximum Power Point Tracking Control System", *IEEE Transactions on Power Electronics*, vol. 16, no 1, pp. 46–54, Jan 2001.
- [17] Yun Tiam Tan, D.S. Kirschen and N. Jenkins, "A Model of PV Generation Suitable for Stability Analysis," *IEEE Transactions Energy Conversion*, vol. 19, no. 4, pp. 748–755, Dec. 2004.
- [18] I. Laird, H. Lovatt, N. Savvides, D. Lu, V. G. Agelidis, "Comparative study of maximum power point tracking algorithms for thermoelectric generators," *Australasian Universities Power Engineering Conference, 2008. AUPEC '08*, pp.1–6, 14–17 Dec. 2008.
- [19] N. Kasa, T. Iida, L. Chen, "Flyback Inverter Controlled by Sensorless Current MPPT for Photovoltaic Power System," *IEEE Transactions on Industrial Electronics*, vol.52, no.4, pp. 1145–1152, Aug. 2005.
- [20] R. Gules, J. De Pellegrin Pacheco, H.L. Hey, J. Imhoff, "A Maximum Power Point Tracking System With Parallel Connection for PV Stand-Alone Applications," *IEEE Transactions on Industrial Electronics*, vol.55, no.7, pp.2674–2683, July 2008.
- [21] Jung-Min Kwon, Bong-Hwan Kwon, Kwang-Hee Nam, "Three-Phase Photovoltaic System With Three-Level Boosting MPPT Control," *IEEE Transactions on Power Electronics*, vol.23, no.5, pp.2319–2327, Sept. 2008.
- [22] Fangrui Liu, Shanxu Duan, Fei Liu, Bangyin Liu, Yong Kang, "A Variable Step Size INC MPPT Method for PV Systems," *IEEE Transactions on Industrial Electronics*, vol.55, no.7, pp.2622–2628, July 2008.
- [23] J.A. Jiang, T.L. Huang, Y.T. Hsiao and C.H. Chen, "Maximum Power Tracking for Photovoltaic Power Systems", *Tamkang Journal of Science and Engineering*, Vol. 8, No 2, 2005, pp. 147–153.
- [24] D. Sera, R. Teodorescu, J. Hantschel, M. Knoll, "Optimized Maximum Power Point Tracker for Fast-Changing Environmental Conditions," *IEEE Transactions on Industrial Electronics*, vol.55, no.7, pp.2629–2637, July 2008.
- [25] S. Dahal, N. Mithulananthan, T.K. Saha, "Assessment and Enhancement of Small Signal Stability of a Renewable-Energy-Based Electricity Distribution System," *IEEE Transactions on Sustainable Energy*, vol.3, no.3, pp.407–415, July 2012.
- [26] Mao Xiaolin, R. Ayyanar, "Average and Phasor Models of Single Phase PV Generators for Analysis and Simulation of Large Power Distribution Systems," *Twenty-Fourth Annual IEEE Applied Power Electronics Conference and Exposition, 2009, APEC 2009*, pp.1964-1970, 15–19 Feb. 2009.
- [27] A. Hamadi, S. Rahmani, K. Al-Haddad, Y.A. Al-Turki, "A three-phase three wire grid-connect photovoltaic energy source with Sepic converter to track the Maximum Power Point," *IECON 2011 - 37th Annual Conference on IEEE Industrial Electronics Society*, pp.3087-3092, 7–10 Nov. 2011.
- [28] W. Du, H.F. Wang, R. Dunn, "Power system small-signal oscillation stability as affected by large-scale PV penetration," *International Conference on Sustainable Power Generation and Supply, 2009, SUPERGEN '09*, pp.1–6, 6–7 April 2009.
- [29] G.J. Kish, J.J. Lee, P.W. Lehn, "Modelling and control of photovoltaic panels utilising the incremental conductance method for maximum power point tracking," *IET Renewable Power Generation*, vol.6, no.4, pp.259–266, July 2012.

- [30] M.A.S. Masoum, H. Dehbonei, E.F. Fuchs, "Theoretical and experimental analyses of photovoltaic systems with voltage and current-based maximum power-point tracking," *IEEE Transactions Energy Conversion*, vol. 17, no. 4, pp. 514–522, Dec. 2002.
- [31] C. Hua and J.R. Lin, "DSP-based controller application in battery storage of photovoltaic system," in *Proc. IEEE IECON 22nd Int. Conf. Ind. Electron., Contr. Instrum.*, 1996, pp. 1705–1710.
- [32] L. Zhang, A. Al-Amoudi, and Y. Bai, "Real-time maximum power point tracking for grid-connected photovoltaic systems," in *Proc. Eighth Int. Conf. Power Electronics Variable Speed Drives*, 2000, pp. 124–129.
- [33] Y.C. Kuo, T.J. Liang, J.F. Chen, "Novel Maximum-Power-Point-Tracking Controller for Photovoltaic Energy Conversion System", *IEEE Transactions on Industrial Electronics*, Vol. 48, No. 3, June 2001, pp. 594–601.
- [34] N. Femia, G. Petrone, G. Spagnuolo, and M. Vitelli, "Optimization of perturb and observe maximum power point tracking method," *IEEE Transactions on Power Electronics*, vol.20, no.4, pp. 963–973, July 2005.
- [35] O. Waszynczuk, "Dynamic Behavior of a Class of Photovoltaic Power Systems," *IEEE Transactions on Power Apparatus and Systems*, vol.PAS-102, no.9, pp. 3031–3037, Sept. 1983.
- [36] H. Al-Atrash, I. Batarseh, K. Rustom, "Effect of Measurement Noise and Bias on Hill-Climbing MPPT Algorithms," *IEEE Transactions on Aerospace and Electronic Systems*, vol.46, no.2, pp.745–760, April 2010.
- [37] A.M. Latham, C.R. Sullivan, K.M. Odame, "Performance of photovoltaic maximum power point tracking algorithms in the presence of noise," *2010 IEEE Energy Conversion Congress and Exposition (ECCE)*, pp.632–639, 12–16 Sept. 2010.
- [38] M. Sokolov, *Emulated Linear Load Based Maximum Power Point Tracking for Photovoltaic Systems*, M.Sc. thesis, Tel Aviv University, 2008.
- [39] K.H. Hussein, I. Muta, T. Hoshino, M. Osakada, "Maximum photovoltaic power tracking: an algorithm for rapidly changing atmospheric conditions", *IEE Proceedings - Generation, Transmission and Distribution*, Vol. 142, no. 1, Jan. 1995, pp. 59–64.
- [40] S.B. Kjaer, "Evaluation of the "Hill Climbing" and the "Incremental Conductance" Maximum Power Point Trackers for Photovoltaic Power Systems," *IEEE Transactions on Energy Conversion*, vol.27, no.4, pp.922–929, Dec. 2012.
- [41] M. Sokolov, D. Shmilovitz, "A Modified MPPT Scheme for Accelerated Convergence," *IEEE Transactions on Energy Conversion*, vol.23, no.4, pp.1105–1107, Dec. 2008.
- [42] J. Wyatt, L. Chua, "Nonlinear resistive maximum power theorem, with solar cell application," *IEEE Transactions on Circuits and Systems*, vol.30, no.11, pp. 824–828, Nov. 1983.
- [43] A. Al-Diab, C. Sourkounis, "Variable step size P&O MPPT algorithm for PV systems," *2010 12th International Conference on Optimization of Electrical and Electronic Equipment (OPTIM)*, pp.1097–1102, 20v22 May 2010.
- [44] N. Khaehintung, K. Pramotung, B. Tuvirat, and P. Sirisuk, "RISC microcontroller built-in fuzzy logic controller of maximum power point tracking for solar-powered light-flasher applications", in *Proc. 30th Annu. Conf. IEEE Ind. Electron. Soc.*, 2004, pp. 2673–2678.

- [45] L. Zhang, Y. Bai, and A. Al-Amoudi, "GA-RBF neural network based maximum power point tracking for grid-connected photovoltaic systems", in *Proc. Int.Conf. Power Electron., Machines and Drives*, 2002, pp. 18–23.
- [46] K. Irisawa, T. Saito, I. Takano, Y. Sawada, "Maximum power point tracking control of photovoltaic generation system under non-uniform insolation by means of monitoring cells," in *Proc. 28th IEEE Photovolt. Spec. Conf.*, 2000, pp. 1707–1710.
- [47] K. Kobayashi, I. Takano, Y. Sawada, "A study on a two stage maximum power point tracking control of a photovoltaic system under partially shaded insolation conditions", *IEEE Power Engineering Society General Meeting*, July 2003, Vol. 4, pp. 2612–2617.
- [48] T. Shimizu, M. Hirakata, T. Kamezawa, H. Watanabe, "Generation control circuit for photovoltaic modules", *IEEE Transactions on Power Electronics*, Vol. 16, Issue 3, May 2001, pp. 293–300.
- [49] Xiao Weidong, W.G. Dunford, P.R. Palmer, A. Capel, "Regulation of Photovoltaic Voltage," *IEEE Transactions on Industrial Electronics*, vol.54, no.3, pp.1365–1374, June 2007.
- [50] R.W. Erickson, D. Maksimovic, *Fundamentals of Power Electronics*, Second Edition, Springer, 2001.
- [51] M.A. Green, *Solar Cells*, University of New South Wales, 1992.
- [52] G.R. Walker, "Evaluating MPPT converter topologies using a MATLAB PV model", *Australasian Universities Power Engineering Conference, AUPEC'00*, Vol. 1, Brisbane, 2000, pp. 138–143.
- [53] M. Sokolov, T.C. Green, P.D. Mitcheson, D. Shmilovitz, "Small-signal model of photovoltaic power converter for selection of Perturb and Observe algorithm step time," *Proceedings of the 2011-14th European Conference on Power Electronics and Applications (EPE 2011)*, pp.1–5, Aug. 30 2011–Sept. 1, 2011.
- [54] D.M. Van de Sype, K. De Gussemé, A.P. Van den Bossche, J.A.A. Melkebeek, "A sampling algorithm for digitally controlled boost PFC converters," *IEEE Transactions on Power Electronics*, vol.19, no.3, pp. 649–657, May 2004.
- [55] E. Bianconi, J. Calvente, R. Giral, E. Mamarelis, G. Petrone, C.A. Ramos-Paja, G. Spagnuolo, M. Vitelli, "A fast current-based MPPT technique employing sliding mode control," *IEEE Transactions on Industrial Electronics*, vol.60, no.3, pp.1168–1178, March 2013.
- [56] Y. Levron, D. Shmilovitz, "Maximum Power Point Tracking Employing Sliding Mode Control", *IEEE Transactions on Circuits and Systems I: Regular Papers*, vol.60, no.3, pp. 724–732, March 2013.
- [57] J.P. Rooney, "Aging in electronic systems," *Proceedings. Annual Reliability and Maintainability Symposium*, 1999, pp.293–299, 18–21 Jan 1999.
- [58] M. Calavia, J.M. Perié, J.F. Sanz and J. Sallán, "Comparison of MPPT strategies for solar modules", *International Conference on Renewable Energies and Power Quality, (ICREPQ'10), Granada (Spain)*, pp. 1–6, 23–25 March, 2010.
- [59] Jing Hu, Jiancheng Zhang, Hongbo Wu, "A novel MPPT control algorithm based on numerical calculation for PV generation systems," *IEEE 6th International Power Electronics and Motion Control Conference*, 2009. IPEMC '09, pp. 2103–2107, 17–20 May 2009.

- [60] R.M. Chao, S.H. Ko, F.S. Pai, I.H. Lin, C.C. Chang, "Evaluation of a photovoltaic energy mechatronics system with a built-in quadratic maximum power point tracking algorithm" *Solar Energy*, Vol. 83, Issue 12, December 2009, pp. 2177–2185.
- [61] Fu-Sheng Pai, Ru-Min Chao, "A New Algorithm to Photovoltaic Power Point Tracking Problems With Quadratic Maximization," *IEEE Transactions on Energy Conversion*, vol.25, no.1, pp.262–264, March 2010.
- [62] Qiu Pei-chun, Ge Bao-ming, Bi Da-qiang, "An improved MPPT method for photovoltaic power generation system," *2010 2nd IEEE International Symposium on Power Electronics for Distributed Generation Systems (PEDG)*, pp.144–147, 16–18 June 2010.
- [63] Richard L. Burden, J. Douglas Faires. *Numerical Analysis, 9th edition*. Boston, MA: Brooks Cole, 2011.
- [64] V. Scarpa, S. Buso, G. Spiazzi, "Low-Complexity MPPT Technique Exploiting the PV Module MPP Locus Characterization," *IEEE Transactions on Industrial Electronics*, vol.56, no.5, pp.1531–1538, May 2009.
- [65] *Overall Efficiency of Grid Connected Photovoltaic Inverters*, BS EN 50530:2010, BSI, BSI Standards Publication, 2010.

Appendix A

Calculation of a maximum point using interpolation

The interpolation algorithm is based on approximation of PV panel characteristic to a parabola that intersects the PV characteristic at sampling points. Since this algorithm is intended for real-time operation, the calculation complexity should be minimised. This appendix describes the calculation of maximum point of a parabola (x_m, f_m) that intersects with three given points (x_0, f_0) , (x_1, f_1) , (x_2, f_2) as shown in Figure A.1.

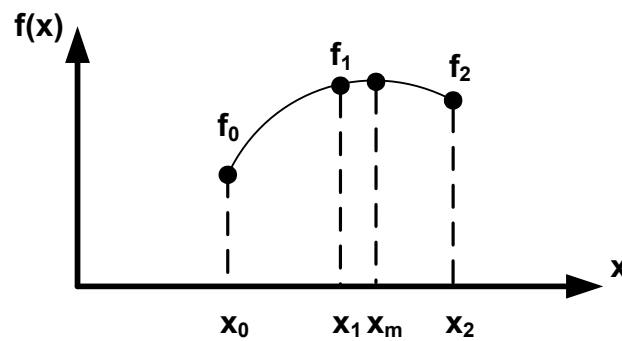


Figure A.1 Schematic illustration of the sampled points and parabola that intersects them.

Second order interpolation polynomial is given by:

$$P_2(x) = a_0 + a_1x + a_2x^2 \quad (\text{A.1})$$

Since the three sampled points belong to the parabola, the coefficients a_0 , a_1 and a_2 can be found solving the system:

$$\begin{pmatrix} 1 & x_0 & x_0^2 \\ 1 & x_1 & x_1^2 \\ 1 & x_2 & x_2^2 \end{pmatrix} \begin{pmatrix} a_0 \\ a_1 \\ a_2 \end{pmatrix} = \begin{pmatrix} f_0 \\ f_1 \\ f_2 \end{pmatrix} \quad (\text{A.2})$$

The extremum argument of the parabola is given by:

$$x_m = -\frac{a_1}{2a_2} \quad (\text{A.3})$$

By Cramer's rule:

$$a_0 = \frac{\begin{vmatrix} f_0 & x_0 & x_0^2 \\ f_1 & x_1 & x_1^2 \\ f_2 & x_2 & x_2^2 \end{vmatrix}}{\begin{vmatrix} 1 & x_0 & x_0^2 \\ 1 & x_1 & x_1^2 \\ 1 & x_2 & x_2^2 \end{vmatrix}}, \quad a_1 = \frac{\begin{vmatrix} 1 & f_0 & x_0^2 \\ 1 & f_1 & x_1^2 \\ 1 & f_2 & x_2^2 \end{vmatrix}}{\begin{vmatrix} 1 & x_0 & x_0^2 \\ 1 & x_1 & x_1^2 \\ 1 & x_2 & x_2^2 \end{vmatrix}}, \quad a_2 = \frac{\begin{vmatrix} 1 & x_0 & f_0 \\ 1 & x_1 & f_1 \\ 1 & x_2 & f_2 \end{vmatrix}}{\begin{vmatrix} 1 & x_0 & x_0^2 \\ 1 & x_1 & x_1^2 \\ 1 & x_2 & x_2^2 \end{vmatrix}} \quad (\text{A.4})$$

Hence the direct calculation of the extremum point x_m from the sampled points is given by:

$$x_m = -\frac{a_1}{2a_2} = -\frac{\begin{vmatrix} 1 & f_0 & x_0^2 \\ 1 & f_1 & x_1^2 \\ 1 & f_2 & x_2^2 \end{vmatrix}}{\begin{vmatrix} 1 & x_0 & f_0 \\ 1 & x_1 & f_1 \\ 1 & x_2 & f_2 \end{vmatrix}} = \frac{1}{2} \frac{x_0^2(f_2-f_1)+x_1^2(f_0-f_2)+x_2^2(f_1-f_0)}{x_0(f_2-f_1)+x_1(f_0-f_2)+x_2(f_1-f_0)} \quad (\text{A.5})$$

The value of the extremum f_m is given by:

$$f_m = a_0 + a_1x_m + a_2x_m^2 = a_0 - a_1 \frac{a_1}{2a_2} + a_2 \left(\frac{a_1}{2a_2} \right)^2 = a_0 - \frac{a_1^2}{4a_2} = a_0 + \frac{a_1x_m}{2} \quad (\text{A.6})$$

$$f_m = \frac{1}{\begin{vmatrix} 1 & x_0 & x_0^2 \\ 1 & x_1 & x_1^2 \\ 1 & x_2 & x_2^2 \end{vmatrix}} \left(\begin{vmatrix} f_0 & x_0 & x_0^2 \\ f_1 & x_1 & x_1^2 \\ f_2 & x_2 & x_2^2 \end{vmatrix} + \frac{x_m}{2} \begin{vmatrix} 1 & f_0 & x_0^2 \\ 1 & f_1 & x_1^2 \\ 1 & f_2 & x_2^2 \end{vmatrix} \right) =$$

$$\frac{f_0x_1x_2(x_2-x_1)+f_1x_0x_2(x_0-x_2)+f_2x_0x_1(x_1-x_0)+\frac{x_m}{2}(x_0^2(f_2-f_1)+x_1^2(f_0-f_2)+x_2^2(f_1-f_0))}{x_1x_2(x_2-x_1)+x_0x_2(x_0-x_2)+x_0x_1(x_1-x_0)} \quad (\text{A.7})$$

It is possible to reduce the number of calculations by shifting the x axis so that one of the sampling points becomes zero:

$$x = x - x_1 \quad (\text{A.8})$$

Then in the shifted axis the new sampled points will be:

$$x_0 = x_0 - x_1 \quad x_1 = x_1 - x_1 = 0 \quad x_2 = x_2 - x_1 \quad (\text{A.9})$$

Then x_m' is given by:

$$x_m = \frac{1}{2} \frac{x_0^2(f_2-f_1)+x_2^2(f_1-f_0)}{x_0(f_2-f_1)+x_2(f_1-f_0)} \quad (\text{A.10})$$

and f_m is given by:

$$f_m = f_1 + \frac{x_m(x_0^2(f_2-f_1)+x_2^2(f_1-f_0))}{2x_0x_2(x_0-x_2)} \quad (\text{A.11})$$

Further reduction of calculations can be achieved by calculating terms that appears more than once in the equations as temporary values α , γ and δ :

$$\alpha = x_0(f_2 - f_1), \gamma = x_2(f_1 - f_0) \tag{A.12}$$

$$\delta = x_0'\alpha + x_2'\gamma \tag{A.13}$$

$$x_m' = \frac{1}{2} \frac{\delta}{\alpha + \gamma} \tag{A.14}$$

$$x_m = x_m' + x_1 \tag{A.15}$$

$$f_m = f_1 + \frac{x_m'\delta}{2x_0'x_2'(x_0' - x_2')} \tag{A.16}$$

This calculation requires only four multiplications and one division to be executed to calculate x_m after the calculation of the three sampled points' power, which takes three multiplications. There is no need to calculate the value at the maximum f_m , since only the location of the maximum is required for algorithm operation, although it can be calculated by executing three additional multiplications and a division.

If the distance between the sampled points is equal:

$$x_2 - x_1 = x_1 - x_0 \tag{A.17}$$

Then the axis transformation:

$$x' = \frac{x - x_1}{x_2 - x_1} \tag{A.18}$$

Will give:

$$x_0' = -1 \quad x_1' = 0 \quad x_2' = 1 \tag{A.19}$$

Then x_m can be calculated by executing one division and one multiplication as:

$$x_m' = \frac{1}{2} \frac{f_0 - f_2}{f_0 - 2f_1 + f_2} \tag{A.20}$$

$$x_m = x_m'(x_2 - x_1) + x_1 \tag{A.21}$$

Then f_m can be calculated by executing an additional multiplication as:

$$f_m = f_1 + \frac{x_m'}{4} (f_2 - f_0) \tag{A.22}$$

Appendix B

Calculation of a maximum point in rotated axis

In some cases the interpolation error can be reduced by rotating the axis of the sampled points as shown in Figure B.1. However, the maximum point in the rotated coordinates is different from the maximum in the original coordinates and it is required to calculate the maximum of the function in the original coordinates.

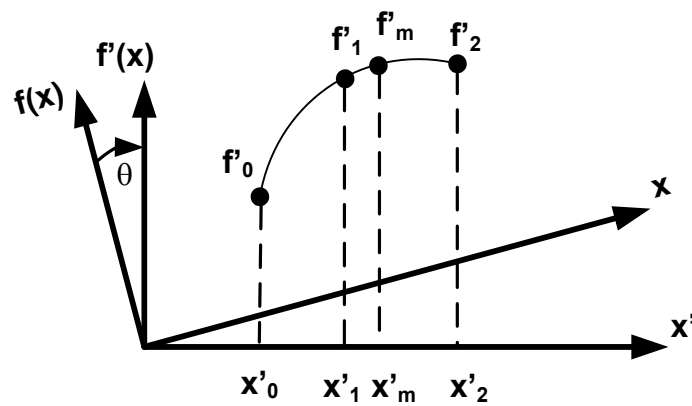


Figure B.1 Sampled points on rotated axis.

To simplify the calculations the axis can be shifted so that one of the sampled points will be in the axis origin:

$$x'' = x - x_0 \quad (\text{B.1})$$

$$f'' = f - f_0 \quad (\text{B.2})$$

So that $(x_0'', f_0'') = (0, 0)$.

The sampled values in the rotated coordinates are given by:

$$\begin{pmatrix} x \\ f \end{pmatrix} = \begin{pmatrix} \cos \theta & -\sin \theta \\ \sin \theta & \cos \theta \end{pmatrix} \begin{pmatrix} x'' \\ f'' \end{pmatrix} \quad (\text{B.3})$$

The rotated polynomial is:

$$f = a_2x^2 + a_1x + a_0 \quad (\text{B.4})$$

The derivative at the extremum in the original axis is zero but it is equal to $\tan \theta$ in the rotated axis:

$$\frac{df}{dx} = 2a_2x + a_1 = \tan \theta \quad (\text{B.5})$$

The location of the extremum is:

$$x_m = \frac{\tan \theta - a_1}{2a_2} \quad (\text{B.6})$$

And the extremum value is:

$$f_m = a_2x_m^2 + a_1x_m + a_0 = \frac{x_m(\tan \theta + a_1)}{2} + a_0 \quad (\text{B.7})$$

By Cramer's rule:

$$a_0 = \frac{\begin{vmatrix} f_0 & x_0 & x_0^2 \\ f_1 & x_1 & x_1^2 \\ f_2 & x_2 & x_2^2 \end{vmatrix}}{\begin{vmatrix} 1 & x_0 & x_0^2 \\ 1 & x_1 & x_1^2 \\ 1 & x_2 & x_2^2 \end{vmatrix}}, \quad a_1 = \frac{\begin{vmatrix} 1 & f_0 & x_0^2 \\ 1 & f_1 & x_1^2 \\ 1 & f_2 & x_2^2 \end{vmatrix}}{\begin{vmatrix} 1 & x_0 & x_0^2 \\ 1 & x_1 & x_1^2 \\ 1 & x_2 & x_2^2 \end{vmatrix}}, \quad a_2 = \frac{\begin{vmatrix} 1 & x_0 & f_0 \\ 1 & x_1 & f_1 \\ 1 & x_2 & f_2 \end{vmatrix}}{\begin{vmatrix} 1 & x_0 & x_0^2 \\ 1 & x_1 & x_1^2 \\ 1 & x_2 & x_2^2 \end{vmatrix}} \quad (\text{B.8})$$

If $(x_0, f_0) = (0, 0)$ then:

$$a_0 = \frac{\begin{vmatrix} 0 & 0 & 0 \\ f_1 & x_1 & x_1^2 \\ f_2 & x_2 & x_2^2 \end{vmatrix}}{\begin{vmatrix} 1 & 0 & 0 \\ 1 & x_1 & x_1^2 \\ 1 & x_2 & x_2^2 \end{vmatrix}}, \quad a_1 = \frac{\begin{vmatrix} 1 & 0 & 0 \\ 1 & f_1 & x_1^2 \\ 1 & f_2 & x_2^2 \end{vmatrix}}{\begin{vmatrix} 1 & 0 & 0 \\ 1 & x_1 & x_1^2 \\ 1 & x_2 & x_2^2 \end{vmatrix}}, \quad a_2 = \frac{\begin{vmatrix} 1 & 0 & 0 \\ 1 & x_1 & f_1 \\ 1 & x_2 & f_2 \end{vmatrix}}{\begin{vmatrix} 1 & 0 & 0 \\ 1 & x_1 & x_1^2 \\ 1 & x_2 & x_2^2 \end{vmatrix}} \quad (\text{B.9})$$

$$a_0 = 0, \quad a_1 = \frac{f_1x_2^2 - f_2x_1^2}{x_1x_2(x_2 - x_1)}, \quad a_2 = \frac{f_2x_1 - f_1x_2}{x_1x_2(x_2 - x_1)} \quad (\text{B.10})$$

The coordinates of the extremum can be calculated using the direct equations:

$$x_m = \frac{\tan \theta - a_1}{2a_2} = \frac{x_1x_2(x_2 - x_1)\tan \theta - f_1x_2^2 + f_2x_1^2}{2(f_2x_1 - f_1x_2)} \quad (\text{B.11})$$

$$f_m = \frac{x_m(\tan \theta + a_1)}{2} = \frac{1}{2}x_m \left(\tan \theta + \frac{f_1x_2^2 - f_2x_1^2}{x_1x_2(x_2 - x_1)} \right) \quad (\text{B.12})$$

To reduce the amount of calculations, terms that appear more than once in the equations can be pre-calculated:

$$\alpha_1 = x'_1 f'_2, \quad \alpha_2 = x'_2 f'_1 \tag{B.13}$$

$$\beta = x'_1 x'_2 (x'_2 - x'_1) \tag{B.14}$$

$$\gamma = \alpha_1 x'_1 - \alpha_2 x'_2 \tag{B.15}$$

Then:

$$x'_m = \frac{\beta \tan \theta + \gamma}{2(\alpha_1 - \alpha_2)} \tag{B.16}$$

$$f'_m = \frac{1}{2} x'_m \left(\tan \theta - \frac{\gamma}{\beta} \right) \tag{B.17}$$

The result is needed to be transformed to the original axis:

$$\begin{pmatrix} x''_m \\ f''_m \end{pmatrix} = \begin{pmatrix} \cos \theta & \sin \theta \\ -\sin \theta & \cos \theta \end{pmatrix} \begin{pmatrix} x'_m \\ f'_m \end{pmatrix} \tag{B.18}$$

$$x_m = x''_m + x_0 \tag{B.19}$$

$$f_m = f''_m + f_0 \tag{B.20}$$

This calculation of x_m requires 18 multiplications and two divisions to be performed by the microcontroller. Calculation of f_m requires two additional multiplications.

Appendix C

Simulations of interpolation error in presence of noise

This appendix contains additional plots for section 5.4 – Interpolation of PV power curves in presence of noise. The plots show mean and maximal (worst case) power losses ($P_{MPP} - P_{op_est_MPP}$) as a result of maximum calculation via interpolation for different distances between sampling points and for calculations in P- V_{ref} and P-V planes. The information is provided in both linear and logarithmic scales for easier evaluation. Each point in the plots is based on statistics of 10,000 calculations in the same conditions with Gaussian noise. These plots were used for selection of the region of low error. In some cases the maximal power loss was larger than P_{MPP} , this is because mathematical model used to represent the PV array includes operation at negative voltages and currents, which does not occur in practice. Even though, the graphs provide useful information about the scale of the error in calculation.

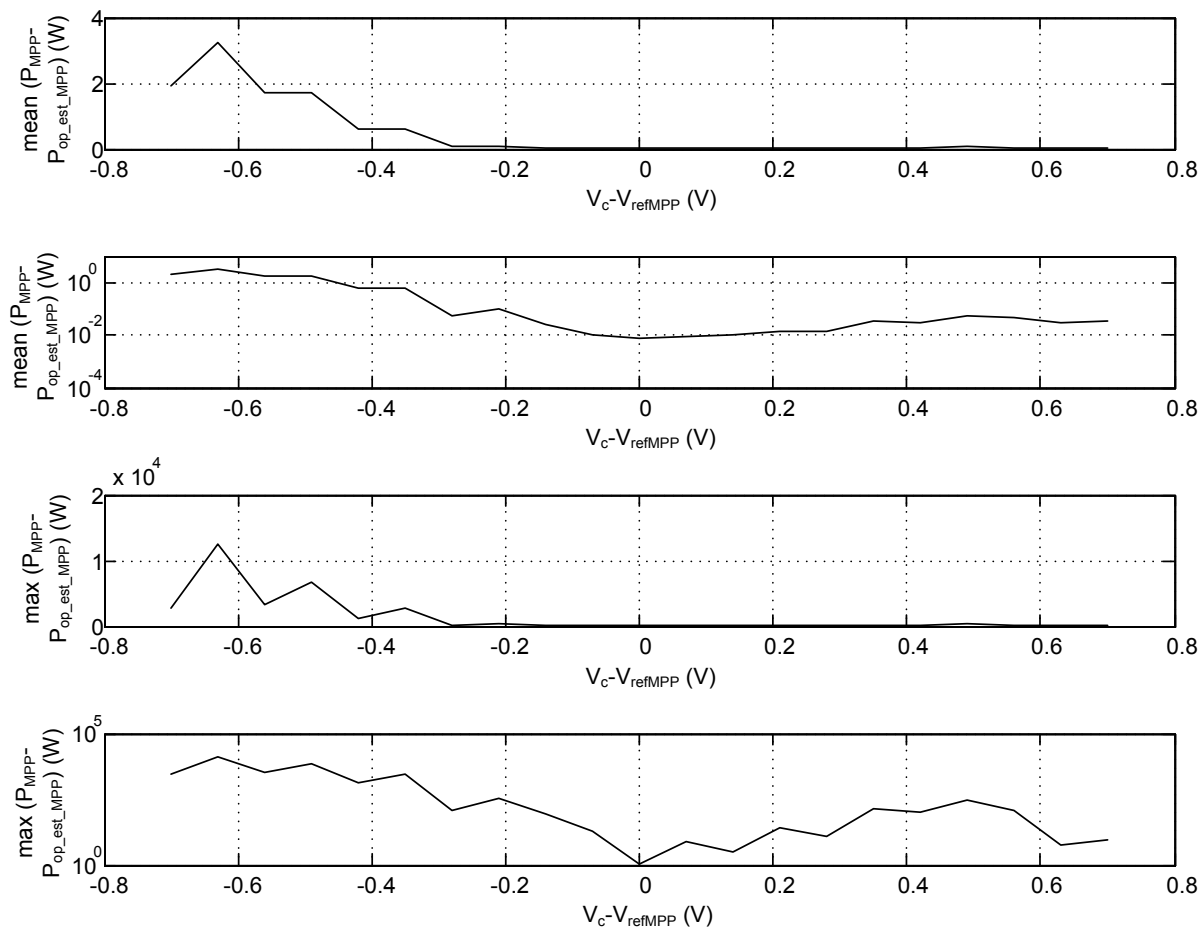


Figure C.1 Simulation results of power loss in maximum calculation in V-P plane at different sampling points in presence of noise. Distance between sampling points 0.7 V.

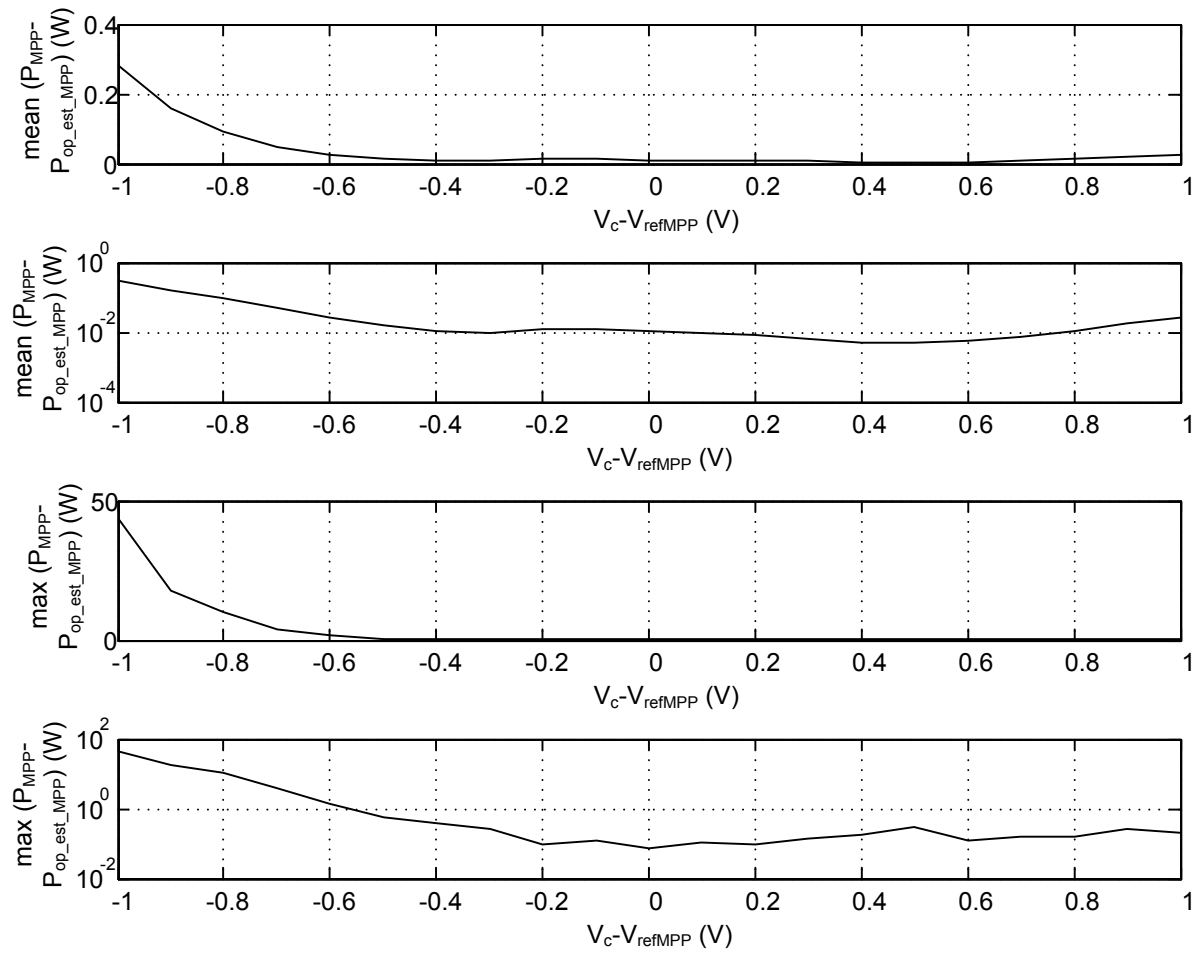


Figure C.2 Simulation results of power loss in maximum calculation in V-P plane at different sampling points in presence of noise. Distance between sampling points 1 V.

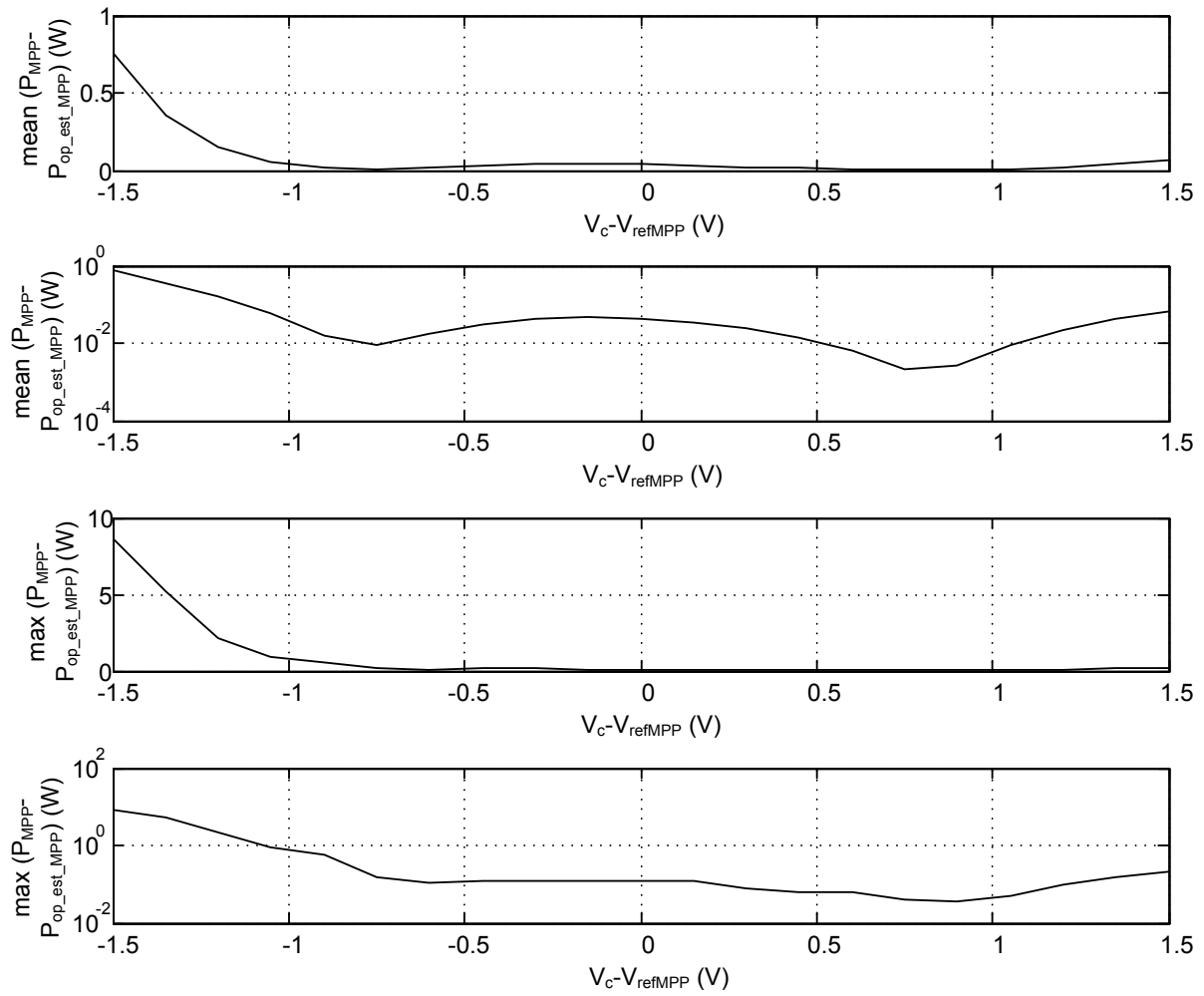


Figure C.3 Simulation results of power loss in maximum calculation in V-P plane at different sampling points in presence of noise. Distance between sampling points 1.5 V.

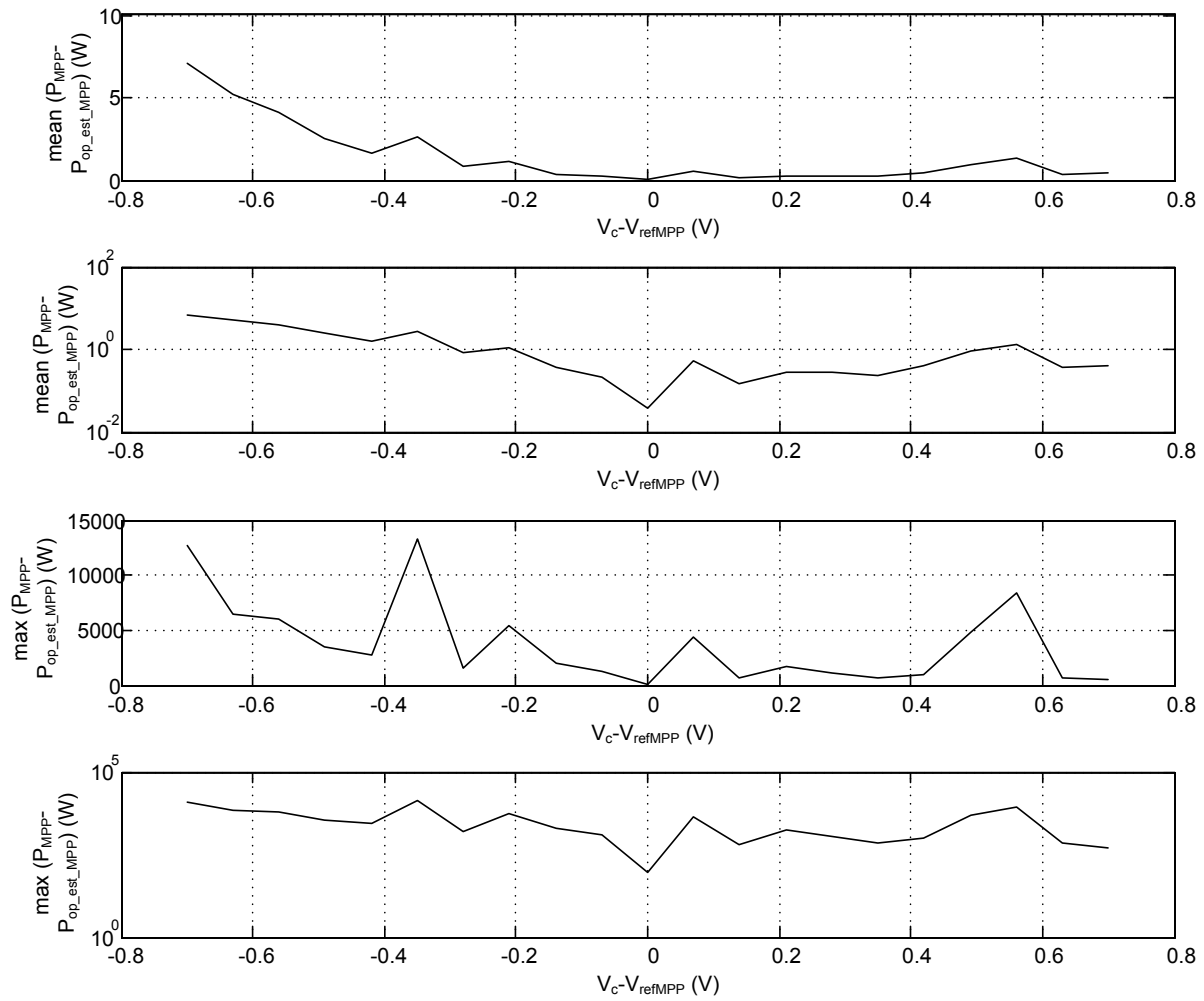


Figure C.4 Simulation results of power loss in maximum calculation in V_{ref} - P plane at different sampling points in presence of noise. Distance between sampling points 0.7 V.

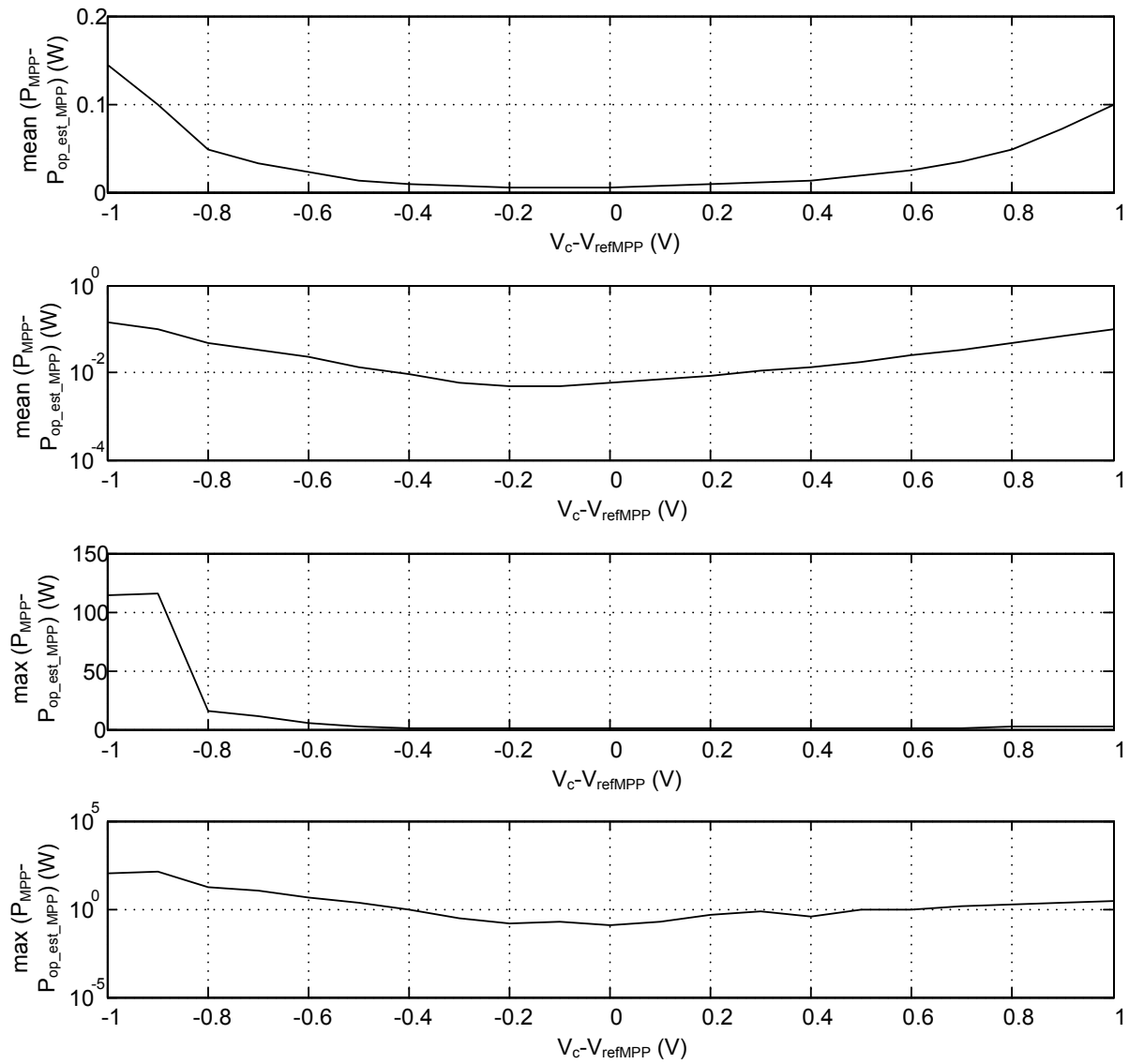


Figure C.5 Simulation results of power loss in maximum calculation in $V_{\text{ref}}-P$ plane at different sampling points in presence of noise. Distance between sampling points 1 V.

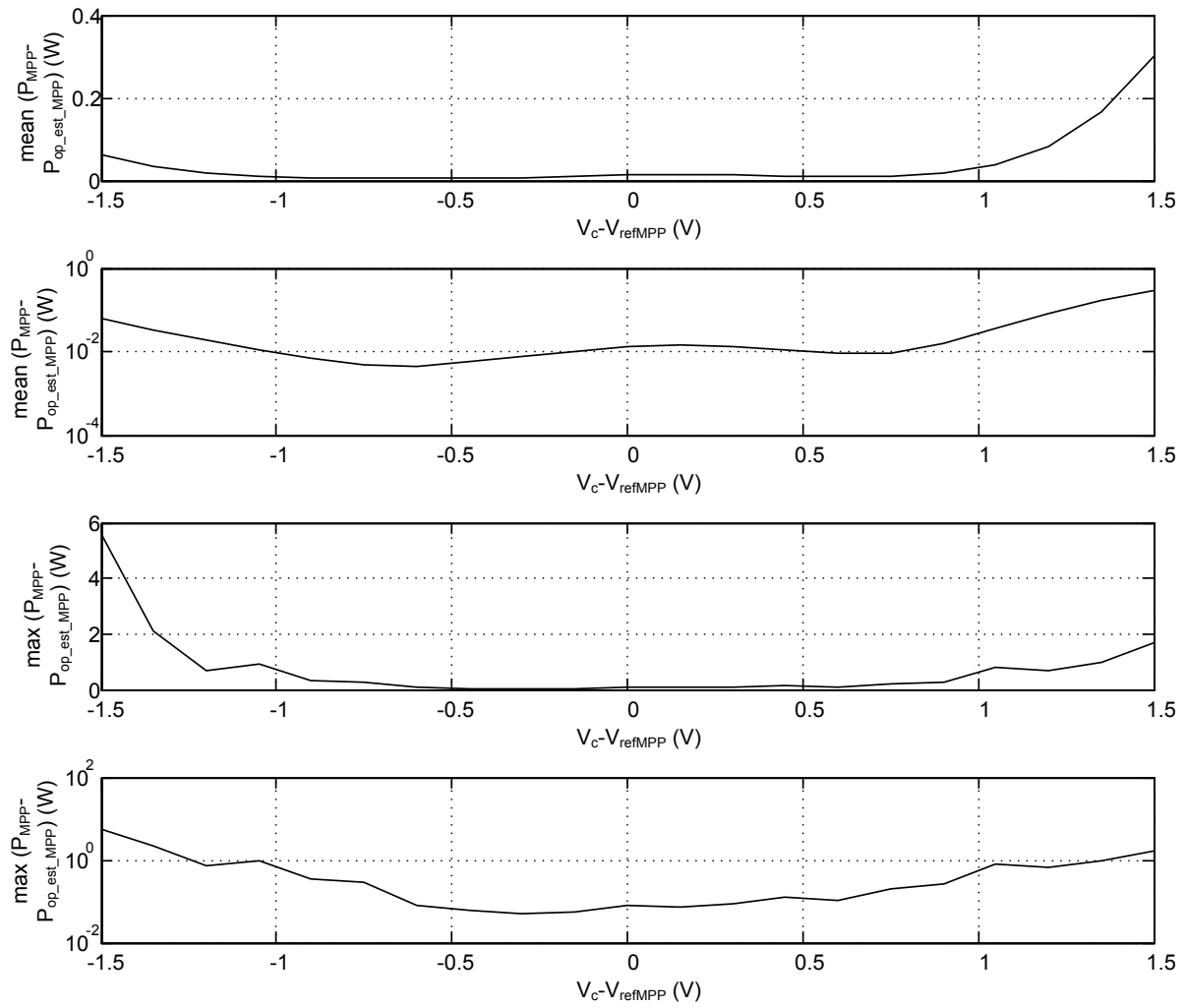


Figure C.6 Simulation results of power loss in maximum calculation in V_{ref} -P plane at different sampling points in presence of noise. Distance between sampling points 1.5 V.

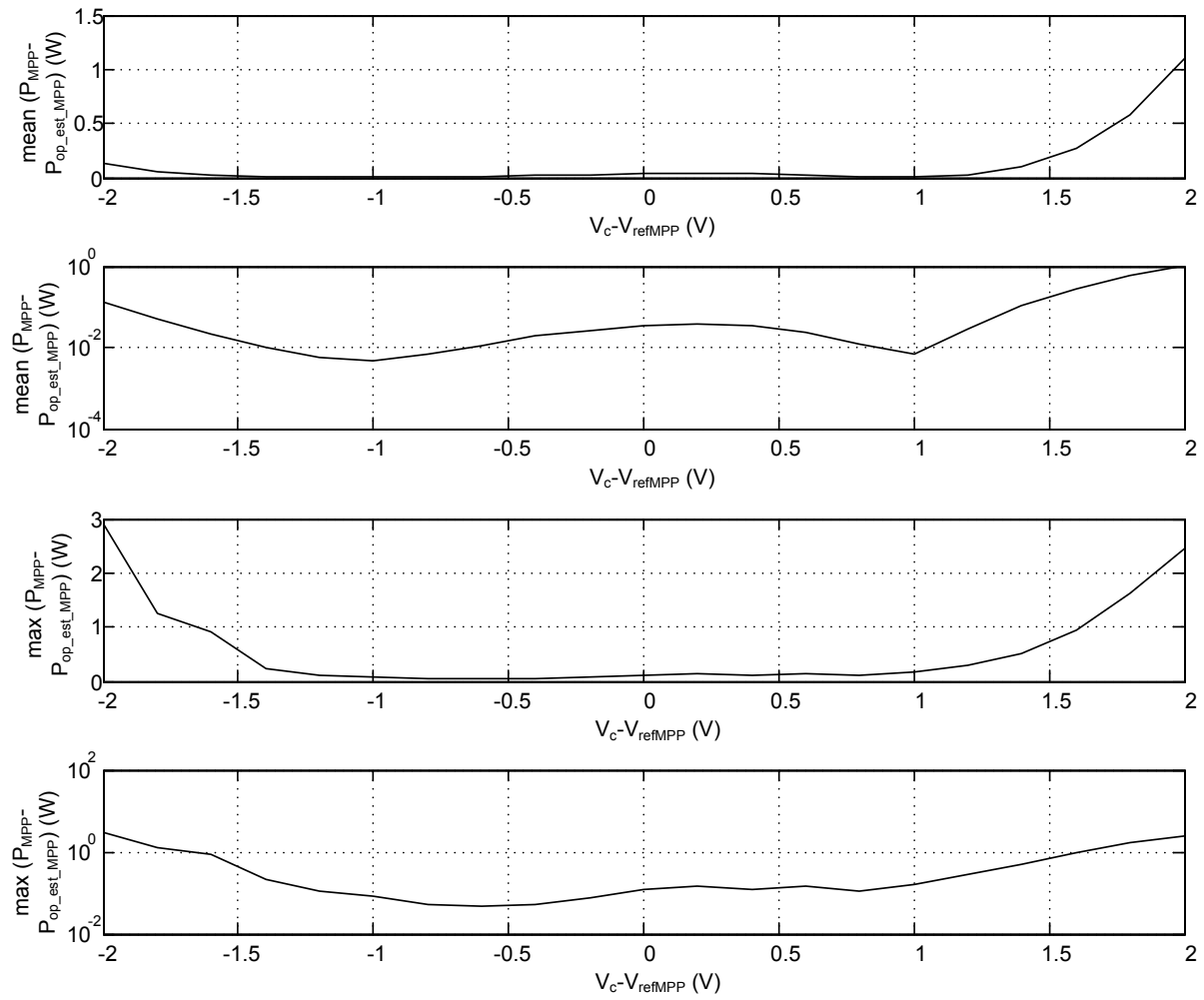


Figure C.7 Simulation results of power loss in maximum calculation in $V_{\text{ref}}-P$ plane at different sampling points in presence of noise. Distance between sampling points 2 V.